A New Continuous 4π-Frozen-Spin-Target for the Crystal Barrel Experiment

Dissertation
zur
Erlangung des Doktorgrades (Dr. rer. nat.)
der
Mathematisch-Naturwissenschaftlichen Fakultät
der
Rheinischen Friedrich-Wilhelms-Universität Bonn

vorgelegt von

Stefan Runkel

aus
Bonn

Bonn 2017

Angefertigt mit Genehmigung der Mathematisch-Naturwissenschaftlichen Fakultät der Rheinischen Friedrich-Wilhelms-Universität Bonn

1. Gutachter:	Priv. Doz. Dr. Stefan Goertz
2. Gutachter:	Prof. Dr. Reinhard Beck

Tag der Promotion:	17.10.2017
Erscheinungsjahr:	2018

Acknowledgements

I would like to thank ...

Priv. Doz. Dr. Stefan Goertz for the opportunity to work in the group of the polarised target in Bonn, the support and the guidance to complete my Diploma and my PhD thesis and having an interesting task to work on.

Prof. Reinhard Beck as the second corrector and the possibility to work in this field after this thesis.

Dr. Hartmut Dutz for the help and guidance and the hard work on the refrigerator and the test facility, for the many hours of testing leaks and discussing how to fix them. Also I want to thank him for the help on all the things in the everyday business.

Scott Reeve for the long but nice and funny time we worked together and the long hours we spend together in the lab. I would also thank Scott for the beautiful time we spend on workshops together.

Marcel Bornstein for the work we did together and the many interesting conversations in the office.

The polarised target team, all current and former members for all the collaboration and help during this thesis.

Markus Kriesinger for the steady work at the refrigerator and the many hours of constructing and mounting.

Toni Hanfland for the steady support of liquid helium.

Jörg Drückhammer and Dr. Moritz von Gliszczynski for the correction and advice to write this thesis.

My father for always believing in me and teaching me to never give up.

My wife Marie for her help and understanding during this long time, especially during those days when I had to work in the night.

Contents

Chapter 1

Introduction

In the 1960s, Murray Gell-Mann and George Zweig observed particles in bubble chamber experiments, that could not be explained with the already existing particle models. To explain these particles, they postulated the existence of quarks, which form the substructure of the nucleons. Explaining this substructure, the composition of matter and its interaction is the main challenge of particle physics. The standard model of particle physics consists of the following particles [1]:

$$\begin{pmatrix} u \\ d \end{pmatrix}\begin{pmatrix} c \\ s \end{pmatrix}\begin{pmatrix} t \\ b \end{pmatrix} \qquad \begin{pmatrix} e \\ \nu_e \end{pmatrix}\begin{pmatrix} \mu \\ \nu_\mu \end{pmatrix}\begin{pmatrix} \tau \\ \nu_\tau \end{pmatrix}$$

Within the standard model 6 quarks - u up, d down, c charm, s strange, t top, b bottom - , 6 leptons - e electron, μ muon, τ tauon and the three corresponding neutrinos ν_i - and the corresponding anti particles are known, which form the basis of all matter. Hadrons are formed by the strong interaction between the quarks. They consists of two quark states (mesons) or three quark states (baryons). For protons this results in (uud) and for neutrons (udd). In particle physic experiments, particle accelerators, detectors and target systems are used to investigate new and exited hadron states to improve the knowledge about the interaction between the quarks.

For example, the discovery of the Ω^- baryon [2] showed that mesons and baryons are composed of constituent quarks, but like the $\Delta^{++}(1232)$ and the $\Delta^-(1232)$ it consists of three identical quarks. The spin and parity of these baryons are $J^p = \frac{3}{2}^+$, which results for a quark spin of $s = \frac{1}{2}$ to a total quark spin of $S = \frac{3}{2}$. Thus the Pauli principle, which forbids two fermions with identical quantum numbers, was violated.

A new quantum number was introduced to solve this problem. Due to the necessary local gauge invariance, a new theory of strong interactions, **Q**uantum **C**hromo **D**ynamics (QCD), was deduced [3][4]. This theory assigned a new triple-valued charge called colour. With it, a state like the Ω^- baryon with (sss) is possible, because every quark is able to carry a different colour and the Pauli principle is fullfilled.

Nevertheless, there are some interesting physical problems in hadron physics to investigate. It is currently not understood how QCD generates the structure of hadrons and how symmetries influence their structures and their dynamics. At lower energies, several resonances were measured and are fitting well with the predictions from QCD, but additional measurements for other decay channels could bring more information about the coupling of the quarks and the inner structure of the nucleon. At higher energies, a large number of nucleon and Δ resonances were predicted and experimental proof for them is still missing [5].

The CBELSA/TAPS experiment uses photo production reactions to study the baryon resonance spectrum. In this case, four complex amplitudes for nucleon spin-flip, non-flip and for photon and nucleon spin aligned or anti-aligned, exist. Then 16 polarisation observables become accessible, which can be reduced to eight for the measurement of the differential cross section of a specific reaction [6]. Thus, if the polarisation of the target and the beam can be controlled and the recoil polarisation can be determined, the total cross section is given by

$$\begin{aligned}\frac{\mathrm{d}\sigma}{\mathrm{d}\Omega}(\vartheta,\ \phi) = \frac{\mathrm{d}\sigma}{\mathrm{d}\Omega}(\vartheta)\,[1 &- P_T \Sigma(\vartheta)\cos(2\phi) \\ &+ P_x\left(-P_T H(\vartheta)\sin(2\phi) + P_\circ F(\vartheta)\right) \\ &- P_y\left(P_T P(\vartheta)\cos(2\phi) - T(\vartheta)\right) \\ &- P_z\left(-P_T G(\vartheta)\sin(2\phi) + P_\circ E(\vartheta)\right)][7].\end{aligned} \tag{1.1}$$

P_T and $P_\circ$ are the linear or circular polarisation of the photon beam and $P_{x,\,y,\,z}$ the polarisation of the target whereas z is the direction of the beam. ϑ is the angle of the particle reaction and ϕ the angle between the reaction surface and the polarisation of the photon beam which is shown in Fig. 1.1. σ represents the cross section, Σ, T and P gives the asymmetry for the beam, the target or the recoil for a single polarisation measurement and the polarisation observables E, G, F and H are representing the four asymmetry observables for beam-target double polarisation reactions.

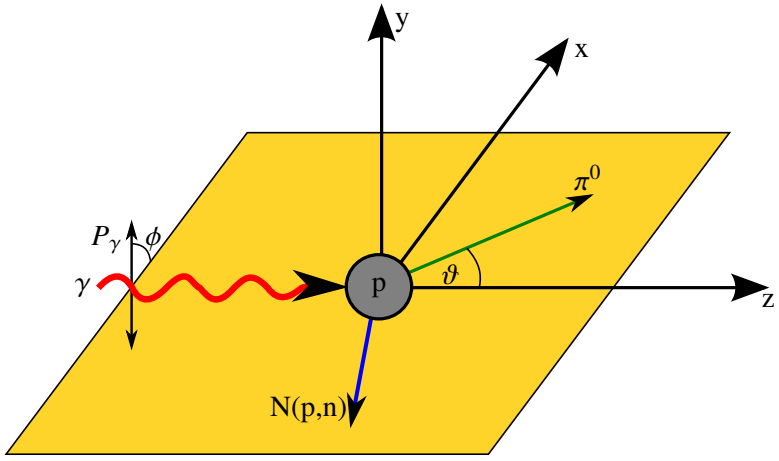

Figure 1.1: Reaction surface for a photo production reaction with the corresponding angles of the reaction.

Fig. 1.2 shows the total cross section for $\gamma p \rightarrow p\pi^0$ and the Breit-Wigner shapes of the different contributing resonances. There are three clean peaks which can be easily analysed but there are other contributing resonances which are not seen as obvious peaks. Baryon resonances are broad, which makes it challenging to extract them from the total cross section. Thus, using photo production reactions, the eight observables of Eq. 1.2 need to be measured over the full solid angle with high precision. This means a 4π acceptance of the detector is needed.

This also defines the requirements for the photon beam to study light-baryon resonances. The accelerator has to deliver unpolarised and polarised electrons with a large duty cycle from which an intense photon beam can be created. This photon beam is unpolarised, circular or linear polarised, depending

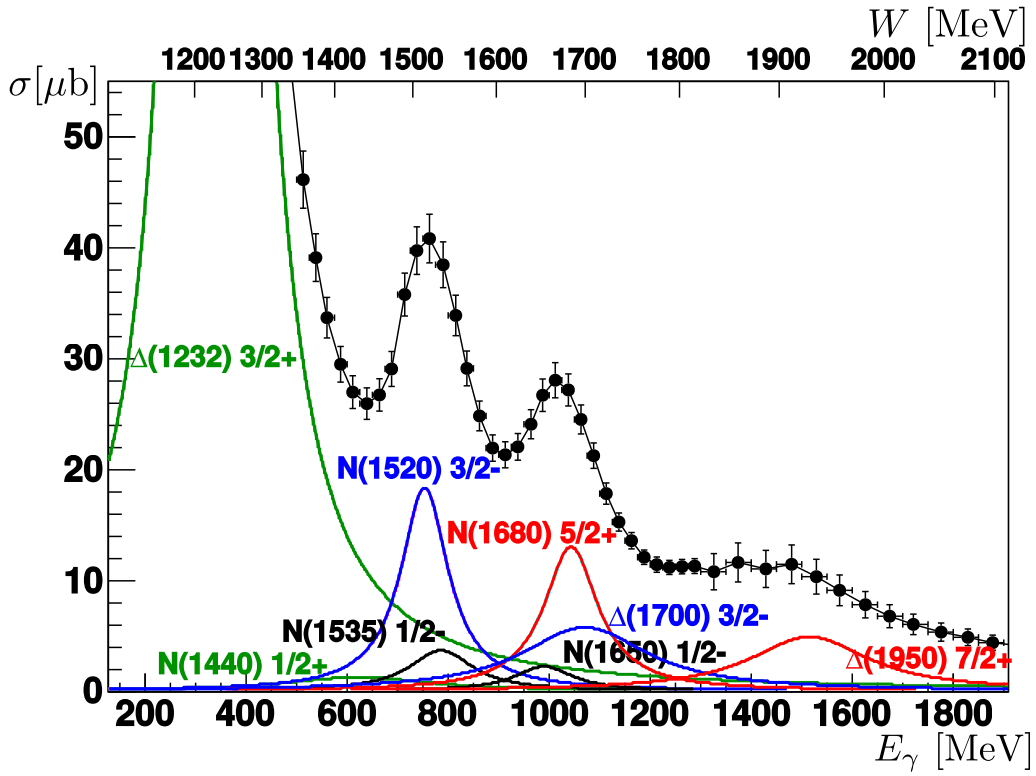

Figure 1.2: Total cross section of $\gamma p \rightarrow p\pi^0$ from the CBELSA/TAPS-data [8]. Also indicated are the BREIT-WIGNER shapes of the different resonances contributing to the reaction.

on the polarisation of the electron beam. In Bonn, for the CBELSA/TAPS experiment, the **EL**ectron **S**tretcher **A**ccelerator (ELSA) [9] provides an electron beam with the needed polarisation and energies up to 3.5 GeV. After the extraction from the stretcher ring, a radiator target within a goniometer is used to produce the unpolarised or polarised photon beam via bremsstrahlung. Fig. 1.3 shows the experimental area for CBELSA/TAPS including the detector system, the polarised target and the tagging system, used to analyse the momentum of the electrons after the bremsstrahlung process. The electron beam dump is used to catch the electron beam after production of the photon beam. The photon beam is guided through the beam line to the polarised target which is located in the centre of the CB detector.

The **C**rystal **B**arrel (CB) detector is suited to measure the decay of neutral mesons into photons. The CB consists of three layers scintillation fibres (513 fibres), used for the identification of charged particles, and of an electromagnetic calorimeter consisting of 1230 CsI(T1)-crystals. To measure particles in forward direction, below polar angles of 30°, two further calorimeters are used: the forward plug with 90 CsI(T1)-crystals, and the forward TAPS-wall consisting of 216 BaF_2 crystals. For the next measurement period of the CBELSA/TAPS experiment the CB detector has been upgraded [10]. Thus the readout of the CB calorimeter has been extended by a timing branch to gain trigger capability for the detector. This allows to measure completely neutral final states in photo production reactions. The readout for the inner crystals of the TAPS detector has been modified to be capable of high event rates for higher beam intensities. Due to higher beam intensities, a high cooling power for the polarised target is necessary, which is one of the reasons for designing a new dilution refrigerator.

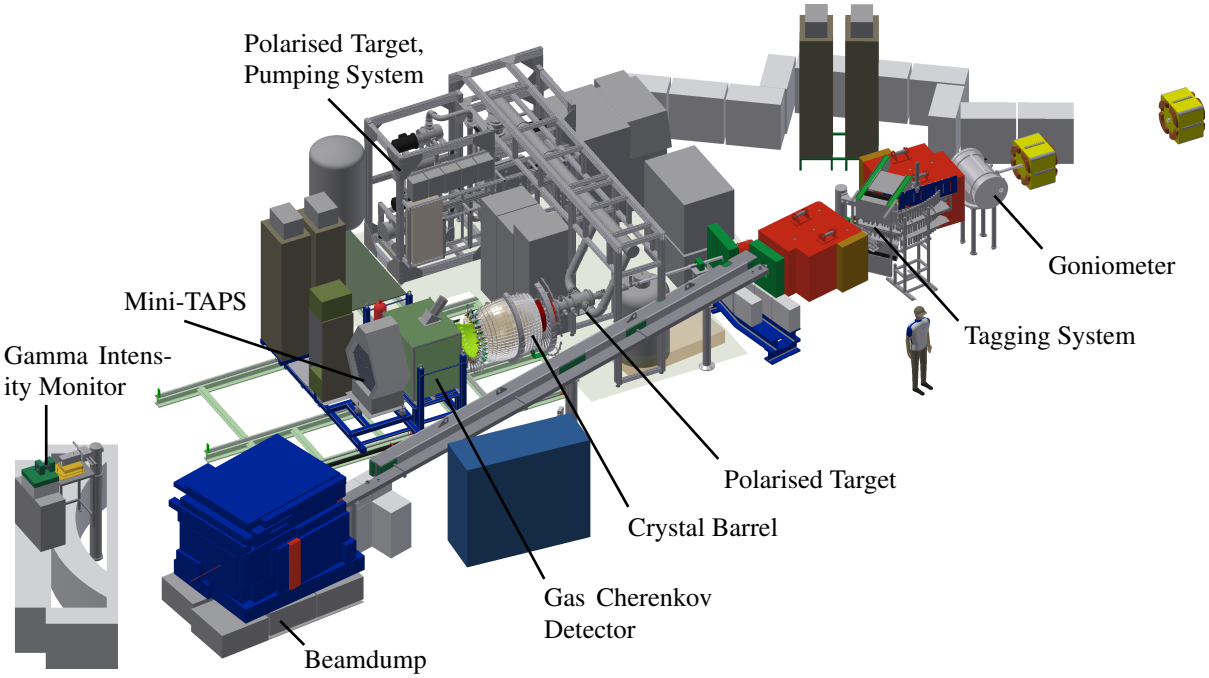

Figure 1.3: Experimental setup of the CBELSA/TAPS experiment

In the centre of the detector an unpolarised or polarised target is set. As explained later, for a high polarisation of a solid target, temperatures below 200 mK are mandatory. A dilution refrigerator is used to reach these temperatures. Due to the necessary 4π acceptance, the geometry of such a refrigerator within the CB detector is limited. This leads to a horizontal dilution refrigerator built around a beam tube connected to the beam line of the accelerator. Due to the inner diameter of the detector ($\oslash$ 105 mm) and the inner diameter of the existing polarising magnet ($\oslash$ 95 mm), the geometry of the front part is given.

For the measurements within the SFB project, a frozen-spin target system was used. The same refrigerator was used to measure the GDH sum rule, published by Gerasimov [11], Drell and Hearn [12], and is described by Bradkte [13]. This target system enabled, by the use of the frozen spin technique with an internal holding coil, the measurement of a spin dependent cross-section in combination with a polarised solid state target [14]. With this technique, the polarisation of the target material is maintained by holding coils for a transverse and a longitudinal polarisation with a magnetic field of 0.4 – 0.7 T. The thickness of these coils of less than 2 mm enables outgoing particles to pass through. This reduces the threshold for the detection of them as good as possible. In former target systems, a vertical dilution refrigerator was used leading to a reduction of the angular acceptance [15].

Within this thesis, a new horizontal dilution refrigerator for the CBESLA/TAPS experiment has been built. This new system, with its horizontal alignment of the refrigerator, allows the placement of the cryogenic components around the beam-axis in the backward region. This design extends the angular acceptance to almost 4π in the laboratory frame. It allows measuring with a 4π detector in frozen spin mode, if it is possible to remove the detector to polarise the target with an external magnet, as for the last frozen-spin solid state target, operated by the polarised target group in Bonn. Nevertheless, the data taking has to be interrupted every 2 d to 4 d, depending of the relaxation time of the target material. The

design of the new dilution refrigerator, presented in this thesis, allows a continuous operating target. The idea to built a continuous mode target with a 4π acceptance for the CB detector was first presented by H. Dutz in [16] and [17]. The design is also based on his work [18].

The goal is to increase the luminosity of the scattering experiment and an enhancement of the **F**igure **o**f **M**erit (FOM) of the polarised solid target. Both quantities characterise the quality of the experiment and how fast it can be performed for a given accuracy. The luminosity L, which is defined as the product of the beam Intensity I and the target thickness n_t

$$L = I \cdot n_t, \tag{1.2}$$

is connected to the counting rate N with the differential cross section $\frac{\mathrm{d}\sigma}{d\Omega}$ and the angular acceptance $\Delta\Omega$ of the detection system like

$$N = L\frac{\mathrm{d}\sigma}{\mathrm{d}\Omega}\Delta\Omega. \tag{1.3}$$

Typical luminosity's reached in particle experiments with polarised targets are of the order of $10^{30}\,\mathrm{cm}^{-2}\,\mathrm{s}^{-1}$ to $10^{34}\,\mathrm{cm}^{-2}\,\mathrm{s}^{-1}$. An improvement of the cooling power of a solid target leads to a higher possible luminosity and is always the goal by improving the cryogenic systems of a polarised solid target. The FoM of an external polarised solid state target can be defined as

$$\mathrm{FoM} = \rho \cdot \kappa \cdot P_\mathrm{T}^2 \cdot f^2, \tag{1.4}$$

with

$$f = \frac{N_{\text{pol. nucleons}}}{N_{\text{nucleons}}}. \tag{1.5}$$

Here ρ is the density of the target material, κ the filling factor of the target container, f the dilution factor of the material himself and P_T is the target polarisation. An enhancement of the FoM leads to a shorter running time to achieve a chosen accuracy in the measurement of a polarisation observable. The improvement of the cryogenic system and the usage of a continuous mode operating target increases the target polarisation P_T and improves the FoM. Due to the higher base temperature in continuous mode (200 mK), a higher cooling power is accessible which increases the possible luminosity of the experiment. In Chap. 2 the polarisation mechanism for solid targets, used to reach high nucleon polarisation, is presented. Afterwards the difference between a continuous operating and a frozen-spin target, and how it increases the FoM, is described in detail. The geometry of the detector and the necessary parameter for a continuous operating target leads to the following parameters for the new dilution refrigerator:

- Support for high current (90 A) internal superconducting magnets
- High cooling power at temperatures of 200 mK for continuous polarisation during the experiment
- Minimal temperature of 30 mK for high relaxation times in frozen-spin mode
- Maximum diameter of 94 mm for the target region due to the geometry of the detector and the geometry of the external polarisation magnet for frozen-spin mode ($\oslash$ 95 mm)

To reach temperatures as low as needed for a polarised target, the usage of liquid helium is necessary. Chap. 3 describes the most important physical properties of the two helium isotopes used in a dilution refrigerator. A ^{3}He-^{4}He mixture cools the target material down to 30 mK (for frozen-spin mode), under the usage of the dilution effect. This ^{3}He-^{4}He mixture has to circulate in a closed system, due to the high costs of ^{3}He. Liquid ^{4}He is used to precool and liquefy the circulating mixture. By the process of evaporation, it is possible to cool the circulating mixture down to $\approx$ 1 K before it is used in the main cooling unit of the refrigerator.

In designing a dilution refrigerator, the calculation of the performance of the different cooling stages is of major importance. Hence, it is possible to calculate two stream heat exchangers, as described in [19] or [20], analytically, three stream counter flow heat exchangers are hard to calculate in an accurate way. Also, for complex geometries, it is difficult to determine the characteristic flow parameter like the PRANDLT and NUSSELT numbers. Due to this problems, a iterative procedure was used to calculate the performance of the precooling stages of the refrigerator. Chap 4 describes this mathematical method to analyse the precooling stages which are used for the cooling of the circulating ^{3}He-^{4}He mixture. These **C**omputational **F**luid **D**ynamic simulations are based on the NAVIER-STOKES equations and uses a **F**inite **V**olume **M**ethod to solve these with an iterative procedure. Thus, a full vector field for the important flow parameter of each heat exchanger is available for the first time, which enables a new way for the optimisation of the different cooling parts of dilution refrigerators like it is described in this thesis.

The description of the target system itself is given in Chap 5. The refrigerator consists of two main parts:

- **The precooling unit**, which cools the circulating ^{3}He-^{4}He mixture to a temperature of 1 K
- **The dilution unit**, cools the polarised solid target to temperatures below 200 mK depending on the operation mode of the refrigerator.

First the possible heat sources, which increase the temperature of the target material, were calculated. To reach temperatures below 50 mK, it is important to reduce the heat to the mixing chamber as much as possible. The different parts of the precooling are explained and the results of the CFD simulations for the different parts are discussed. The dilution unit was analysed by the usage of the calculations of Frossati [21][22]. A simulation like for the precooling stages was not possible, due to the necessary computer performance needed to build a simulation mesh for a copper sintered heat exchanger.

Chap. 6 describes the test facility built to measure the performance of this new horizontal dilution refrigerator. A new DAQ was implemented and the test facility includes a measurement system for the temperature, the flow and the outlet pressure for each cooling stage. In addition a mass spectrometer was installed to control the ^{3}He-^{4}He rate during the operation in dilution mode.

First tests with pure ^{4}He were performed to measure the performance of the precooling stages. In this tests, a minimal temperature of 900 mK was reached. The liquefaction rate of the precooling unit was measured by the usage of ^{4}He as a test fluid. Due to a cold leak, it was not possible to test the refrigerator in dilution mode. Thus, fixing this leak and finishing the refrigerator for the usage at the CBELSA/TAPS facility is ongoing. Also, first tests with the internal polarisation magnet were done to test the possibility of a continuous mode operating solid target.

Chapter 2

Polarisation Mechanisms

For double polarisation experiments like those performed at CBELSA/TAPS in Bonn, a polarised target is required. The polarisation of the protons (or deuterons) of a target material is of especially interest. In Fig. 2.1 the polarisation in thermal equilibrium at a constant magnetic field $\underline{B}$, dependent on the temperature, is shown. It is obvious that high proton or deuteron polarisation in thermal equilibrium

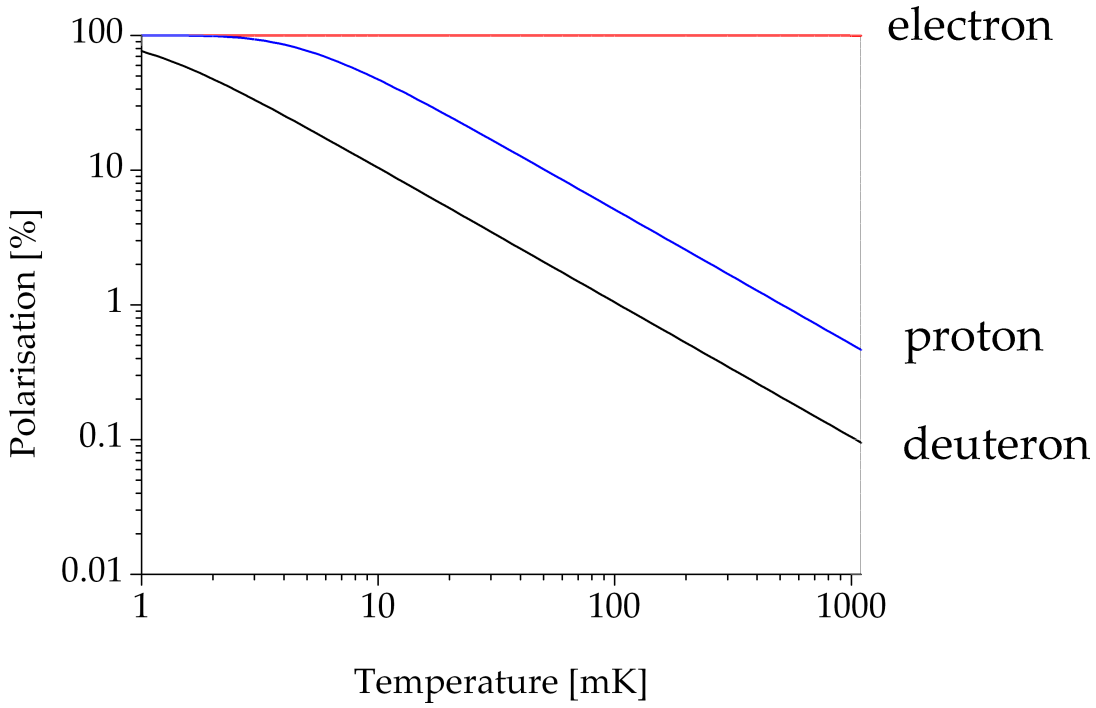

Figure 2.1: Polarisation in thermal equilibrium depending on the temperature

can only be reached with low temperatures. An additional parameter is the magnetic field strength, increasing the magnetic field leads also to a higher nucleon polarisation. A description for the polarisation in thermal equilibrium and how to reach high polarisation with the brute force method can be found in chapter 2.1. In the case of a polarised target for particle physics experiments, the so called DNP method is used. The idea of the **D**ynamic **N**uclear **P**olarisation is to translate the high electron polarisation to the nucleon. Two models for this process are described in chapter 2.2. Afterwards, the two techniques used to provide a high target polarisation for the experiment will be outlined in detail (chapter 2.3).

2.1 Polarisation at Thermal Equilibrium

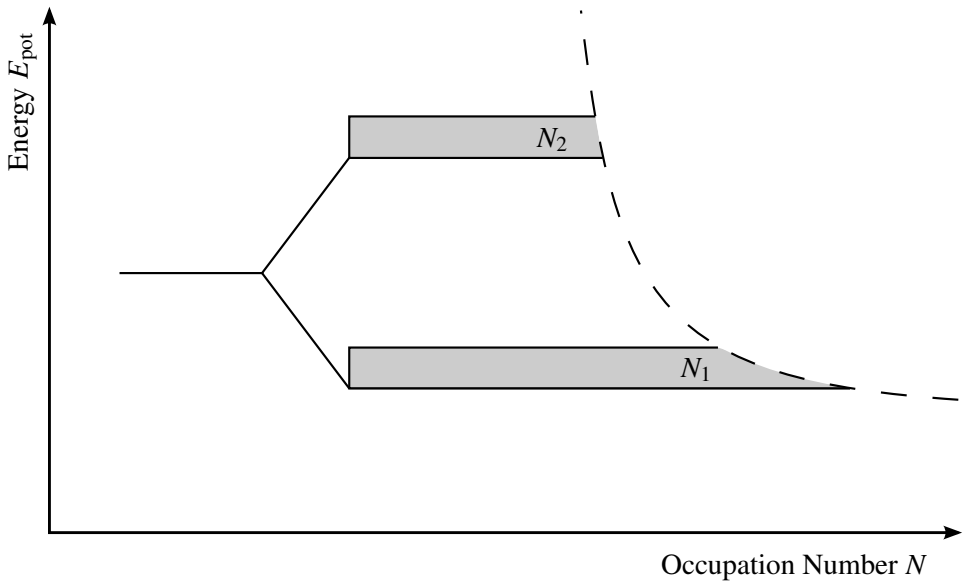

Figure 2.2: Occupation of the sub-levels of a spin-$\frac{1}{2}$-system

The target material is an ensemble of nucleons, made up of protons and neutrons. Under the conditions of a polarised target, the target material is cooled to a temperature of less than 1 K and is permeated by a magnetic field of about 2.5 T. The splitting of the energy levels of a particle system with spin s in an external magnetic field into $2s+1$ sub-levels can be described by the Zeeman effect. The energy of these levels depends on the Landé factor g, the magnetic moment $\vec{\mu}$, the z-component of the spin m and the magnetic field $\underline{B}$ and is given by [23]

$$E_{pot} = -\underline{\mu}\underline{B} = -g\mu_N mB, \tag{2.1}$$

with

$$\underline{B} = B \cdot \hat{e}_z. \tag{2.2}$$

The spins interact with the crystal lattice and after a specific time depending on the temperature and the external magnetic field, the spins relaxate into a thermal equilibrium. In thermal equilibrium, the occupation of the sub-levels follows the Boltzmann statistics, which is shown in Fig. 2.2. In this situation, the occupation number N_i of the sub-level E_i is given by

$$N_i = n_i \cdot \frac{N}{Z} \cdot e^{-\frac{E_i}{k_B T}}, \tag{2.3}$$

with

$$Z = \sum_i n_i \cdot e^{-\frac{E_i}{k_B T}}. \tag{2.4}$$

k_B is the Boltzmann constant, n_i the distribution of uncoupling of the energy levels and $N = \sum N_i$ the

number of all particles of the system, which have the energy E_i at the temperature T. In case of a spin-$\frac{1}{2}$-system like in Fig. 2.2, the ratio between the occupation numbers N_1 and N_2 is given by

$$\frac{N_1}{N_2} = e^{-\frac{\Delta E}{k_B T}} = e - \frac{g\mu_N B}{k_B T}\,(m_2 - m_1). \tag{2.5}$$

The polarisation of a macroscopic system, with a nucleon spin I, is defined as

$$P_z := \frac{I_z}{I}, \tag{2.6}$$

thus the polarisation of a spin $\frac{1}{2}$ and a spin 1 system can be written as

$$P_{\frac{1}{2}} = \frac{N_{\frac{1}{2}} \cdot \frac{1}{2} + N_{-\frac{1}{2}} \cdot \left(-\frac{1}{2}\right)}{\frac{1}{2}\left(N_{\frac{1}{2}} + N_{-\frac{1}{2}}\right)} = \frac{N_{\frac{1}{2}} - N_{-\frac{1}{2}}}{N_{\frac{1}{2}} + N_{-\frac{1}{2}}} = \tanh\left(\frac{\hat{\mu}B}{2k_B T}\right), \tag{2.7}$$

$$P_1 = \frac{N_1 - N_{-1}}{N_1 + N_0 + N_{-1}} = \frac{4\tanh\left(\frac{\hat{\mu}B}{2k_B T}\right)}{3 + \tanh^2\left(\frac{\hat{\mu}B}{2k_B T}\right)}. \tag{2.8}$$

Table 2.1 shows the polarisation at the temperature of liquid nitrogen (77 K), at 1 K which can be reached in a ^{4}He evaporation refrigerator and at 50 mK, which is a moderate temperature for a dilution refrigerator. The reason for this huge difference in the polarisation at thermal equilibrium is the difference in the magnetic moments of the particles. The magnetic moment of the electron μ_e is 660 times higher than the magnetic moment μ_p of the proton. If neutrons are necessary as a polarised target, deuterised materials are used, due to the lack of stable pure neutron materials.

Table 2.1: Magnetic moment [24] and the polarisation at thermal equilibrium for protons, deuterons and electrons

Particle	μ[J T^{-1}]	T[K]	$B = 2.5$ T	$B = 5$ T
electron	-9.2848×10^{-29}	77	2.18%	4.36%
		1	93.3%	99.8%
		0.05	100%	100%
proton	1.4106×10^{-26}	77	0.003%	0.007%
		1	0.26%	0.51%
		0.05	5.1%	10.18%
deuteron	4.3307×10^{-27}	77	0.0007%	0.001%
		1	0.05%	0.1%
		0.05	1.05%	2.09%

It is not reasonable to perform double polarisation experiments with such low nucleon polarisation, because the necessary measurement time for a specific statistical error goes with $\frac{1}{P^2}$. One way to reach higher values for the proton or deuteron polarisation is the brute force method. In this method, temperatures below 10 mK and magnetic fields up to 15 T are used to increase the polarisation. It is very difficult to realise temperatures this low for the polarised target at a particle experiment, due to the heating of

the beam. In addition, magnets to generate magnetic fields of around 15 T need a huge support structure and it is difficult to move them. The dilution refrigerator, described within this thesis, is designed for the usage inside a 4π-detector, to measure the reactions of the double polarisation experiments. This means, if an external magnet is used to create the polarisation, the possibility to replace the magnet with the detector is mandatory. The internal magnets, used to create or hold the polarisation, have to be as thin as possible. Otherwise, low energy particles are stucked in the surrounding refrigerator parts and can not be detected. Another disadvantage of the brute force method is the high build up time for the polarisation. Using the brute force method, it takes weeks or months to build up a polarisation high enough to measure reactions depending on the target polarisation.

Thus, the process of **D**ynamic **N**uclear **P**olarisation is used for the polarisation of the target material. With this method a higher polarisation at higher temperatures and lower magnetic fields can be achieved. Due to this method, a compromise between low temperatures, high magnetic fields, build up time of the polarisation and mobility of the external polarisation magnet can be found.

2.2 Dynamic Nuclear Polarisation

DNP is a method to transfer a high electron polarisation to the nucleon of the target material. For this, paramagnetic centres are necessary. If a spin-flip of this paramagnetic centres is induced, it is possible to translate the polarisation of the electron, via dipole-dipole coupling, to the nucleon. A simple model to explain the process is the **S**olid **S**tate **E**ffect (see next section). An enhanced description is given by the **E**qual **S**pin **T**heory (see Chap. 2.2.2). With the DNP method, a high proton or deuteron polarisation of the target can be reached in a few hours and provided for the scattering experiment.

2.2.1 Solid State Effect

The SSE was first observed by Abragam and Proctor within a Li-F sample [25]. In this case, the fluorine was used for the paramagnetic centres, necessary for the DNP process. Later, Abragam and Goldman described this effect with the dipole-dipole coupling for an electron and nucleon spin system [26]. The Hamiltonian of this system can be written by

$$\hat{H} = \left(\nu_e \hat{S}_z - \nu_I \hat{I}_z\right)_{\text{ZEEMAN}} + \left(c\hat{S}_z\hat{I}_+ + c^*\hat{S}_z\hat{I}_-\right)_{\text{dipole}} \simeq \hat{H}_Z + \hat{H}_D. \tag{2.9}$$

In this case, $\hat{S}_z$ is the operator for the z - component of the electron spin, $\hat{I}_z$ the operator for the z - component of the nucleon spin and ν_i is the LAMOR - frequency of the corresponding particle. $\hat{I}_\pm = \hat{I}_x \pm i\hat{I}_y$ are the operators to full-fill a spin flip and $c \sim \frac{\mu_B \mu_K}{r^3}$. The interaction between electron and nucleon is induced by their local magnetic fields. This results in a mixing of the states of the systems with the same electron spin, as described in [26]. The grade of this mixing is

$$|q| = \frac{c}{h\nu_p} \simeq \frac{B_S}{B_0} \approx 10^{-4}. \tag{2.10}$$

In Fig. 2.3, this is depicted for a spin-$\frac{1}{2}$-system. Due to the mixing of the states, it is possible to induce the forbidden transitions 1 and 3 by using microwaves with a frequency of $\nu = \left(\nu_\text{e} \pm \nu_\text{p}\right)$. As shown in Fig. 2.3, the orientation of the electron and the proton spin changes caused by this transition. Due to the allowed transitions 2 or 4, the electron spin flips back and the proton is polarised. For this process, Abragam and Goldman showed that the condition

$$T_{1\text{p}} \gg \frac{N_\text{p}}{N_\text{e}} T_{1\text{e}} \tag{2.11}$$

has to be fulfilled [26]. Eq. 2.11 shows that the relaxation time of the electron has to be much lower than the relaxation time of the proton, and that the ratio between protons and electrons that are able to do a spin flip is important. In target materials like chemical doped butanol, irradiated ammonia or ^{6}LiD, one electron flips the spins of $\sim 10^3$ protons before the first proton spin flips back.

The dipole coupling of this system goes with $\sim \frac{1}{r^3}$, so there are not many protons that can be reached by the electron [27], but the polarisation of the protons can propagate through the target by spin diffusion. If a proton spin flips back, it is possible that it transfers his polarisation to an other proton by the dipole coupling of the nucleons. In this way protons that can not be reached by electrons, can be polarised.

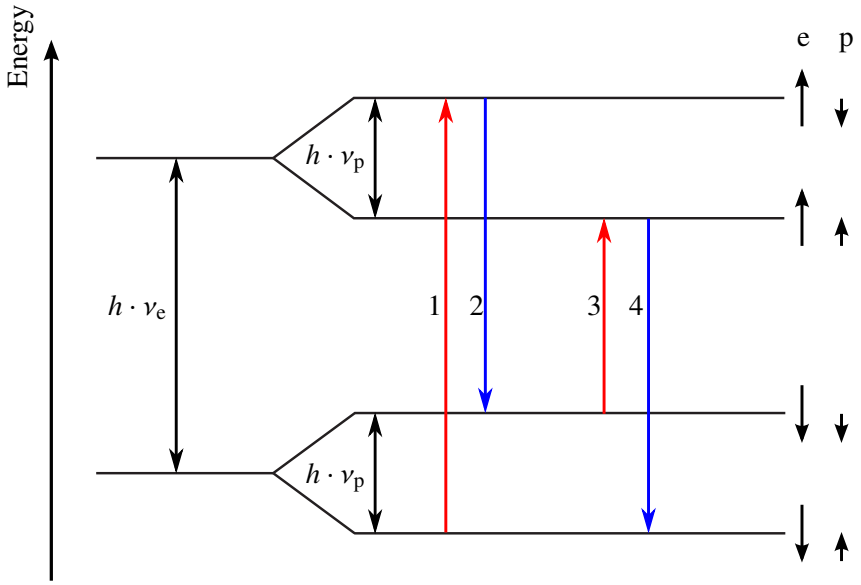

Figure 2.3: Zeeman splitting of an electron-proton system. The transitions in red are forbidden, the blue ones are allowed.

2.2.2 Equal Spin Temperature Theory

Most of the target materials, used for double polarisation experiments, can not be fully described by the simple model of the SSE. The fact that the coupling of the electron spins among each other is smaller than the ZEEMAN-coupling, but, due to the high electron density, is no longer negligible leads to an additional splitting of the energy levels. Then discrete ZEEMAN levels do no longer exist and the energy levels become a band structure like Fig. 2.4 (a) shows. An enhanced fitting model to describe

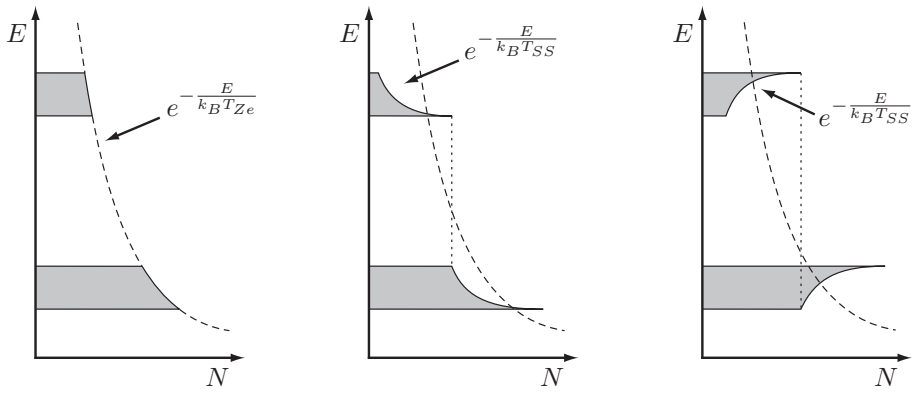

(a) $T_G = T_{SS} = T_{Ze}$ (b) $0 < T_{SS} < T_{Ze}$ (c) $|T_{SS}| < T_{Ze}$ $T_{SS} < 0$

Figure 2.4: Energy of the electrons in thermal equilibrium (**a**) and after the radiation of microwaves (**b** and **c**) [28]

the DNP for these materials is the **E**qual **S**pin **T**emperature theory, first introduced by Redfield [29] and described by S. Goertz et all [30]. In this section, only a rough description of the EST will be given. The population distribution of the spins follows the BOLTZMANN distribution and can be characterised with

the specific temperature reservoirs T_{Ze} and T_{Zp} that corresponds to the occupation of the electron and the proton ZEEMAN levels. T_{Ze} and T_{Zp} are in relationship with the polarisation by the occupation of the ZEEMAN levels. An additional temperature reservoir for the spacial distribution of the electron spins and for the lattice can be defined:

T_{SS} is the temperature of the spin spin coupling for the electrons and stands for the distribution of the spins in space.

T_L is the temperature of the lattice.

Now, an exchange of heat between all of this reservoirs is possible. Due to this, all four temperatures are equal in thermal equilibrium. If T_{Ze} is constant, only the average of the spins oriented to the external magnetic field axes is constant. For the explicit setup of the spins, leading to this polarisation, different spacial distributions are possible.

Under usage of microwaves with a frequency of $\nu_e - \delta$, where δ is the width of the ZEEMAN band, it is possible to induce a transition from the band with low energy to the band of higher energy. This energy $h\delta$, which is needed for the transition, is provided by changing the spacial spin distribution. It is shown in Fig. 2.4 (b). This leads to a lower T_{SS}, which results in an increased polarisation. Due to the contact between the electron spin-spin reservoir (T_{SS}) and the nucleon ZEEMAN reservoir (T_{Zp}), T_{Zp} follows T_{SS}. Under the use of microwaves with an frequency of $\nu_e + \delta$, the effect is the same but T_{SS} becomes negative (see Fig. 2.4 (c)).

2.3 The frozen spin technique and the continuous mode

In cases like the COMPASS experiment, there are several continuous operating polarised solid targets that reaches a polarisation up to 95 %[31][32]. Here, the target material is cooled to temperatures around 200 mK and polarised by the usage of microwaves with a frequency of 70 GHz and a magnetic field of 2.5 T. Normally, an external magnet is used for the polarisation. In the case of the CBELSA/TAPS experiment, a 4π acceptance is needed. This means that the geometry of the detector does not allow an external magnet during the experiment, because the aperture of the detector has a diameter of only 110 mm. Thus, the frozen-spin technique had to be used for the measurements at CB.

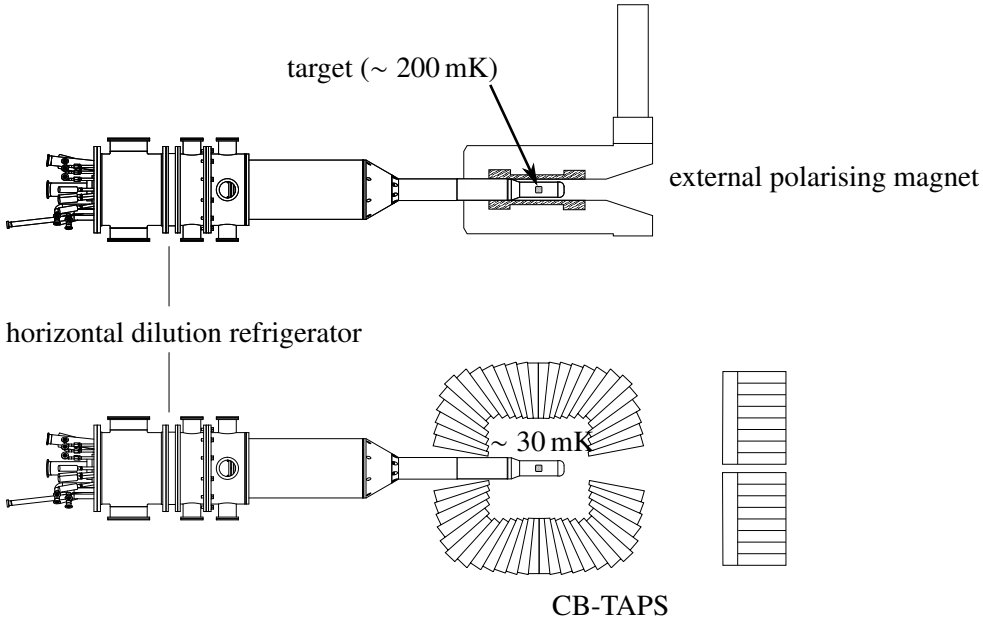

Figure 2.5: The frozen spin technique [33]

In Fig. 2.5 the principle of this frozen spin technique is illustrated. First, the target material will be polarised at low temperatures and an external magnetic field of 2.5 T by the usage of microwaves at $\approx$ 70 GHz. To obtain a magnetic field of this strength, an external polarisation magnet with an homogeneity of better than 10^{-4} is used. Afterwards the temperature is lowered as much as possible to sustain the relaxation of the protons. Then a holding coil with a magnetic field strength of $0.6 - 0.7$ T and a homogeneity of better than 10×10^{-3} is used to create a holding field, while the field of the polarisation magnet will be reduced down to $\underline{B} = 0$. At this point, the external polarisation magnet can be removed, the detector is pulled over the target and data collection can start. For transverse and longitudinal target polarisation, two different types of superconducting coils are used. More information about these coils is given in the thesis of Gehring [34].

This technique can be used to increase the relaxation time of the nucleon, but not to preserve the maximal reached polarisation. In the setup for the CB-ELSA experiment, relaxation times of 200 h to 600 h were reached as mentioned in [14] and [35]. Due to this, it is necessary to repolarise the target material every two or four days, depending on the relaxation time of the target material. Thus, for the frozen spin mode, only an average polarisation lower than the maximum polarisation is reached. This is illustrated in Fig. 2.6. First, the target will be polarised (black line) until the polarisation is high enough for the

experiment. Afterwards, the material is cooled down. The polarisation through this process is given in blue. The polarisation falls slow in the frozen-spin mode, due to the increased relaxation time at lower temperatures. The difference in the relaxation times during the cooling phase and the measuring phase comes from the different magnetic fields. During the cooling phase, the external polarisation magnet is used to sustain the polarisation. Afterwards, a holding magnet with a lower magnetic field is used for the measurement.

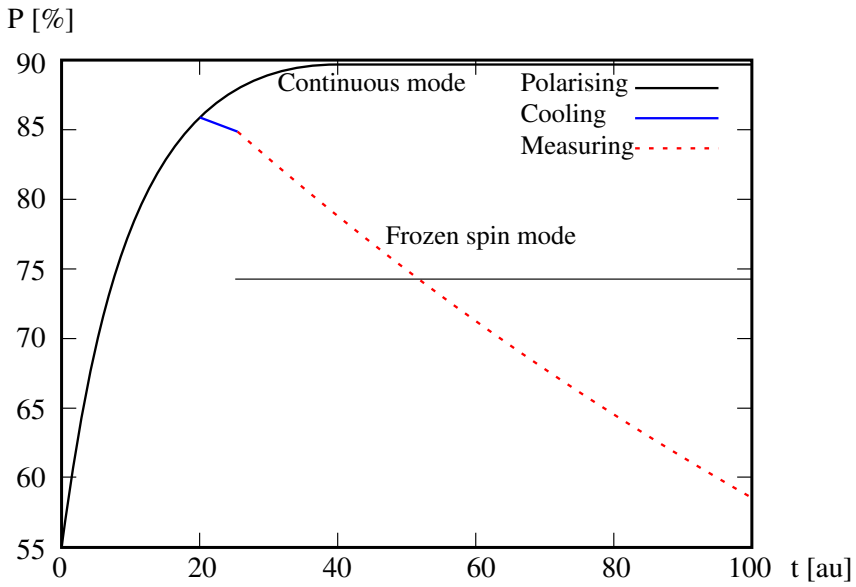

Figure 2.6: Polarisation for the frozen spin and the continuous mode. The diagram is inspired by Rohlof [36]

As in Chap. 1 mentioned, the figure of merit of a polarised target characterises the quality of the target. Thus, the necessary measurement time to reach a specific statistical significance depends on the FoM, given in Eq. 1.4. An important parameter for increasing the FoM is to increase the target polarisation P_T. For the frozen spin mode, it is the average target polarisation during the data taking. Reducing the target temperature would increase the relaxation time of the target polarisation and, due to this, it will increase the average polarisation during the data taking. If a continuous polarised target is used, P_T is the maximum polarisation which could improve the FoM by a factor of two, compared to a frozen spin target. For both concepts, a good performing cooling machine is necessary. In the case of the polarised target for CBELSA/TAPS, a dilution refrigerator is used. This refrigerator cools the target material with a ^{3}He-^{4}He mixture.

This work aims to provide a continuous mode target for the CB detector for a longitudinal polarisation. To reach this goal, an internal superconducting polarising magnet is necessary. A first design can be found in [36]. The problem of this concept was, due to some winding errors, the necessary homogeneity of $\sim 10^{-4}$ could not be reached. Based on this, Fehér recalculated an inverse notched coil [37]. With this design, it should be easier to reduce the winding errors and obtain the necessary homogeneity. This superconducting coil, operated with a Current of ~ 90 A, gives a magnetic field strength of 2.5 T. Afterwards, several tests were done by Bornstein [38] to improve the winding process.

Thus, the parameter for the new dilution refrigerator, which was designed for the experiment are given below:

- Support for high current (90 A) internal superconducting coils for the usage of an internal longitudinal polarisation magnet
- High cooling power at temperatures of 200 mK for continuous polarisation during the experiment
- Minimal temperature of 30 mK for high relaxation times in frozen-spin mode. This is necessary for transverse polarised targets
- Maximum diameter of 94 mm for the target region due to the geometry of the detector and the geometry of the external polarisation magnet for frozen-spin mode (⊘ 95 mm)

The design of the refrigerator was created by Dutz [18]. This refrigerator uses a ^{3}He-^{4}He mixture to cool the target material and the mixture is cooled and liquefied by liquid ^{4}He before it enters the central part of the refrigerator, the so called dilution unit. Helium is an important liquid in cryophysics and has many applications. In the following, the physical properties of helium are summarised, which are important for the construction and the operation of a dilution refrigerator.

Chapter 3

Cooling Fundamentals

As mentioned before, temperatures below 1 K are necessary for a polarised solid target. Cryogenics, 'the production of coldness', is a branch of physics that studies methods to obtain temperatures well below room temperature and methods to measure these temperatures. Normally, the lowest temperature existing in the universe is $\sim$ 2.7 K. This is the background temperature depending on the presence of the microwave background, 'fossil photons', of the big bang [39]. It is possible to reach temperatures down to $\sim$ 500 pK, but only for a small number of atoms or molecules. If a large amount of material and higher cooling power is needed, cooling methods with cryo-liquids are more common.

There are several liquids in use in cryophysics like liquid oxygen, hydrogen, argon or nitrogen, depending on the temperature. If it is necessary to reach temperatures $\ll$ 20 K (for liquid oxygen) helium is the only possible liquid, due to its boiling point. For polarisation experiments, it is necessary to cool a 'huge' amount of target material to temperatures below 1 K. To compensate heating from the microwave system, the particle beam and other sources, a good performance and a high cooling power are indispensable. Nowadays, temperatures around 1 K can be easily obtained by means of refrigerators using the evaporation process of helium. This principle is used for different cooling parts in the described refrigerator.

To reach temperatures below 300 mK, a ^{3}He-^{4}He mixture has to be used. This mixture circulates in a closed system and cools the target material. The so called dilution unit is the most important part of a dilution refrigerator, operating with this principle.

This chapter will describe the relevant physical properties of helium to build a high performance dilution refrigerator. A more detailed description of the properties of ^{3}He and ^{4}He is given by the book of Keller [40]. Afterwards, there will be an explanation of the dilution effect and how it will be used to reach temperatures around 30 mK in a dilution refrigerator.

3.1 Liquid helium

Helium is inert, non-corrosive, non-flammable, and one of the most interesting and most used elements in cryophysics. There exist two stable isotopes: ^{4}He, which is a boson with nuclear spin $I = 1$, and ^{3}He, which is a fermion with nuclear spin $I = \frac{1}{2}$.

In nature, ^{3}He is present with a concentration of $\sim 10^{-7}$ of that of ^{4}He and the separation is not effective. It is obtained as byproduct of the tritium production in nuclear reactors by the beta decay of tritium. Due to the high costs of ^{3}He, it is used in a closed system.

In Appendix A.1 the thermophysical properties of the two helium isotopes are summarised. Helium has a very low boiling and critical point, low density and no triple point. Also, there exists a superfluid phase for ^{4}He and ^{3}He.

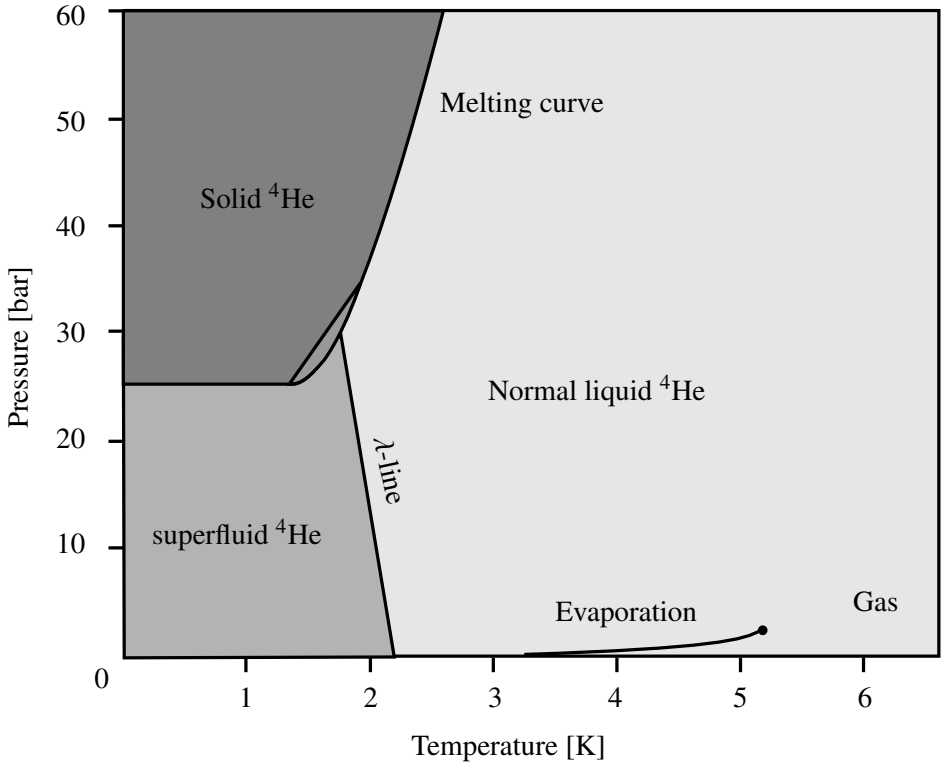

Figure 3.1: Phase diagram of ^{4}He

Fig. 3.1 and Fig. 3.2 (Data from [41]) show the phase diagrams of the two isotopes. Note that a zone with changing slope is present in the melting curve in Fig. 3.2. These properties are due to the fact that the zero-point energy of helium is large owing to its small atomic mass and the very weak Van der Waals force between the atoms. Also, note the different temperature scales in these diagrams. Thus, it is possible to reach lower temperatures by the evaporation of ^{3}He instead of ^{4}He (see Chap. 3.1.1). In the temperature region above 30 mK, where the dilution refrigerator described in this thesis should operate, only ^{4}He has the possibility to get superfluid.

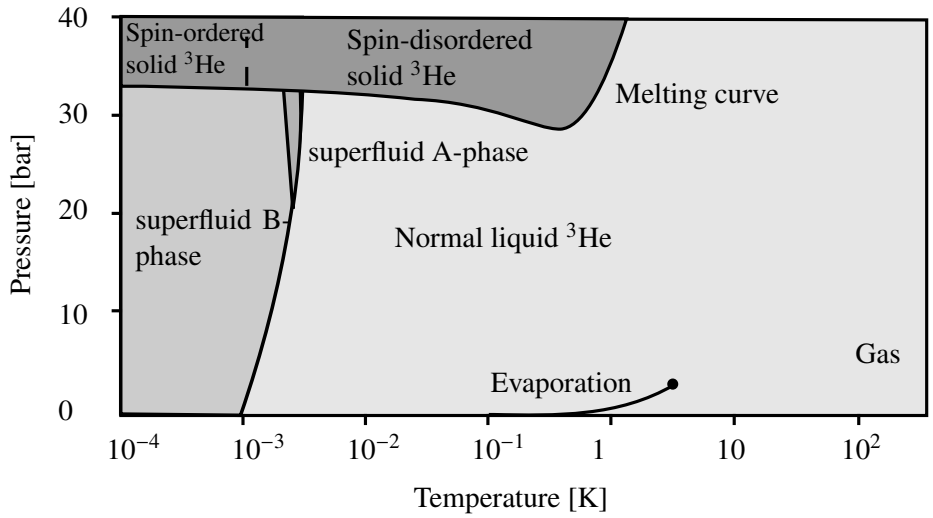

Figure 3.2: Phase diagram of ^{3}He

3.1.1 Latent heat and evaporation

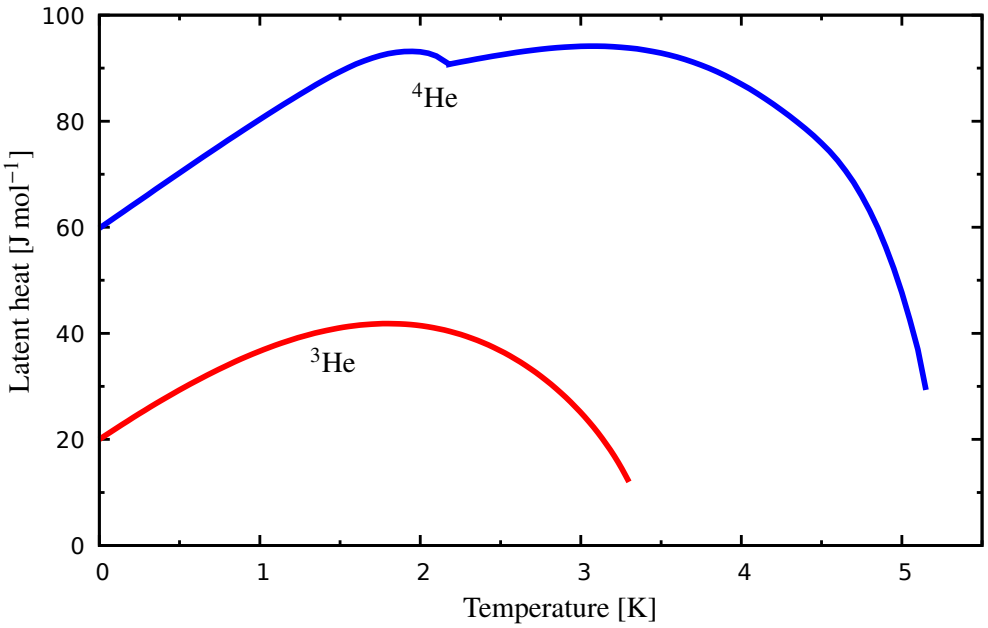

Figure 3.3: Latent heat of the two helium isotopes used in a dilution refrigerator [42]

The latent heat and the vapour pressure are fundamental parameters for using cryogenic liquids in a refrigeration process. In this process, a bath of a liquid is cooled by lowering the vapour pressure of the liquid. The cooling power of this process is then proportional to the latent heat. This leads to high cooling power, if the latent heat L has a large value. The vapour pressure can be calculated by the

Clausius-Clapeyron equation

$$\left(\frac{\mathrm{d}p}{\mathrm{d}T}\right)_{\mathrm{vap}} = \frac{S^{\mathrm{gas}} - S^{\mathrm{liq}}}{V_{\mathrm{m}}^{\mathrm{gas}} - V_{\mathrm{m}}^{\mathrm{liq}}} \approx \frac{L(T)}{RT^2} \cdot p, \tag{3.1}$$

with S the entropy and V_{m} the molar Volume. The difference of the entropy for the liquid and the gaseous state is the latent heat over the temperature. Also, the molar volume of the gas is much larger than the molar volume of the liquid, so that the volume of the liquid is negligible and the difference of the molar volumes can be written as $\frac{RT}{p}$. Then, the vapour pressure is given by

$$p_{\mathrm{vap}}(T) \propto e^{-\left(\frac{L}{RT}\right)}, \tag{3.2}$$

where it is assumed that the latent heat is approximately constant. Fig. 3.3 shows that the latent heat is a function of the temperature, but as a rule of thump Eq. 3.2 is a good assumption. If a bath of liquid helium is pumped, helium particles will evaporate, resulting in cooling of the remaining bath. In this case, the cooling power depends on the latent heat and the amount of particles removed from the bath

$$\dot{Q} = \dot{n} \cdot L \qquad \text{with} \qquad \dot{n} = k \cdot p_{\mathrm{vap}}(T). \tag{3.3}$$

$\dot{n}$ in Eq. 3.3 is given for the usage of a volumetric pump. With Eq. 3.3 and 3.2, the cooling power of the evaporation process of liquid helium can be written as

$$\Rightarrow \dot{Q} \propto kL \cdot e^{-\left(\frac{L}{RT}\right)}. \tag{3.4}$$

Due to p_{vap}, the cooling power decreases exponentially. Finally, a limit temperature is reached at which the cooling power, supplied by the evaporating particles, is balanced to the external heat input. With this simple cooling process, it is possible to reach temperatures of:

- ^{4}He: $\sim 800\,\mathrm{mK}$
- ^{3}He: $\sim 300\,\mathrm{mK}$

A ^{4}He refrigerator is used, by the Bonn polarised target group, to perform polarisation measurements for new target materials [32] [43]. As will be described in Chap. 5, the evaporation process of ^{4}He is also used in the dilution refrigerator, described in this thesis, in the precooling stages to precool and liquefy the incoming mixture and to cool the internal superconducting magnet.

3.1.2 Specific heat and superfluid helium

Compared to other materials, helium has a large specific heat in the temperature range of a polarised target (see Fig. 3.4). This large specific heat, compared to other materials at low temperatures, makes it possible to cool other materials with helium with high efficiency. This means that the temperature of a refrigerator rapidly follows any temperature changes of its refrigerating helium bath.

Many of the properties of a material are revealed by its specific heat and at low temperatures. These properties are influenced by statistical or quantum effects. As Fig. 3.5 shows, the heat capacity of ^{4}He has a very prominent peak at a temperature of about 2.17 K at saturated vapour pressure. This peak indicates a phase transition to a new state of the liquid. Above the so called λ-transition, ^{4}He behaves

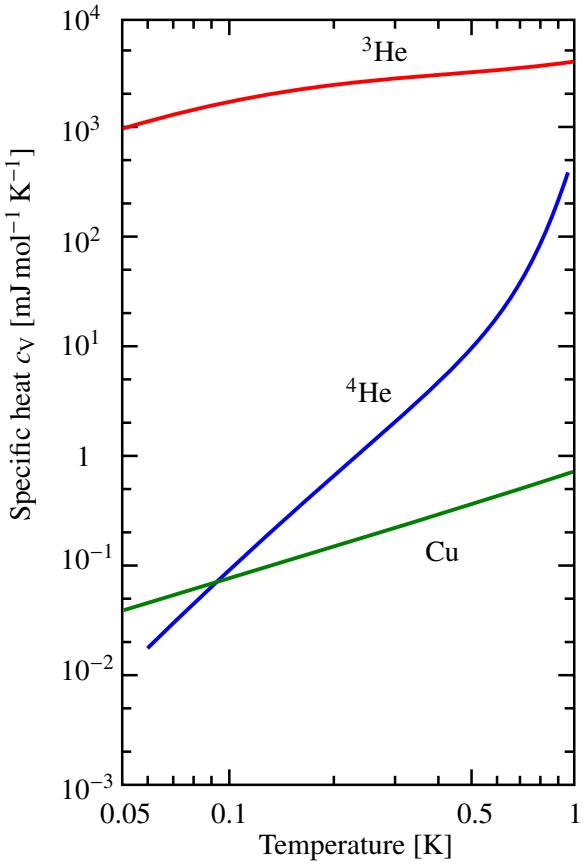

Figure 3.4: Specific heat of liquid helium at vapour pressure compared to the specific heat of Cu. Data from [44],[45] and [46].

like a classical fluid or, due to its low density, as a classical gas (called ^{4}He I). Below the λ-transition (^{4}He II, the superfluid ^{4}He), its entropy and specific heat decrease rapidly with the temperature, due to its Bose-Einstein condensation. For more details see [48].

^{4}He in its normal fluid state (^{4}He I), above 2.17 K, shows transport properties like a classical gas. The same applies to liquid ^{3}He above 10 mK. Conversely, if $T < T_\lambda$, where T_λ is the critical temperature for the transition to the superfluid state at a specific pressure, the thermal conductivity of ^{4}He II is infinity for ideal experimental conditions, where no heat flow occurs, or under realistic conditions it is finite but quite large compared to other materials. This high thermal conductivity makes ^{4}He II a very efficient medium for establishing temperature homogeneity. Below 0.4 K and at $p \leq 2$ bar the thermal conductivity is given by

$$\kappa_4 \propto 20 d T^3 \ \mathrm{W\,K^{-1}\,cm^{-1}}, \tag{3.5}$$

where d is the diameter of the helium column in centimetres [49]. Keller [40] and Wilks[50] gave a detailed description for the thermal transport properties of helium. Another consequence of the superfluid state is that ^{4}He II has a vanishing viscosity ($\eta_s = 0$) for flow through fine capillaries. It is superfluid until a critical velocity is reached, similar to the critical current in a metallic superconductor. Thus, the viscosity is smaller than for its gaseous state.

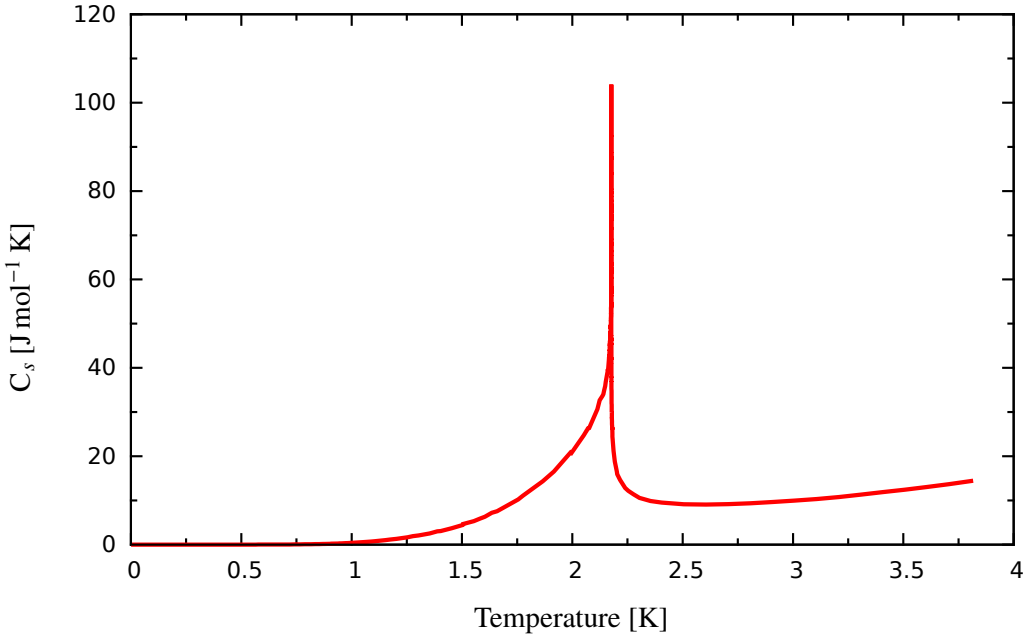

Figure 3.5: Heat capacity of liquid ^{4}He at saturated vapour pressure (Data from [47])

This is a challenge for the construction of refrigerators for temperatures below 2 K. An apparatus which seems to be leak tight at higher temperatures may suddenly develop a so called superleak, when superfluid helium has contact to the structure. Also, the superfluid can flow up walls against gravitational forces. In constructing a dilution refrigerator, a superfluid film, flowing out of the thermal sinks or the dilution unit described later, has to be avoided.

3.2 The dilution effect

Since the cooling by evaporation of a pure ^{4}He or ^{3}He bath does not meet the requirements of the polarised target for the CBELSA/TAPS experiment, a dilution refrigerator has been built. In this case, a mixture of ^{3}He and ^{4}He is used to reach temperatures below 300 mK. The phase diagram at saturated vapour pressure is presented in Fig. 3.6. The phase diagram shows that the super fluid transition temper-

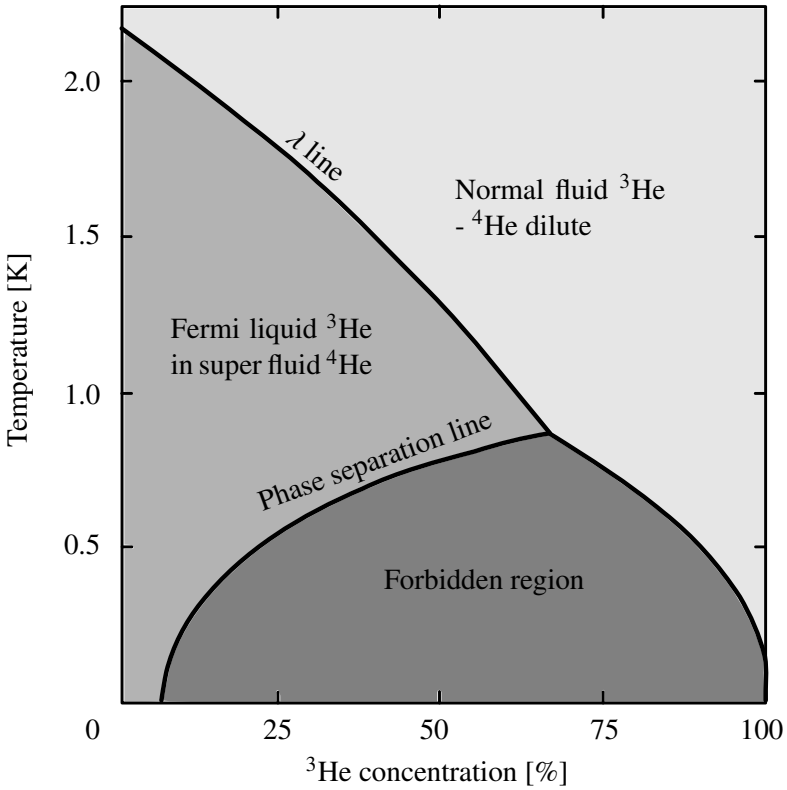

Figure 3.6: Phase diagram of the ^{3}He-^{4}He dilute [42]

ature, for the fluid, is decreased by the ^{3}He. Below the temperature of the tricritical point (0.867 K), the two isotopes can no longer be admixed at all ratios. If a helium mixture is cooled below this temperature, the liquid will spontaneous separate into two phases:

- A ^{3}He rich phase, which floats on top due to its lower density. If the temperature is decreased close to zero, this liquid becomes pure ^{3}He.

- A ^{4}He rich phase, where the concentration of the diluted ^{3}He does not approach zero if the temperature approaches 0 K. At this temperature the dilute reaches a constant concentration of 6.6%.

This finite solubility is of utmost importance for a dilution refrigerator. The limiting concentrations of the diluted isotopes on the phase separation line at saturated vapour pressure are given by

$$x_{^4\mathrm{He}} = 0.85 T^{\frac{3}{2}} \cdot \mathrm{e}^{-\frac{0.56}{T}} \text{ [51]}, \tag{3.6}$$

$$x_{^3\mathrm{He}} = 0.066\left(1 + 8.3T^2\right) \quad (\text{for } T < 0.1\,\mathrm{K}) \text{ [52]}. \tag{3.7}$$

The cooling in a dilution refrigerator is achieved by transferring ^{3}He atoms from the concentrated to the diluted phase. The cooling capacity in this process is the heat of mixing of the two isotopes

$$\dot{Q} = \dot{n}_3 \left[H_{\mathrm{dil}}(T) - H_{\mathrm{con}}(T) \right]. \tag{3.8}$$

Whereby H_{con} is the enthalpy of the concentrated ^{3}He phase. At temperatures below 100 mK, the concentration is above $x_{^3\mathrm{He}} > 99\%$ and the phase behaves like a Fermi liquid. The enthalpy is then given by

$$\begin{aligned} H_{\mathrm{con}}(T) &= H_3(0) + \int_0^T c_p d\bar{T}, \\ \Rightarrow\ H_{\mathrm{con}}(T) &= H_3(0) + 11T^2\ \mathrm{J/molK^2}. \end{aligned} \tag{3.9}$$

Below 50 mK, the specific heat of ^{3}He follows approximately $c_p = 22 \cdot T$ J/molK [45]. The diluted side is composed of $\sim 7\%$ ^{3}He in ^{4}He. Below 500 mK, this admixture is super fluid and does not interact with other particles. The enthalpy of the mixture can be described with the equations of a Fermi gas with $c_p = 108 \cdot T$ J/molK below 40 mK and whereby an effective mass $m^\star$ equal to 2.34 times the mass of an ^{3}He atom, to take the influence of the neighbouring ^{4}He atoms into account. If both phases are in thermodynamic equilibrium, they have the same chemical potential

$$\mu = H - TS. \tag{3.10}$$

At temperatures below 200 mK the entropy of Fermi liquids equals the heat capacity. This leads to

$$\begin{aligned} H_{\mathrm{con}}(T) - T \cdot S_{\mathrm{con}}(T) &= H_{\mathrm{dil}}(T) - T \cdot S_{\mathrm{dil}}(T), \\ \Rightarrow\ H_{\mathrm{dil}}(T) &= H_{\mathrm{con}}(T) + T \cdot \left[S_{\mathrm{dil}}(T) - S_{\mathrm{con}}(T) \right] \\ &= H_3(0) + 95T^2\ \mathrm{J/molK^2}. \end{aligned} \tag{3.11}$$

$\dot{n}_3$ is the ^{3}He circulation rate, T_0 the temperature of the incoming liquid and T_{mc} the temperature of the outgoing ^{3}He. The cooling power at the phase boundary can be calculated by Eq. 3.8 with the usage of Eq. 3.9 and 3.11

$$\begin{aligned} \dot{Q} &= \dot{n}_3 \left[H_{\mathrm{dil}}(T_{\mathrm{mc}}) - H_{\mathrm{con}}(T_0) \right] \\ &= \dot{n}_3 \cdot \left[95 \cdot T_{\mathrm{mc}}^2 - 11 \cdot T_0^2 \right] \mathrm{J/molK^2} \qquad (3.12) \\ \Rightarrow\ \dot{Q} &= \dot{n}_3 \cdot 84 \cdot T_{\mathrm{mc}}^2\ \mathrm{J/molK^2}, \qquad (3.13) \end{aligned}$$

where Eq. 3.13 shows the maximum cooling power in a discontinuous operation mode, when no further ^{3}He is supplied to the mixing chamber and $T_0 = T_{\mathrm{mc}}$. If T_0 is close to T_{mc}, the cooling power goes with T_{mc}^2. As Eq. 3.8 shows, ^{3}He diffusing across the phase boundary from the concentrated to the diluted phase absorbs heat analogous to the evaporation process of a liquid into a gas. For a continuously dissolve of ^{3}He atoms from the concentrated to the diluted phase, the balance of these two phases has to be disturbed. This has to be done by distillation of the ^{3}He from the diluted phase which creates an osmotic pressure that makes an continuous ^{3}He circulation possible. All dilution refrigerators work with this principle, introduced by London and Clarke [53].

Fig. 3.7 shows the basic components of a dilution refrigerator. The three core components of the dilution refrigerator are the mixing chamber, the still and the heat exchanger between them. The mixing chamber contains the two separated phases. The diluted phase is connected to the still through an heat exchanger. This heat exchanger cools the incoming ^{3}He before it enters the mixing chamber. Inside the

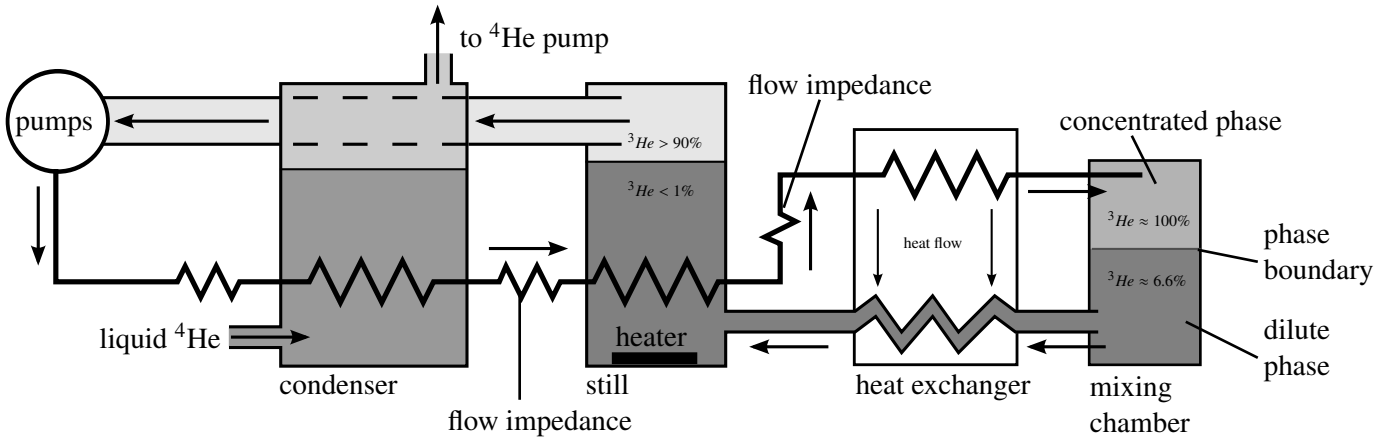

Figure 3.7: Principle of a dilution refrigerator

still, a heater has to be used to heat the liquid to around 700 mK to increase the vapour pressure of ^{3}He. This leads to an evaporation of the ^{3}He out of the diluted liquid at the still. Due to the different ^{3}He concentrations between still and mixing chamber, an osmotic pressure between them occurs and ^{3}He streams from the mixing chamber to the still. Now, the balance between the two phases is disturbed and ^{3}He from the concentrated side can diffuse into the diluted side. For a continuous operating refrigerator, the distilled ^{3}He will be removed from the refrigerator and then refilled and liquefied in a condenser. In Chap. 5 the details of each part for a real horizontal dilution refrigerator will be discussed and presented.

3.3 Kapitza Resistance

At temperatures below 1 K, the thermal boundary resistance between liquid helium and a solid is refereed to as Kapitza resistance. In this temperature region, the heat transfer between solid and liquid is dominated by thermal phonons. The acoustic impedance, which are the product of density and first sound of velocity, of most solids differ by more then two orders of magnitude from that of liquid helium. This mismatch interferes with the passage of the thermal phonons across the interface and reduces the transmission. At the boundary, this leads to a discontinuity ΔT in the temperature distribution, which is given for a small heat transfer $\dot{Q}$ across the interacting surface A by

$$\Delta T_{\mathrm{Kap}} = \frac{\rho_{\mathrm{Kap}} \cdot \dot{Q}}{A}. \tag{3.14}$$

The Kapitza resistance ρ_{KAP} depends on the properties of the solid, the pressure of the liquid and the temperature. In Fig. 3.8 the resistivity between a copper sintered material and the helium streams inside the dilution unit is shown. It can be seen that the Kapitza resistance increases strongly with decreasing temperature.

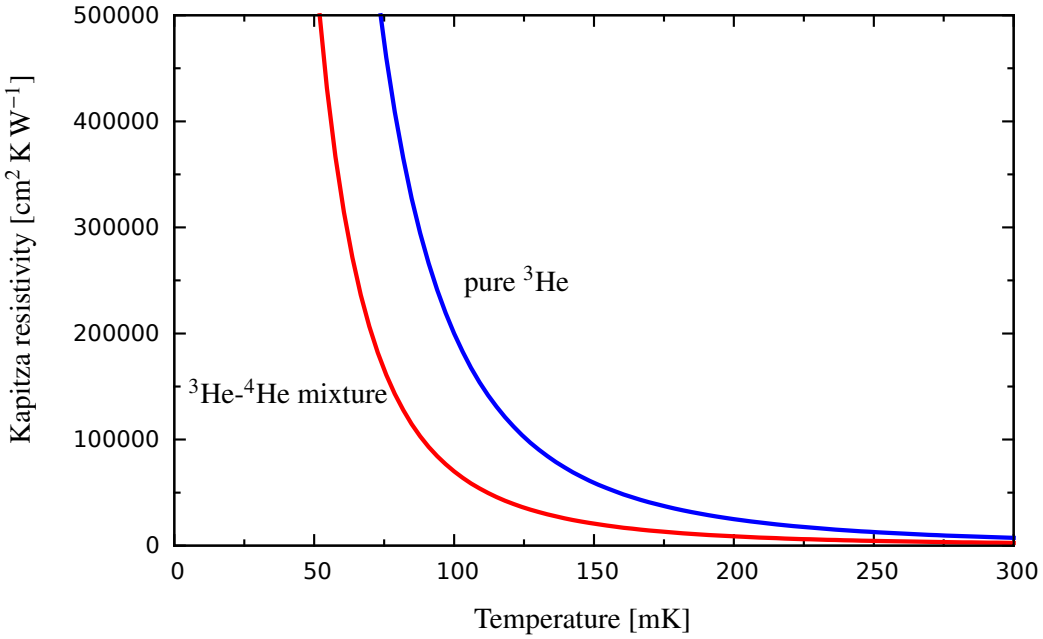

Figure 3.8: Kapitza resistance for pure ^{3}He and a ^{3}He-^{4}He mixture in a copper sintered heat exchanger [54][55]

The Kapitza resistance is of major importance for the performance of the heat exchanger between the still and the mixing chamber of a dilution refrigerator. To reach the necessary cooling power, those heat exchangers need a huge surface area between the liquids and the solid. Thus, the Kapitza resistance has a huge influence on the design for such a heat exchanger.

Chapter 4

CFD-Simulations

For the design of a dilution refrigerator the cooling power of the different heat exchangers has to be calculated. The initial calculations for the cooling stages of the precooling were done similar to Bradtke [13], Borisov [56] and Pobell [42], based on energy conservation for each stream. The main challenge for the calculation of heat exchangers used in horizontal dilution refrigerators is the determination of the heat exchange between the different streams through the solid

$$\dot{Q}_{\text{solid}}(\Delta T_{\text{m}}) = \alpha \cdot A \Delta T_{\text{m}} \quad \text{with} \quad \alpha \propto \text{Nu}(\text{Re}, \text{Pr}) \cdot \frac{\lambda}{L}. \tag{4.1}$$

α is the heat transfer coefficient at the surface area and A the surface area itself. λ corresponds to the thermal conductivity and L to the length of the heat conducting part. Nu is the Nusselt number, which depends on the Reynolds/Prandtl number Re/Pr referring to Prandtl [57]. This three values are used to characterise the stream behaviour. Equation 4.1 shows that the heat exchange depends on the characteristic flow parameter and the geometry. Unfortunately, it can be a great challenge to determine these numbers. For the initial calculations, the Prandlt and the Reynolds numbers for the ^{3}He-^{4}He mixture back stream were estimated to be Pr = 0.7 and Nu = 3.66. For the other streams, the fluid flows through tubes and the calculations by Bradtke [13] were used, for the calculation of Re and Pr see [19]. Nevertheless, the characteristic flow parameters are used to rewrite the Navier-Stokes equation with dimensionless parameters to characterise the fluid behaviour. If it is possible to solve the Navier-Stokes equation in a direct way, this flow parameter can be avoided.

The calculation is also more complicated, due to the fact that the heat exchangers in this refrigerator are counter flow heat exchangers with three or four streams. In the past, all calculations were done for two stream counter flow heat exchangers and the influence of the back streaming ^{3}He-^{4}He mixture to the cooling of the heat exchangers was ignored.

Thus the Navier-Stokes equations were solved for the precooling stages of the dilution refrigerator, described in this thesis. For this, a **F**inite **V**olume **E**lement method was used. Then the different fluid streams and the heat exchangers are discretised in finite volume cells, where it is possible to solve the Navier-Stokes equations in a direct way. Convergence of the system is reached by a suiting algorithm. This method is called **C**omputational **F**luid **D**ynamics and has many applications in engineering. The idea to use this simulations for a dilution refrigerator was to adapt this principle for the precooling of the circulating ^{3}He-^{4}He mixture. In this section of the refrigerator, ^{3}He and ^{4}He behave like an ideal fluid until the temperatures for a superfluid phase transition are reached.
These simulations were performed with OpenFOAM [58]. The meshes for the calculation were created with the included mesh generating code called snappyHexMesh. This chapter will give a brief introduction into CFD-Simulations with a finite volume method and into the physical basics which were used for the simulations.

4.1 Governing equations of conservation

The basis of these simulations are the Navier-Stokes equations which consider the continuity equation, the equations for the conservation of the momentum and for the energy. The fluid behaviour can be described by these three equations where the fluid parameters:

- $\underline{u}$ the fluid velocity,
- T the temperature of the fluid
- h the enthalpy or the inner energy e of the fluid,
- p the pressure,

and the fluid properties:

- ρ the density,
- η the dynamic viscosity,
- k the heat conductivity of the fluid

are expressed as a function of space and time, where their balance is evaluated on a fixed volume of space traversed by the fluid. Hence, the system can be described by a set of partial differential equations. In this case, the Eulerian approach is used, as it allows to separate the time dependence from the spatial dependence. The simulations, that were performed within the scope of this thesis, are all steady state problems and the contribution of time variation is zero. If the Lagrangian approach would be used, the time dependency, even for a steady state phenomenon remains due to its connection to the integration volume that must be followed and which varies as a function of time. It is possible to write an equation of conservation of a generic physical property ϕ in a control volume Ω delimited by the boundary surface S by

$$\frac{\mathrm{d}}{\mathrm{d}t}\int_{\Omega}\rho\phi\left(\underline{x},t\right)\,\mathrm{d}\Omega = \int_{\Omega}Q_{\phi}\,\mathrm{d}\Omega + \int_{\Omega}D_{\phi}\,\mathrm{d}\Omega. \tag{4.2}$$

The left side of Eq. 4.2 represents the total variation in time of the physical parameter ϕ

$$\frac{\mathrm{d}}{\mathrm{d}t}\int_{\Omega}\rho\phi\left(\underline{x},t\right)\,\mathrm{d}\Omega = \frac{\partial}{\partial t}\int_{\Omega}\rho\phi\left(\underline{x},t\right)\,\mathrm{d}\Omega + \int_{S}\rho\phi\left(\underline{x},t\right)\underline{u}\cdot\underline{n}\,\mathrm{d}S. \tag{4.3}$$

$\underline{u}$ is the fluid velocity. D_{ϕ} and Q_{ϕ} in Eq. 4.2 are source terms for the fluid parameter ϕ. Afterwards Eq. 4.2 can be rewritten

$$\frac{\partial}{\partial t}\int_{\Omega}\rho\phi\left(\underline{x},t\right)\,\mathrm{d}\Omega + \int_{S}\rho\phi\left(\underline{x},t\right)\underline{u}\cdot\underline{n}\,\mathrm{d}S = \int_{\Omega}Q_{\phi}\,\mathrm{d}\Omega + \int_{\Omega}D_{\phi}\,\mathrm{d}\Omega. \tag{4.4}$$

Due to the surface integral, the value ϕ can not be calculated for all points in the control domain. This issue can be solved by the Gauss theorem in order to translate the surface integral to a volume integral

$$\int_{S}\rho\phi\left(\underline{x},t\right)\underline{u}\cdot\underline{n}\,\mathrm{d}S = \int_{\Omega}\nabla\cdot\left(\rho\phi\left(\underline{x},t\right)\underline{u}\right)\,\mathrm{d}\Omega, \tag{4.5}$$

$$\Rightarrow\ \frac{\partial}{\partial t}\int_{\Omega}\rho\phi\left(\underline{x},t\right)\,\mathrm{d}\Omega + \int_{\Omega}\nabla\cdot\left(\rho\phi\left(\underline{x},t\right)\underline{u}\right)\,\mathrm{d}\Omega = \int_{\Omega}Q_{\phi}\,\mathrm{d}\Omega + \int_{\Omega}D_{\phi}\,\mathrm{d}\Omega. \tag{4.6}$$

If the control volume is constant in time, it is possible to express the balance equation by the partial derivative without reference to a particular volume

$$\frac{\partial}{\partial t}(\rho\phi) + \underbrace{\nabla \cdot \left(\rho \underline{u} \phi\right)}_{F_\phi} = D_\phi + Q_\phi. \tag{4.7}$$

The source terms are defined as follows:

- F_ϕ: convective flow, describes the transport of the stream given by ϕ
- D_ϕ: diffusive flow, describes the changes in space given by ϕ
- Q_ϕ: all other distributions given by ϕ

With the Source terms given in Tab. 4.1, the equations of conservation for a compressible fluid model can be written as:

$$\begin{aligned}
&1. \quad \frac{\partial \rho}{\partial t} + \nabla \cdot \left(\rho \underline{u}\right) = 0 \\
&2. \quad \frac{\partial}{\partial t}\left(\rho \underline{u}\right) + \nabla \cdot \left(\rho \underline{u}\underline{u}\right) = \nabla \cdot \underline{\underline{\sigma}} + \rho \underline{g} \\
&3. \quad \frac{\partial \rho h}{\partial t} + \nabla \cdot \left(\rho \underline{u} h\right) = \frac{\partial p}{\partial t} + \underline{u} \cdot \nabla p + \nabla(k \nabla T) + \nabla \cdot \left(\underline{\underline{\tau}} \cdot \underline{u}\right)
\end{aligned} \tag{4.8}$$

$\underline{\underline{\sigma}}$ is the stress tensor which describes the deforming forces in the fluid and $\underline{g}$ is the gravity. This system of equations is the basis of the CFD-simulations performed for the dilution refrigerator. The following sections will describe this equation system in more detail.

Table 4.1: Source terms for a compressible fluid flow

Equation	ϕ	D_ϕ	Q_ϕ
1. Continuity	1	0	0
2. Motion	$\underline{u}$	$\nabla \cdot \underline{\underline{\sigma}}$	$\rho \underline{g}$
3. Energy	h	$\nabla (k \nabla T)$	$\frac{\partial p}{\partial t} + \underline{u} \cdot \nabla p + \nabla \cdot \left(\underline{\underline{\tau}} \cdot \underline{u}\right)$

4.1.1 Continuity equation

Using Eq. 4.6, the continuity or mass conservation equation follows by setting the fluid parameter $\phi = 1$

$$\frac{\partial}{\partial t} \int_\Omega \rho \, \mathrm{d}\Omega + \int_\Omega \nabla \cdot \left(\rho \underline{u}\right) \mathrm{d}\Omega = 0. \tag{4.9}$$

Due to the fact that no additional mass sources exist, Q_ϕ and D_ϕ are assumed to be zero. Using a infinitesimal small control volume, this leads to a differential coordinate-free form of the continuity equation

$$\frac{\partial \rho}{\partial t} + \nabla \cdot \left(\rho \underline{u}\right) = 0. \tag{4.10}$$

This means that the change of mass for a specific volume in time equals the sum of the incoming and outgoing masses of this volume. If the fluid is incompressible, which is assumed if the Mach number is

below 0.3, the density is approximately constant which leads to:

$$\nabla \cdot \underline{u} = 0 \tag{4.11}$$

4.1.2 Momentum equation

Similar to the section above, Eq. 4.6 can be used to find an equation for momentum conservation. Thus, setting the parameter ϕ to the fluid velocity $\underline{u}$, for a fixed, fluid-containing volume of space, leads to

$$\frac{\partial}{\partial t}\int_\Omega \rho \underline{u}\,\mathrm{d}\Omega + \int_\Omega \nabla \cdot \left(\rho \underline{\underline{uu}}\right)\,\mathrm{d}\Omega = \int_\Omega Q_{\underline{u}}\,\mathrm{d}\Omega + \int_\Omega D_{\underline{u}}\,\mathrm{d}\Omega. \tag{4.12}$$

The left side of this equation shows the change of the motion in time and the incoming and outgoing motion flows. To express the right side in terms of explicit properties, one has to consider the forces which may act on the fluid in a control volume:

- For $D_{\underline{u}}$ they are represented by surface forces like the pressure, normal and shear stresses and surface tension
- $Q_{\underline{u}}$ can be represented by body forces like the gravity

The surface forces, due to pressure and stresses, are the microscopic momentum fluxes across a surface. They can lead to a system of equations which is not closed, if these fluxes cannot be written in terms of the fluid properties. It can be avoided by the assumption of a Newtonian fluid. This means that the viscous stresses arising from its flow are linearly proportional to the local strain rate which is the rate of change of its deformation over time. Then the stress tensor $\underline{\underline{\sigma}}$ can be written as

$$\underline{\underline{\sigma}} = -\left(p + \frac{2}{3}\eta \nabla \cdot \underline{u}\right)\mathbb{1} + 2\eta \underline{\underline{S}}. \tag{4.13}$$

In this case, η represents the dynamic viscosity, $\mathbb{1}$ is the unit tensor, p the static pressure and $\underline{\underline{S}}$ represents the rate of strain or deformation tensor

$$\underline{\underline{S}} = \frac{1}{2}\left(\nabla \cdot \underline{u} + \left(\nabla \cdot \underline{u}\right)^{\mathrm{T}}\right). \tag{4.14}$$

Using the Newtonian stress tensor and $\underline{g}$ representing the body forces due to gravitation the momentum conservation equation can be written by

$$\frac{\partial}{\partial t}\int_\Omega \rho \underline{u}\,\mathrm{d}\Omega + \int_\Omega \nabla \cdot \left(\rho \underline{\underline{uu}}\right)\,\mathrm{d}\Omega = \int_\Omega \rho \underline{g}\,\mathrm{d}\Omega + \int_\Omega \nabla \cdot \underline{\underline{\sigma}}\,\mathrm{d}\Omega. \tag{4.15}$$

For non-Newtonian fluids, the relation between the stress tensor and the velocity is defined by a set of partial differential equations and the problem is far more complicated. As in Chap. 4.1.1 this equation can be expressed in a coordinate-free vector form for infinitesimal small control volumes:

$$\frac{\partial}{\partial t}\left(\rho \underline{u}\right) + \nabla \cdot \left(\rho \underline{\underline{uu}}\right) = \nabla \cdot \underline{\underline{\sigma}} + \rho \underline{g}, \tag{4.16}$$

Using Eq. 4.13 and Eq. 4.14 this leads to

$$\frac{\partial}{\partial t}\left(\rho \underline{u}\right) + \nabla \cdot \left(\rho \underline{\underline{uu}}\right) = -\nabla p + \eta \nabla \cdot \left(\nabla \underline{u}\right) + \rho \underline{g} \tag{4.17}$$

4.1.3 Energy equation

For a full description of a compressible flow the enthalpy is necessary. Once again, Eq. 4.6 gives an equation of conservation

$$\frac{\partial}{\partial t}\int_\Omega \rho h \,\mathrm{d}\Omega + \int_\Omega \nabla\cdot\left(\rho h \underline{u}\right)\,\mathrm{d}\Omega = \int_\Omega Q_h \,\mathrm{d}\Omega + \int_\Omega D_h \,\mathrm{d}\Omega. \tag{4.18}$$

In this, ϕ was set to be the enthalpy h in the system and the additional source terms Q_h and D_h have to be found. The diffusive transport of energy is given by Fourier´s law of heat transfer and can be written as

$$q'' = k\nabla T \qquad \text{with:} \qquad k = \frac{\eta c_p}{\mathrm{Pr}}. \tag{4.19}$$

In this case k is the thermal diffusivity with the dynamic viscosity η, T the temperature, c_p the specific heat at constant pressure and Pr is the Prandtl number. In addition the surface forces, like the pressure, the normal and shear stresses perform mechanical work on the control volume and have to be taken into account. Thus, the conservation of energy is given by

$$\frac{\partial}{\partial t}\int_\Omega \rho h \,\mathrm{d}\Omega + \int_\Omega \nabla\cdot\left(\rho h \underline{u}\right)\,\mathrm{d}\Omega = \frac{\partial}{\partial t}\int_\Omega p \,\mathrm{d}\Omega + \int_\Omega \underline{u}\cdot\nabla p \,\mathrm{d}\Omega + \int_\Omega \nabla\cdot\left(\underline{\underline{\tau}}\cdot\underline{u}\right)\,\mathrm{d}\Omega + \int_\Omega k\nabla T \,\mathrm{d}\Omega, \tag{4.20}$$

which leads to

$$\frac{\partial \rho h}{\partial t} + \nabla\cdot\left(\rho \underline{u} h\right) = \frac{\partial p}{\partial t} + \underline{u}\cdot\nabla p + \nabla(k\nabla T) + \nabla\cdot\left(\underline{\underline{\tau}}\cdot\underline{u}\right). \tag{4.21}$$

$\underline{\underline{\tau}}$ is the viscous stress tensor $\underline{\underline{\tau}} = \underline{\underline{\sigma}} + p\mathbb{1}$ which results from friction stresses at the surfaces of the control volume. $\frac{\partial p}{\partial t} + \underline{u}\cdot\nabla p$ represents mechanical work done on the control volume by pressure. A detailed review on the Navier-Stokes equations is given by the book of Prandtl [57].

4.2 The Finite Volume Elements Method

Eq. system 4.8 can be solved with a FVE method. The basis of the FVE method is the solution of Eq. 4.7 within a control volume of a mesh. After, the principle of this discretisation is described for the simple case of a mesh consisting of cubic cells. There are several other possible shapes in OpenFOAM for the cells of the mesh [59], but the basic principle holds.

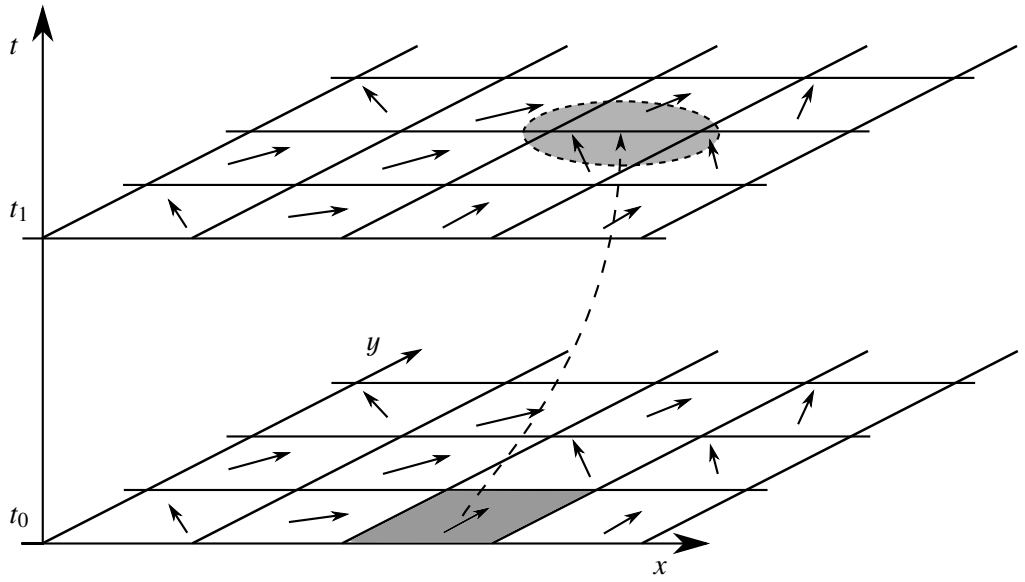

Figure 4.1: Behaviour of a fluid element in time and space. (Drawing inspired by Schwarze [60])

Fig. 4.1 shows the scheme of a two dimensional flow region at time t_0 and t_1. A fluid element at t_0 moves through the mesh from the initial control volume to another position at t_1 along the velocity vector drawn in the centre of the cells in Fig. 4.1. At time t_1, the fluid element has the new position in the mesh. This element transports all conservation values like the mass, motion and enthalpy from the position at the time t_0 to the position at t_1. This means the source terms for convective and diffusive flow F_ϕ and D_ϕ in Eq. 4.7 exist outside the limits of the control volume. Hence, the determination of this source terms is essential. The main advantage of the FVE method is, that it solves F_ϕ and D_ϕ at the boundaries of every cell in the mesh and is able to determine this sources beyond the boundaries.

For the determination of the fluid parameter, Eq. 4.7 is used:

$$\begin{aligned} & \frac{\partial}{\partial t}\int_\Omega \rho\phi\left(\underline{x},t\right)\,\mathrm{d}\Omega + \int_\Omega \nabla\cdot\left(\rho\phi\left(\underline{x},t\right)\underline{u}\right)\,\mathrm{d}\Omega = \int_\Omega Q_\phi\,\mathrm{d}\Omega + \int_\Omega D_\phi\,\mathrm{d}\Omega, \\ \Rightarrow\ & \frac{\partial}{\partial t}\int_\Omega \rho\phi\left(\underline{x},t\right)\,\mathrm{d}\Omega = \int_\Omega \left[D_\phi\ - \nabla\cdot\left(\rho\phi\left(\underline{x},t\right)\underline{u}\right) + Q_\phi\right]\,\mathrm{d}\Omega. \end{aligned} \tag{4.22}$$

With the Gauss- theorem this can be rewritten as

$$\frac{\partial}{\partial t}\int_\Omega \rho\phi\left(\underline{x},t\right)\,\mathrm{d}\Omega = \oint_S (\Gamma\nabla\phi)\cdot\underline{n}\,\mathrm{d}S\ - \oint_S \left(\rho\phi\left(\underline{x},t\right)\underline{u}\right)\cdot\underline{n}\,\mathrm{d}S\ + \int_\Omega Q_\phi\,\mathrm{d}\Omega. \tag{4.23}$$

Now there are 4 terms in Eq. 4.23 which describe the problem for each flow parameter in any control volume that is surrounded by the closed surface S. The left side is the behaviour of $\rho\phi$ in time, the first two terms on the right side the diffusive and convective flow of $\rho\phi$ through S and the last one is for any other sources for ϕ.

Before Eq. 4.23 can be calculated for a specific geometry, the computational fluid domain has to be discretised into a finite number of control volumes Ω. It constitutes a three-dimensional mesh and includes the information for the boundaries to the neighbouring cells. The centre of Ω is defined as the computational node and calculated as the centre of gravity of the volume on which the equation system is solved. This centre represents the mean value for the flow parameter in the control volume. The conservation property is given due to the fact that the surface integrals of the internal faces cancel out and only the surface integrals on the global boundaries remains, while the contributions of the volume integral add up to a global single term. More details about the necessary mesh for the calculation and its structures can be found in [61].

4.2.1 Time discretisation

The discretisation methods in time, used for CFD, are described by Schwarze [60] or Ferziger [61]. Herein, only a brief introduction in time discretisation is given since a steady state solver is used for the simulation of the different cooling stages for the dilution refrigerator. The time derivative term is usually discretised by means of a finite difference ratio. The simplest scheme is the Euler scheme

$$\frac{\partial\phi}{\partial t} \approx \frac{\phi_n - \phi_{n-1}}{\Delta t}. \tag{4.24}$$

The index n denotes the time step and Δt the duration of this time step itself. The Euler method is only a first order method. For a higher accuracy several CFD-codes uses the backward differencing scheme

$$\frac{\partial\phi}{\partial t} = \frac{3\phi_n - 4\phi_{n-1} + 4\phi_{n-2}}{2\Delta t}. \tag{4.25}$$

4.2.2 Space discretisation

After the creation of the mesh, Eq 4.23 has to be discretised. This section will explain the principle of discretisation for the finite volume method, following the description in the book of Versteeg [62]. The case of a steady state diffusion, as it is used for the heat transfer through the solid parts of the heat exchangers, is shown as an example. The process is governed by

$$\frac{\partial}{\partial x}\left(\Gamma\frac{\partial\Phi}{\partial x}\right) + \frac{\partial}{\partial y}\left(\Gamma\frac{\partial\Phi}{\partial y}\right) + \frac{\partial}{\partial z}\left(\Gamma\frac{\partial\Phi}{\partial z}\right) + Q_\Phi = 0, \tag{4.26}$$

where Γ is the diffusion coefficient and Q_Φ is a generic source term. Fig. 4.2 shows the cells of a three-dimensional mesh. After the mesh is divided into discrete control volumes, a nodal point is placed in the centre of each cell. It is common practice to set up the control volumes at the edges in such a way that the physical boundary conditions coincide with the boundary conditions of the control volumes. The usual convention of the CFD methods is shown in Fig. 4.2a for the one-dimensional case. A general nodal point is given by **P**, the neighbouring nodes are identified by **W** and **E**, as the nodes are in the west and east of **P**. The west side face is referenced by **w** and the east side control volume face by **e**. The distance between the nodes **W** and **P** and between the Nodes **P** and **E** are given by δx_{WP} and δx_{PE}.

Similarly, the distance between **w** and **P** and between **P** and **e** is given by δx_{wP} and δx_{Pe}, hence the control volume is given by $\Delta x = \delta x_{\mathrm{we}}$.

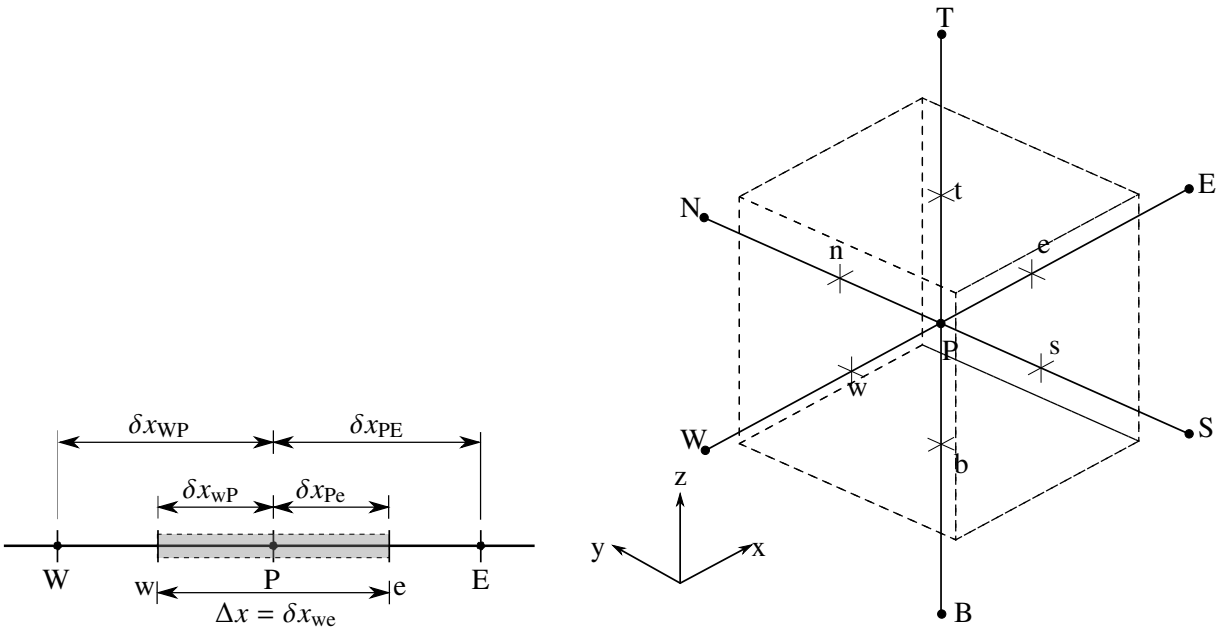

(a) 1D mesh (b) 3D mesh

Figure 4.2: Mesh in different dimensions for the discretisation in space

In the case of the three-dimensional grid given in Fig. 4.2b, four additional nodes for north (**N**), south (**S**), bottom (**B**) and top (**T**) are defined. This leads to a control volume given by $\Delta x = \delta x_{\mathrm{we}}, \Delta y = \delta y_{\mathrm{ns}}$ and $\Delta z = \delta z_{\mathrm{bt}}$.

The key step of the finite volume method is the integration of the governing equations over a control volume to yield a discretised equation at its nodal point **P**. For the three dimensional control volume, defined above, this leads to

$$\int_{\Delta V} \frac{\partial}{\partial x}\left(\Gamma \frac{\partial \Phi}{\partial x}\right) \mathrm{d}V + \int_{\Delta V} \frac{\partial}{\partial y}\left(\Gamma \frac{\partial \Phi}{\partial y}\right) \mathrm{d}V + \int_{\Delta V} \frac{\partial}{\partial z}\left(\Gamma \frac{\partial \Phi}{\partial z}\right) \mathrm{d}V + \int_{\Delta V} \bar{Q}_{\Phi}\, \mathrm{d}V = 0 \tag{4.27}$$

$$\left[\Gamma_{\mathrm{e}} A_{\mathrm{e}} \left(\frac{\partial \Phi}{\partial x}\right)_{\mathrm{e}} - \Gamma_{\mathrm{w}} A_{\mathrm{w}} \left(\frac{\partial \Phi}{\partial x}\right)_{\mathrm{w}}\right] + \left[\Gamma_{\mathrm{n}} A_{\mathrm{n}} \left(\frac{\partial \Phi}{\partial y}\right)_{\mathrm{n}} - \Gamma_{\mathrm{s}} A_{\mathrm{s}} \left(\frac{\partial \Phi}{\partial y}\right)_{\mathrm{s}}\right] + \left[\Gamma_{\mathrm{t}} A_{\mathrm{t}} \left(\frac{\partial \Phi}{\partial z}\right)_{\mathrm{t}} - \Gamma_{\mathrm{b}} A_{\mathrm{b}} \left(\frac{\partial \Phi}{\partial z}\right)_{\mathrm{b}}\right] + \bar{Q}_{\Phi} \Delta V = 0 \tag{4.28}$$

A_{i} is the cross-sectional area of the control volume face, ΔV the volume and $\bar{Q}_{\Phi}$ is the average source term over the control volume. Eq. 4.27 shows that the diffusive flux of Φ leaving one face, minus the diffusive flux entering through the counterpart face, is equal to the generation of Φ.

For the derivation of the discretised equations, the interface diffusion coefficient Γ and the gradient $\frac{\partial \Phi}{\partial x,\, y,\, z}$ for the different boundary faces are required. The values of the diffusion coefficients and Φ are

defined at the nodal points, whereas the gradients and hence fluxes at the control volume faces have to be calculated. A linear approximate distribution (central differencing) of the properties between the nodal points is used to do that. Thus, the diffusion coefficient can be written as:

$$\begin{aligned} \Gamma_{\mathrm{w,\,s,\,b}} &= \frac{\Gamma_{\mathrm{W,\,S,\,B}} + \Gamma_{\mathrm{P}}}{2} \\ \Gamma_{\mathrm{e,\,n,\,t}} &= \frac{\Gamma_{\mathrm{P}} + \Gamma_{\mathrm{E,\,N,\,T}}}{2} \end{aligned} \tag{4.29}$$

The diffusive fluxes through the faces are evaluated as:

$$\begin{aligned} \Gamma_{\mathrm{w}} A_{\mathrm{w}} \left(\frac{\partial \Phi}{\partial x}\right)_{\mathrm{w}} &= \Gamma_{\mathrm{w}} A_{\mathrm{w}} \left(\frac{\Phi_{\mathrm{P}} - \Phi_{\mathrm{W}}}{\delta x_{\mathrm{WP}}}\right) \\ \Gamma_{\mathrm{s}} A_{\mathrm{s}} \left(\frac{\partial \Phi}{\partial y}\right)_{\mathrm{s}} &= \Gamma_{\mathrm{s}} A_{\mathrm{s}} \left(\frac{\Phi_{\mathrm{P}} - \Phi_{\mathrm{S}}}{\delta y_{\mathrm{SP}}}\right) \\ \Gamma_{\mathrm{b}} A_{\mathrm{b}} \left(\frac{\partial \Phi}{\partial z}\right)_{\mathrm{b}} &= \Gamma_{\mathrm{b}} A_{\mathrm{b}} \left(\frac{\Phi_{\mathrm{P}} - \Phi_{\mathrm{B}}}{\delta z_{\mathrm{PB}}}\right) \\ \Gamma_{\mathrm{e}} A_{\mathrm{e}} \left(\frac{\partial \Phi}{\partial x}\right)_{\mathrm{e}} &= \Gamma_{\mathrm{e}} A_{\mathrm{e}} \left(\frac{\Phi_{\mathrm{E}} - \Phi_{\mathrm{P}}}{\delta_{\mathrm{PE}}}\right) \\ \Gamma_{\mathrm{n}} A_{\mathrm{n}} \left(\frac{\partial \Phi}{\partial y}\right)_{\mathrm{n}} &= \Gamma_{\mathrm{n}} A_{\mathrm{n}} \left(\frac{\Phi_{\mathrm{N}} - \Phi_{\mathrm{P}}}{\delta y_{\mathrm{PN}}}\right) \\ \Gamma_{\mathrm{t}} A_{\mathrm{t}} \left(\frac{\partial \Phi}{\partial z}\right)_{\mathrm{t}} &= \Gamma_{\mathrm{t}} A_{\mathrm{t}} \left(\frac{\Phi_{\mathrm{T}} - \Phi_{\mathrm{P}}}{\delta z_{\mathrm{TN}}}\right) \end{aligned} \tag{4.30}$$

For most cases, the source term Q_Φ is a function of the dependent variable, so the source term can be approximated by the linear form

$$\bar{Q}_\Phi \Delta V = Q_{\mathrm{u}} + Q_{\mathrm{p}} \Phi_{\mathrm{P}}. \tag{4.31}$$

Under the usage of 4.30 and 4.31, Eq. 4.28 is obtained

$$\begin{aligned} \left[\Gamma_{\mathrm{e}} A_{\mathrm{e}} \left(\frac{\Phi_{\mathrm{E}} - \Phi_{\mathrm{P}}}{\delta_{\mathrm{PE}}}\right) - \Gamma_{\mathrm{w}} A_{\mathrm{w}} \left(\frac{\Phi_{\mathrm{P}} - \Phi_{\mathrm{W}}}{\delta x_{\mathrm{WP}}}\right)\right] + \left[\Gamma_{\mathrm{n}} A_{\mathrm{n}} \left(\frac{\Phi_{\mathrm{N}} - \Phi_{\mathrm{P}}}{\delta y_{\mathrm{PN}}}\right) - \Gamma_{\mathrm{s}} A_{\mathrm{s}} \left(\frac{\Phi_{\mathrm{P}} - \Phi_{\mathrm{S}}}{\delta y_{\mathrm{SP}}}\right)\right] \\ + \left[\Gamma_{\mathrm{t}} A_{\mathrm{t}} \left(\frac{\Phi_{\mathrm{T}} - \Phi_{\mathrm{P}}}{\delta z_{\mathrm{TN}}}\right) - \Gamma_{\mathrm{b}} A_{\mathrm{b}} \left(\frac{\Phi_{\mathrm{P}} - \Phi_{\mathrm{B}}}{\delta z_{\mathrm{PB}}}\right)\right] + \left(Q_{\mathrm{u}} + Q_{\mathrm{p}} \Phi_{\mathrm{P}}\right) = 0. \end{aligned} \tag{4.32}$$

Identifying the coefficients of Φ_{i} in Eq. 4.31 as a_{i} and for Φ_{P} with a_{P}, the above equation can be written as

$$a_{\mathrm{P}} \Phi_{\mathrm{P}} = a_{\mathrm{W}} \Phi_{\mathrm{W}} + a_{\mathrm{E}} \Phi_{\mathrm{E}} + a_{\mathrm{S}} \Phi_{\mathrm{S}} + a_{\mathrm{N}} \Phi_{\mathrm{N}} + a_{\mathrm{B}} \Phi_{\mathrm{B}} + a_{\mathrm{T}} \Phi_{\mathrm{T}} + Q_{\mathrm{u}} = \sum_{\mathrm{i}} a_{\mathrm{i}} \Phi_{\mathrm{i}} + Q_{\mathrm{u}}, \tag{4.33}$$

with

$$a_\mathrm{P} = \sum_\mathrm{i} a_\mathrm{i} - Q_\mathrm{u} \tag{4.34}$$

for the coefficients around point P. Eq. 4.33 can always be reduced to two- or one-dimensional problems. A summary of the neighbour coefficients for diffusion problems is given in Tab. 4.2. The boundary conditions are incorporated by cutting the link to the boundary side and introducing the boundary side flux through additional source terms Q_u and Q_p. This linear discretisation scheme is used to calculate the heat transfer through the solid of the heat exchanger in the performed simulations. In this case Γ is given bei the thermal conductivity k and the parameter Φ is represented by the enthalpy h. The coefficients are given in Tab 4.3.

Table 4.2: General neighbour coefficients for a diffusive flow

	a_W	a_E	a_S	a_N	a_B	a_T
1D	$\frac{\Gamma_\mathrm{w}A_\mathrm{w}}{\delta_\mathrm{WP}}$	$\frac{\Gamma_\mathrm{e}A_\mathrm{e}}{\delta_\mathrm{PE}}$	-	-	-	-
2D	$\frac{\Gamma_\mathrm{w}A_\mathrm{w}}{\delta_\mathrm{WP}}$	$\frac{\Gamma_\mathrm{e}A_\mathrm{e}}{\delta_\mathrm{PE}}$	$\frac{\Gamma_\mathrm{s}A_\mathrm{s}}{\delta_\mathrm{SP}}$	$\frac{\Gamma_\mathrm{n}A_\mathrm{n}}{\delta_\mathrm{PN}}$	-	-
3D	$\frac{\Gamma_\mathrm{w}A_\mathrm{w}}{\delta_\mathrm{WP}}$	$\frac{\Gamma_\mathrm{e}A_\mathrm{e}}{\delta_\mathrm{PE}}$	$\frac{\Gamma_\mathrm{s}A_\mathrm{s}}{\delta_\mathrm{SP}}$	$\frac{\Gamma_\mathrm{n}A_\mathrm{n}}{\delta_\mathrm{PN}}$	$\frac{\Gamma_\mathrm{b}A_\mathrm{b}}{\delta_\mathrm{BP}}$	$\frac{\Gamma_\mathrm{t}A_\mathrm{t}}{\delta_\mathrm{PT}}$

Table 4.3: Neighbour coefficients for a heat flow through a solid

	a_W	a_E	a_S	a_N	a_B	a_T
1D	$\frac{k_\mathrm{w}A_\mathrm{w}}{\delta_\mathrm{WP}}$	$\frac{k_\mathrm{e}A_\mathrm{e}}{\delta_\mathrm{PE}}$	-	-	-	-
2D	$\frac{k_\mathrm{w}A_\mathrm{w}}{\delta_\mathrm{WP}}$	$\frac{k_\mathrm{e}A_\mathrm{e}}{\delta_\mathrm{PE}}$	$\frac{k_\mathrm{s}A_\mathrm{s}}{\delta_\mathrm{SP}}$	$\frac{k_\mathrm{n}A_\mathrm{n}}{\delta_\mathrm{PN}}$	-	-
3D	$\frac{k_\mathrm{w}A_\mathrm{w}}{\delta_\mathrm{WP}}$	$\frac{k_\mathrm{e}A_\mathrm{e}}{\delta_\mathrm{PE}}$	$\frac{k_\mathrm{s}A_\mathrm{s}}{\delta_\mathrm{SP}}$	$\frac{k_\mathrm{n}A_\mathrm{n}}{\delta_\mathrm{PN}}$	$\frac{k_\mathrm{b}A_\mathrm{b}}{\delta_\mathrm{BP}}$	$\frac{k_\mathrm{t}A_\mathrm{t}}{\delta_\mathrm{PT}}$

In problems where fluid flow plays a significant role, the effects of convection has to taken into account. The steady convection-diffusion equation can be derived from the transport equation Eq. 4.7 for a general transport property ϕ by

$$\nabla \cdot \left(\rho \underline{u} \phi\right) = \nabla \cdot (\Gamma \nabla \phi) + Q_\phi. \tag{4.35}$$

After the integration over a control volume this gives similar to Eq. 4.23

$$\oint_S \left(\rho\phi\left(\underline{x}, t\right)\underline{u}\right) \cdot \underline{n}\,\mathrm{d}S = \oint_S (\Gamma\nabla\phi) \cdot \underline{n}\,\mathrm{d}S + \int_\Omega Q_\phi\,\mathrm{d}\Omega. \tag{4.36}$$

This equation represents the flux balance in a control volume. The left hand side gives the net convective flux and the right hand side contains the net diffusive flux and the generation of destruction of the property ϕ within the control volume.

Due to the fact that the diffusion process affects the distribution of a transported quantity along its gradients in all directions, whereas convection spreads influence only in the flow direction, it is possible that higher order discretisation schemes have to be used. In the case of low mass flows and low Reynolds numbers the central differencing method still gives good results.

Then the discretisation leads to a very similar structure like in Eq. 4.33

$$a_\mathrm{P}\Phi_\mathrm{P} = a_\mathrm{W}\Phi_\mathrm{W} + a_\mathrm{E}\Phi_\mathrm{E} + a_\mathrm{S}\Phi_\mathrm{S} + a_\mathrm{N}\Phi_\mathrm{N} + a_\mathrm{B}\Phi_\mathrm{B} + a_\mathrm{T}\Phi_\mathrm{T} \tag{4.37}$$

where the coefficients are given in Tab. 4.4.

Table 4.4: general neighbour coefficients for a convective-diffusive flow for a fluid

a_{W}	a_{E}	a_{S}	a_{N}	a_{B}	a_{T}	a_{P}
$D_{\mathrm{w}} + \frac{F_{\mathrm{w}}}{2}$	$D_{\mathrm{e}} + \frac{F_{\mathrm{e}}}{2}$	$D_{\mathrm{s}} + \frac{F_{\mathrm{s}}}{2}$	$D_{\mathrm{n}} + \frac{F_{\mathrm{n}}}{2}$	$D_{\mathrm{b}} + \frac{F_{\mathrm{b}}}{2}$	$D_{\mathrm{t}} + \frac{F_{\mathrm{t}}}{2}$	$\sum_i a_i + (F_{\mathrm{e}} - F_{\mathrm{w}}) + (F_{\mathrm{n}} - F_{\mathrm{s}}) + (F_{\mathrm{t}} - F_{\mathrm{b}})$

Here the following definitions were used

$$F_{\mathrm{w,\,e}} = (\rho u)_{\mathrm{w,\,e}}\,, \qquad F_{\mathrm{s,\,n}} = (\rho v)_{\mathrm{s,\,n}}\,, \qquad F_{\mathrm{b,\,t}} = (\rho w)_{\mathrm{b,\,t}}\,, \tag{4.38}$$

$$D_{\mathrm{w,\,s,\,b}} = \frac{\Gamma_{\mathrm{w,\,s,\,b}}}{\delta x_{\mathrm{W,\,S,\,B\,P}}}, \qquad D_{\mathrm{w,\,s,\,b}} = \frac{\Gamma_{\mathrm{w,\,s,\,b}}}{\delta x_{\mathrm{W,\,S,\,B\,P}}}. \tag{4.39}$$

For other discretisation schemes like the upwind differencing scheme or the hybrid scheme (central and upwind combined) the equations have the same structure like Eq. 4.33 or 4.37. The main difference is that the coefficients contains additional terms to account for convection as it is shown in the book of Versteeg and Malalasekera [62].

4.3 CFD Modelling

The computational code used for the simulations is **OpenFOAM 2.4.0** [58]. It includes various types of solvers for different fluids e.g. compressible, incompressible, multi-phase, heat transfer cases. The OpenFOAM software contains tools for pre-processing and the solver tools. Useful features in the pre-processing tools are for example the meshing tools *blockMesh* and *snappyHexMesh* for generating the computational mesh. In the solving procedure of OpenFOAM there are two main parts:

- The *executable applications* which are referred to as solvers and utilities. The solvers are algorithms for solving systems of differential equations with the finite volume method
- The *case* is an entity which specifies the solver to be used, the geometry and other problem specific properties.

A full description of the tools provided by OpenFoam is given in [63].

4.3.1 Equations Used by OpenFOAM

The solver *chtMultiRegionSimpleFoam* is a steady state solver for conjugate heat transfer between a solid and a fluid region, including steady-state turbulent flow of compressible fluids.

Governing equations in fluid regions

The solver uses the continuity equation and the Navier-Stokes equations for compressible flow in vector forms as mentioned before

$$\frac{\partial \rho}{\partial t} + \nabla \cdot \left(\rho \underline{u}\right) = 0 \tag{4.40}$$

$$\frac{\partial}{\partial t}\left(\rho \underline{u}\right) + \nabla \cdot \left(\rho \underline{u}\underline{u}\right) = -\nabla p + \eta \nabla \cdot \left(\nabla \underline{u}\right) + \rho \underline{g} \tag{4.41}$$

where $\underline{u}$ is the velocity vector, p the static pressure, $\underline{g}$ the gravitational acceleration and η is the dynamic viscosity. The energy equation used by OpenFOAM can be written as

$$\frac{\partial (\rho E)}{\partial t} + \nabla \cdot \left(\rho \underline{u} E\right) = \nabla \cdot (k \nabla e) - \nabla \cdot \left[\underline{u}\left(p - \rho \underline{g}\right)\right] + Q_{\text{add}}. \tag{4.42}$$

k is the thermal diffusivity, Q_{add} is a thermal source term for additional heat sources, e the specific internal energy and E the total specific energy of the fluid defined as $E = e + \frac{u^2}{2}$. In this case the energy equation was defined with the inner Energy instead of the enthalpy as in Chap. 4.1.3. Both equations can be used by the solver but due to a better stability of the simulation Eq. 4.42 was used. Due to the steady state problem, the derivatives in time vanished.

Governing equations in solid regions

For the calculation of the heat transfer through the solid regions

$$\frac{\partial (\rho h)}{\partial t} = \nabla \cdot (k \nabla h) + Q_{\text{add}} \tag{4.43}$$

is used and h is the enthalpy. In the case of a steady state problem this reduces to

$$-\nabla \cdot (k \nabla h) = Q_{\text{add}}. \tag{4.44}$$

Conjugate Heat Transfer

The fluid and the solid domain are simulated simultaneously for the conjugate heat transfer. The constant temperature boundary condition is given for the outside surfaces of the solid regions in the model. In order to provide the boundary conditions for the fluid governing equations, on the interface between solid and fluid region a no-slip wall boundary condition is assumed.

For the used solver, the domain is divided in sub-meshes for each fluid and solid region. First the Navier-Stokes equations and the energy equation in the fluid regions are solved. Afterwards, the heat transfer equation in the solid regions is solved. The coupling between the different sub-meshes is achieved by exchanging information at the fluid/solid interfaces to ensure the continuity of temperature and the conservation of energy [64].

When the energy equation is solved in the fluid region, a temperature at the interface has to be specified. The temperature T_{w} at the interface can be calculated as follows:

$$T_{\text{w}} = \frac{\frac{k_{\text{s}}}{\delta x_{\text{s}}} T_{\text{s}}}{\frac{k_{\text{f}}}{\delta x_{\text{f}}} + \frac{k_{\text{s}}}{\delta x_{\text{s}}}} + (1-k)\left(T_{\text{f}} + \frac{\nabla T_{\text{ref}}}{\delta x_{\text{f}}}\right) = \frac{\frac{k_{\text{f}}}{\delta x_{\text{f}}} T_{\text{f}} + \frac{k_{\text{s}}}{\delta x_{\text{s}}} T_{\text{s}}}{\frac{k_{\text{f}}}{\delta x_{\text{f}}} + \frac{k_{\text{s}}}{\delta x_{\text{s}}}}, \tag{4.45}$$

where T_{f} and T_{s} are the temperatures from the neighbouring fluid and solid regions, k_{f} and k_{s} are the heat conductivities of the fluid and solid regions and T_{ref} is a reference temperature. By introducing the interpolation coefficient k as

$$k = \frac{\frac{k_{\text{s}}}{\delta x_{\text{s}}}}{\frac{k_{\text{f}}}{\delta x_{\text{f}}} + \frac{k_{\text{s}}}{\delta x_{\text{s}}}}, \tag{4.46}$$

where $\delta x_{\text{f, s}}$ are the distances between the cell centers and the interface. The temperature gradient at the interface can be calculated by the following equation

$$\nabla T_{\text{f}}^{\text{I}} = k \frac{T_{\text{s}} - T_{\text{f}}}{\delta x_{\text{f}}} + (1-k) \nabla T_{\text{ref}} = \frac{\frac{k_{\text{s}}}{\delta x_{\text{s}}}}{\frac{k_{\text{f}}}{\delta x_{\text{f}}} + \frac{k_{\text{s}}}{\delta x_{\text{s}}}} \frac{T_{\text{s}} - T_{\text{f}}}{\delta x_{\text{f}}}. \tag{4.47}$$

For the solid side of the interface a similar gradient relation exists. To ensure the energy conservation near the interface, the following additional condition is required

$$k_{\text{s}} T_{\text{s}}^{\text{I}} = k_{\text{f}} T_{\text{f}}^{\text{I}}. \tag{4.48}$$

4.3.2 The SIMPLE Algorithm

chtMultiRegionSimpleFoam is a compressible solver for steady state heat transfer. It's called *Simple* due to the **S**emi **I**mplicit **P**ressure **L**inked **E**quation algorithm which is used to solve the equation system. Fig. 4.3 shows a workflow scheme of this algorithm. Here p is the pressure, u, v, w are the vector components of the velocity and T is the temperature.

If an implicit method is used in the time domain, the discretised momentum equations at the new time step are non-linear. Because of the coupling of this differential equations, the equation system resulting from discretisation can not be solved directly.

The momentum equations are usually solved sequentially for each component. The pressure used in each iteration is obtained from the previous time step and therefore the computed velocities do not necessarily satisfy the continuity equation. In order to fullfill the continuity equation, the pressure field has to be modified, which can be done by solving the Poisson equation for the pressure.

After solving the equation and the correction of the pressure field, the velocity field is recalculated at the next iteration step. This new velocity field satisfies the continuity equation, but velocity and pressure field satisfies not necessary the momentum equations. Therefore, the procedure is iterated until a velocity field is found that satisfies both the momentum and continuity equation.

Methods of this kind, which first construct velocity fields that do not satisfy the continuity equation, are known as projection methods. The SIMPLE algorithm is such a method. Here p is the pressure, u, v, w are the vector components of the velocity and T is the temperature.

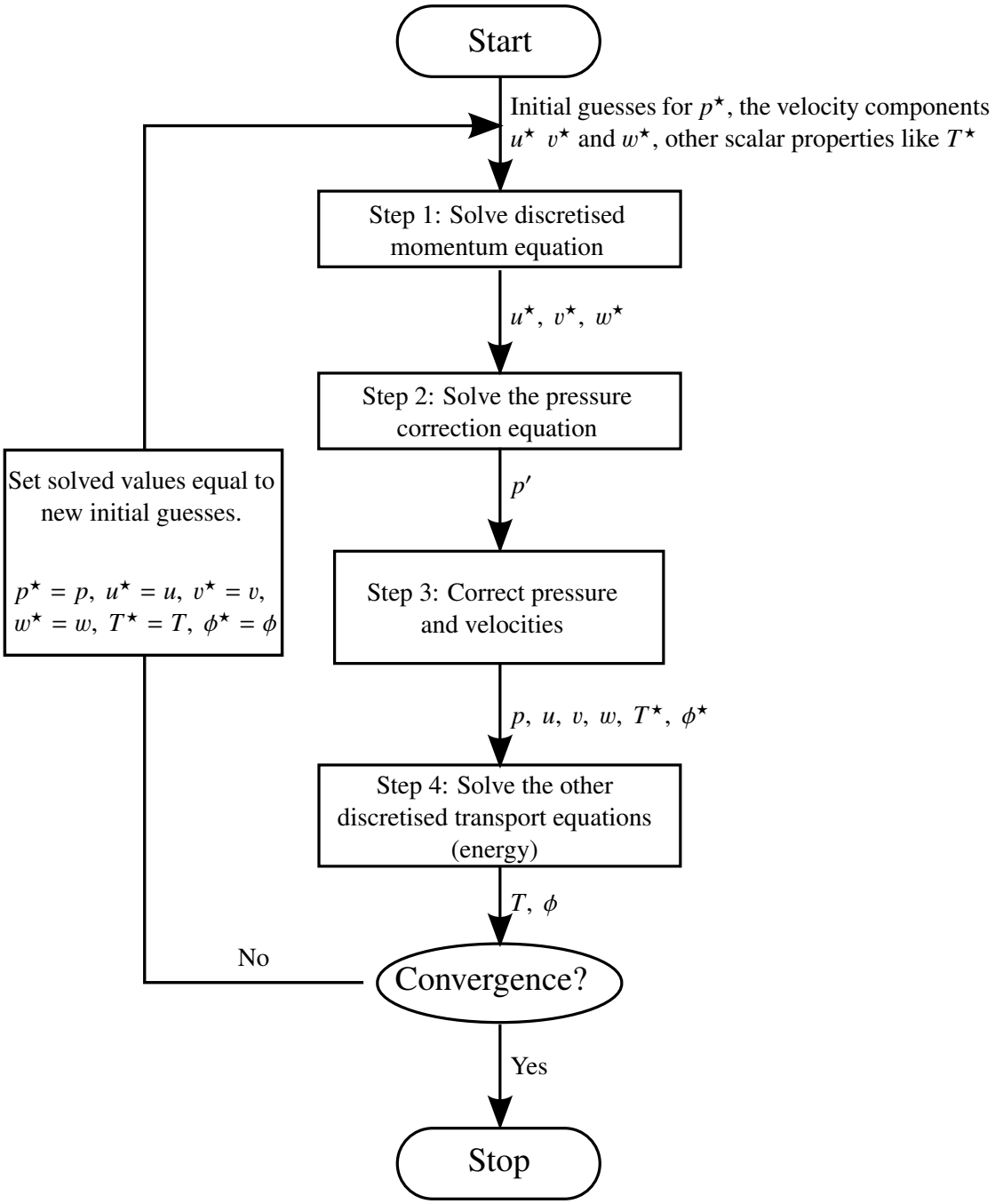

Figure 4.3: Scheme of the SIMPLE algorithm

Chapter 5

The 4π-Continuous Polarised Target

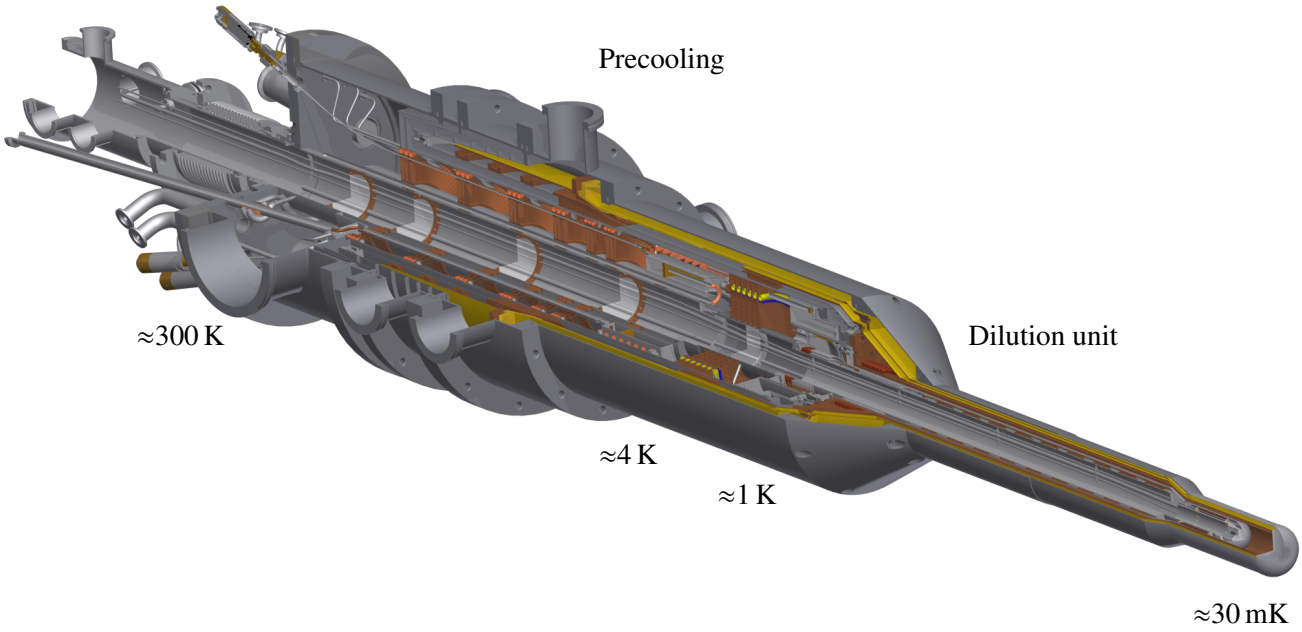

Figure 5.1: The continuous mode dilution refrigerator

Figure 5.1 shows the design of the new 4π continuous polarised target. It consists of two main components: the dilution and the precooling unit. In designing the refrigerator, it is important to consider the special demands of a polarised target instead of other applications for dilution refrigerators. Different to the dilution refrigerator described by Bradtke [13], the requirements for the two operational modes, as mentioned in Chap 2.3, are:

- **Continuous/polarisation mode**: $T = 200\,\mathrm{mK}$ and $\dot{Q} = 100\,\mathrm{mW}$
- **Frozen spin mode**: $T_{\mathrm{min}} = 30\,\mathrm{mK}$ and $\dot{Q} = 200\,\mu\mathrm{W}$
- Support of an internal polarisation magnet with a current of 90 A
- Maximum diameter of the target region of ⌀94 mm
- A target temperature below 160 K during the insert procedure

In any case, the minimum temperature attainable is limited by the heat leak to the mixing chamber. Thus, all imaginable sources have to be taken into account which is done in Chap. 5.1. This heat leak can not be avoided, due to the refrigerator geometry needed for the high angle acceptance of the experiment and the heating by the beam itself.

The precooling stages are designed to provide a large refrigeration power for cavity temperatures of $30\,\mathrm{mK} \leq T \leq 200\,\mathrm{mK}$ and a ^{3}He-^{4}He mixture flow rate of $1\,\mathrm{mmol\,s^{-1}} \leq \dot{n} \leq 20\,\mathrm{mmol\,s^{-1}}$. Thus, the precooling consists of 4 heat exchangers and two heat sinks, called separator and evaporator. Due to the high ^{3}He-^{4}He mixture circulation rate, the heat exchangers are optimised for a huge surface area. In addition, the incoming helium is cooled by the ^{3}He-^{4}He back-stream and liquid ^{4}He supported from the separator. A detailed description can be found in Chap. 5.2. The dilution unit, as described in Chap. 5.3, consists of a still, a copper sintered heat exchanger and a mixing chamber. In addition, a new design to cool the internal superconducting coils was implemented and, due to use of an internal polarisation magnet (see Chap. 5.4), the continuous mode for longitudinal polarisation is possible.

The refrigerator has to work for several weeks with the option to change the target material without heating up the refrigerator and to preserve a target material temperature of $\leq 160\,\mathrm{K}$ during the procedure. Therefore, an insert system as described in Chap 5.5 is necessary. However, the development of the 4π-continuous-mode refrigerator was determined not only by the cooling characteristics, but also under mechanical characteristics given by the CB detector.

5.1 Thermal Insulation

As Eq. 3.13 shows, the available cooling power at temperatures below 100 mK does not exceed 20 mW for the maximum flow-rate of $20\,\mathrm{mmol\,s^{-1}}$. Due to this, it is necessary to create a good thermal insulation of the refrigerator and different sources of heat leaks have to be taken into account:

- Thermal radiation
- Gaseous heat conductivity
- Heat transfer through mechanical supply
- Mechanical vibrations
- Joule heating

All of these heat sources are discussed in the next sections. Any heat increases the minimal temperature in the mixing chamber and reduces the supported cooling power for the target material. Thus, all of these influences have to be minimised for a good performance of the refrigerator.

5.1.1 Heat transfer through the radiation shielding

The Stefan-Boltzmann equation describes the radiant power of an area A_2 with a temperature T_2, which is totally enclosed by a surface area A_1 of the temperature T_1:

$$\dot{Q} = \sigma \cdot A_1 \cdot \left(T_2^4 - T_1^4\right) \frac{\epsilon_1 \epsilon_2}{\epsilon_2 + \left(\frac{A_1}{A_2}\right)(1-\epsilon_2)\,\epsilon_1} \tag{5.1}$$

The coefficients $\epsilon_{1,\,2}$ represent the values of emissivity of the corresponding materials. For this relation, it is assumed that the emissivity of a specific material equals the absorptivity. It has to be taken into account that ϵ is frequency dependent. At temperatures below 300 K, the distribution of the radiant power has its maximum in the far-infrared range, due to Wien's displacement law. Thus, an average value of the emissivity for the far-infrared range can be assumed.

The idea based on Eq. 5.1 is to use radiation shields of low emissivity, surrounding the refrigerator and decrease the temperature of each one. For this refrigerator, an inner and outer heat shield is used. They are anchored to two heat exchangers outside the refrigerator himself to a temperature of:

- **Outer heat shield**: $T \approx 20\,\mathrm{K}$
- **Inner heat shield**: $T \approx 2.5\,\mathrm{K}$

In difference to the refrigerator for the GDH experiment described by Bradtke [13], the cooling of the internal magnet and the heat shields is independent of the heat exchangers of the precooling unit. The separator (or evaporator) supports an independent cooling system which is used to cool the internal magnet, the heat shields and the leads of the internal magnet. In Fig. 5.2 the principle of this cooling system is shown. Liquid ^{4}He from the heat sinks of the precooling unit is used to cool down the magnet and afterwards to cool the heat radiation shields. Thus, the whole system is located in the isolation vacuum and has no direct contact to the inner parts of the refrigerator.

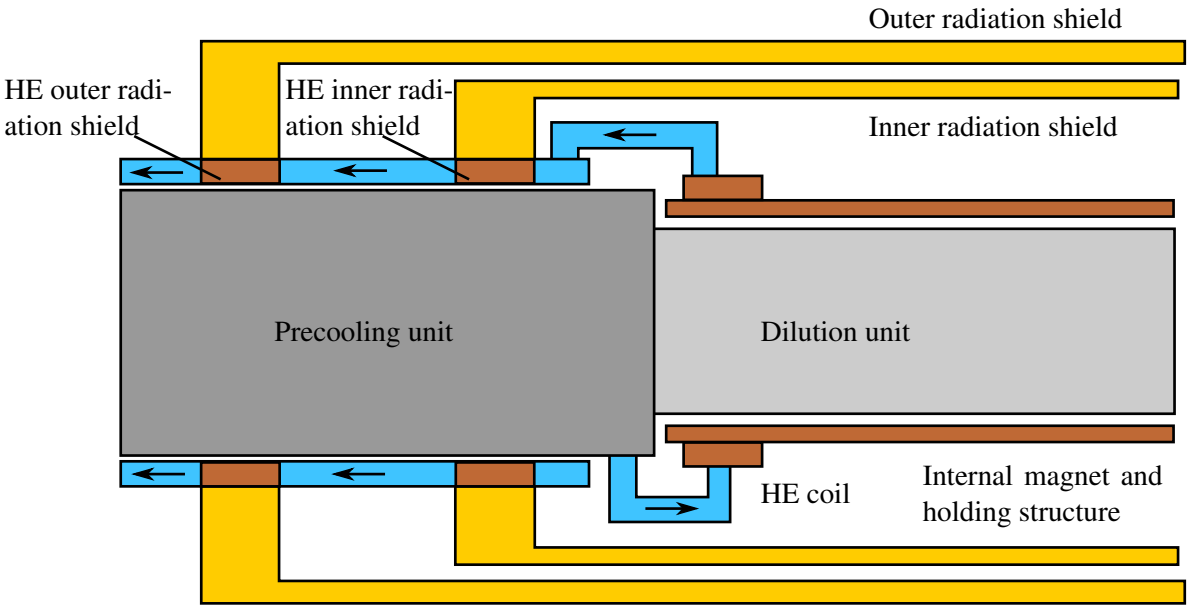

Figure 5.2: Block scheme for the cooling of the magnet and the radiation shields. The cooling system for the radiation heat shields and the magnet surrounds the inner parts of the refrigerator and is located in the vacuum shell.

Therefore, the temperature of the heat shields is independent of the ^{3}He-^{4}He circulation rate. In addition, this cooling system surrounds the precooling unit and reduces also the radiation heat to the inner parts of the refrigerator. The heat shields are made of oxygen free copper for maximal thermal conductance. This provides a quick removal of the heat load. Only the front parts of small surface area and

low heat load consists of aluminium to lower the detection threshold for the outgoing particles. The emissivity of the heat shield is decreased by a gold plating of 2 µm. Also, this prevents the heat shields from oxidation which would increase the emissivity over time.

The calculation of the temperature distribution is similiar to the calculation by Bradtke [13]. The heat shields were discretised by infinitesimal slices with the length Δx. Then it can be assumed that the radiative heat load on a slice is concentrated at its end and that the slice has to conduct the energy

$$P_{\mathrm{i}} = P_{\mathrm{i}-1} + \dot{Q}_{\mathrm{R,\,i}}. \tag{5.2}$$

The thermal conduction along a tube of the cross section A and a thermal conductivity $k\,(T)$ is given by the Fourier law

$$P_{\mathrm{i}} = A \cdot k\,(T)\,\frac{T_{\mathrm{i}} - T_{\mathrm{i}-1}}{\Delta x} \tag{5.3}$$

These equations can be used to calculate the temperature distribution of the heat shields with an iterative procedure. In Fig. 5.3 the calculated and measured temperature profile is shown.

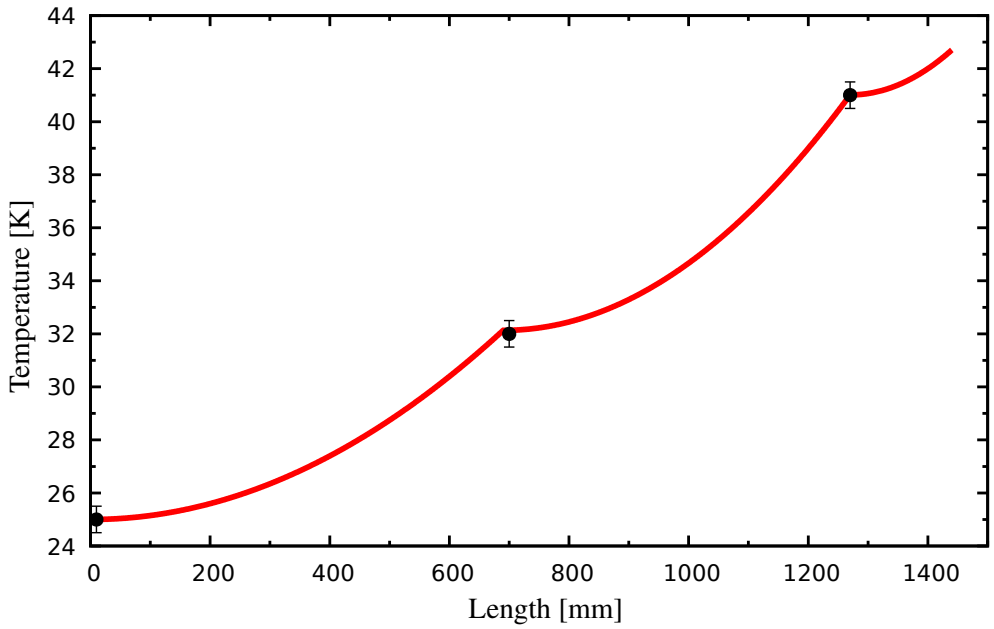

Figure 5.3: Temperature distribution on the outer heat shield

The temperature distribution in Fig. 5.3 leads to a total radiative heat load of about 13 W. Once the temperature profile of the outer heat shield is known, the radiative heat transfer of the inner shield can be calculated and then the heat load of the internal polarisation coil and the mixing chamber itself. The radiative heat load of the different shielding parts is given in App. A.3. The heat load of the cryogenic components ($\sim$ 3 mW) is small compared to the cooling power of the precooling unit. In addition, this is the heat load to the cooling components of the heat shields and the polarising magnet, which surrounds the inner refrigerator parts. Thus, the influence of radiative heat to the precooling is negligibly.

The mixing chamber is surrounded by the internal holding coil, which operates at a temperature of 1 K. To minimise the radiative heat, a radiation foil is attached to its downstream end. Also in the beam tube 5 radiative foils of decreasing temperature prevent radiative heat from the upstream side. Since the last foil is attached to the still, it also operates at a temperature of 1 K. Therefore, the total radiative heat load to the mixing chamber is evaluated to be 41 pW.

5.1.2 Heat transfer by gaseous conduction

An additional heat source, which has to be taken into account, is the heat transfer by gaseous conduction. Gas molecules placed between two bodies of different temperatures give rise to an energy flow from the hotter to the colder surface by collisions. In the range of turbulent flow the thermal conductivity is independent of the pressure because the distance between the surfaces exceeds the mean free path λ. In the case of the vacuum shell and the beam tube, the pressure is lowered such that $\lambda \gg d$. Then, the molecule conduction is the most important source for heat transfer by gaseous conduction. Now, the thermal heat transfer between two nearly parallel surfaces of an area A can be expressed by

$$\dot{Q}_{\text{gas}} = A \cdot a_0 \cdot \frac{c_p + c_V}{\sqrt{c_p - c_V}} \sqrt{\frac{1}{8\pi MT}} \cdot (T_2 - T_1) \cdot p \text{ [65].} \tag{5.4}$$

M is the molecular weight and T the temperature of the gas, whereas $c_{p,\,V}$ are the corresponding specific heat coefficients. The thermo molecular pressure effect based on thermal transpiration leads to a fixed pressure and temperature condition $p = \text{const} \cdot T^2$ [66]. The accommodation coefficient a_0 describes the efficiency of heat transfer between the walls and the gas molecules. White [67] gives $a_0 \geq 0.5$ for helium gas at the conditions of the isolation vacuum.

Eq. 5.4 shows that the heat transfer is largest for mono-atomic gas with low molecular weight. Unfortunately, the compression coefficient of turbo molecular pumps depends on $K = \exp\left(\sqrt{M}\right)$ [68]. The molecular weight and in this way the residual gas molecules are dominated by hydrogen, but in cryogenic apparatus, the system is cryo-pumped and below 10 K the atmosphere is nearly pure helium. Thus, Eq. 5.4 reads

$$\dot{Q}_{\text{gas}} = A \cdot a_0 \cdot 2.12 \frac{m}{s \cdot K} \cdot (T_2 - T_1) \cdot p. \tag{5.5}$$

In order to minimise gaseous heat transfer the dilution refrigerator is surrounded by a vacuum shell. The pressure of the cold refrigerator is reduced to $\leq 1 \times 10^{-5}$ mbar. The heat shields and the internal polarisation magnet are also located in the isolation vacuum. This prevents the gas molecules from travelling from the room temperature side to the cold wall of the refrigerator directly.

In comparison to the thermal radiation, the heat load by conduction on the heat shields and the enclosure of the cryogenic components is negligible, due to the fact that the heat load by gaseous conduction is 10^1 to 10^2 orders smaller than for the radiative heat transfer. For the mixing chamber it is different. In this case and in the case of the internal super conducting magnet, the heat load by gas conduction is the dominant process and around 1 µW. In addition, the mixing chamber is in contact with the isolation vacuum of the beam tube. The insert of the beam tube, where the target is located, is sealed with an cold indium seal against the mixing chamber. This means that the pressure of the isolation vacuum in the beam pipe depends on this tightening and whether super leaks can be avoided at this seal.

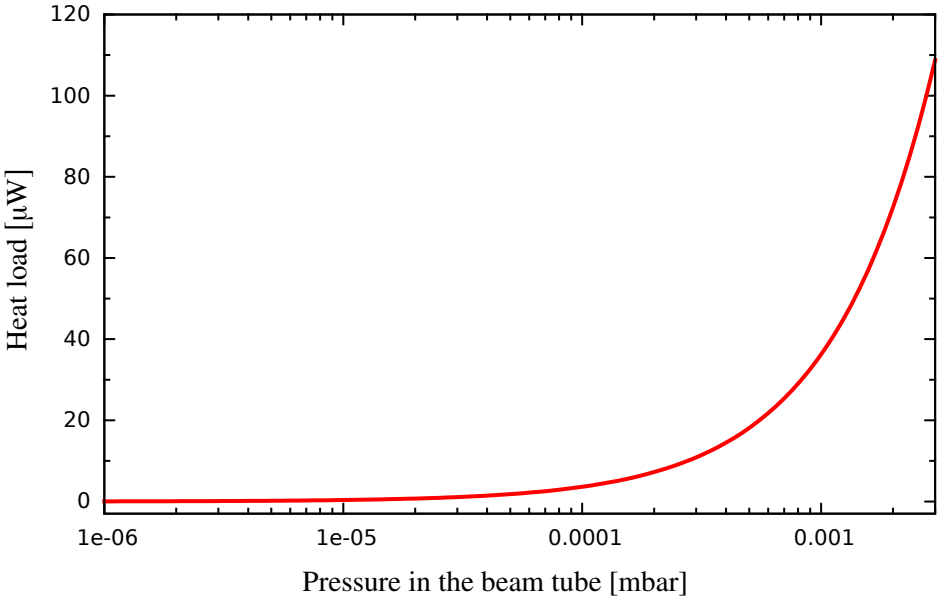

Figure 5.4: Additional heat load by gaseous heat transfer through the beam tube

Fig. 5.4 shows the heat load on the mixing chamber through the beam tube at different pressures. It is obvious that for a good performance of the refrigerator the pressure of the beam tube has to be as small as possible.

During the test measurements described in Chap. 6, a beam tube vacuum of $\approx 5 \times 10^{-5}$ mbar could be reached with liquid ^{4}He in the dilution unit. Without liquid ^{4}He in the dilution unit, a pressure of $\approx 2.4 \times 10^{-7}$ mbar was reached. This shows that the indium ring did not seal the beam tube against the mixing chamber perfectly, but good enough to reach a pressure region where the heat load to the mixing chamber is in an acceptable region. In App. A.3 the calculated heat loads to the different parts of the refrigerator are summarised.

5.1.3 Heat conduction by mechanical supply and vibrations

An additional heat source, which has to be taken into account, is the heat conduction along the mechanical structure of the refrigerator and heat generation by mechanical vibrations. Remembering Eq. 5.3, the axial heat conduction in an isotropic solid of length l and cross-section A can be described by

$$\dot{Q}_{\text{structure}} = \frac{A}{l} \int_{T_1}^{T_2} \kappa(T)\, \mathrm{d}T. \tag{5.6}$$

In this equation the intrinsic thermal conductivity is of utmost importance. Electrons can carry the heat in a solid and, due to their mobility, this leads to $\kappa \propto T$. Also, phonons can translate the heat through a solid which gives a dependence of $\kappa \propto T^2$. Since at low temperatures the number of phonons is small, electron conduction represents the dominating process in pure metals. Then, the thermal conductivity

can be expressed by the Wiedemann-Franz law [69]

$$\kappa(T) = \frac{\sigma}{3}\left(\frac{\pi k}{e}\right)^2 = \sigma \cdot 25\,\mathrm{nW\,\Omega\,K^{-1}} \cdot T. \tag{5.7}$$

Thus, metals like oxygen free high conductivity copper, which provide highest conductivity up to $1300\,\mathrm{W/K^2/m} \cdot T$, are used for the heat exchanger components for optimised heat exchange. Stainless steel, with a much lower conductivity [70], is used for the mechanical structure to reduce the heat conduction. The thermal conductivity of stainless steel is about 10^4 times less compared to copper, due to the scattering of the electrons by impurity atoms in the structure. Thus, stainless steel is also used to isolate the different components of the refrigerator from each other. In addition, thin walled tubes are used to reduce the cross section along the axis of heat conduction, which is a common technique in cryophysics reffered to Hands[71].

The mixing chamber is located at the end of a tube, which forms a part of the heat exchanger of the dilution unit. Thus, the heat conductivity along this structure can be neglected. The main heat load, through heat conduction along the mechanical structure to the mixing chamber, comes from the target insert, the microwave- and the NMR-guide. To reduce the conducted heat, all of these parts are build from thin walled tubes. The NMR guide used for this refrigerator is UT-T-85-B-B, which is a coaxial conductor of beryllium copper alloy isolated by Teflon. Beryllium copper is a metal which has a high electrical conductivity, but a low thermal conductivity. In addition, several heat sinks are used to reduce the axial heat conductivity, the coldest one thermally anchored to the still at a temperature of 700 mK and a distance of arround 1 m from the mixing chamber. Following, the calculations of Klostermann [72], the heat conduction along the NMR guide, with length l, is given by

$$\dot{Q}_{\mathrm{NMR}} = \frac{12.2\,\mu\mathrm{W\,cm}}{l}\left(T_2^{2.25} - T_1^{2.25}\right). \tag{5.8}$$

For a temperature of 30 mK at the mixing chamber, this leads to a heat load of 220 nW. For temperatures below 1 K, the thermal conductivity for stainless steel can be written as

$$\kappa(T) = 0.15\,\mathrm{W\,K^{-1}\,m^{-2}} \cdot T - 4.8\,\mathrm{W\,K^{-1}\,m^{-1}} \cdot T. \tag{5.9}$$

Using Eq. 5.6, the resulting heat load is about 7.2 µW. At temperatures in the milli-kelvin region, the heat generation by mechanical vibrations also has to be taken into account. Especially in the case of a horizontal dilution refrigerator, like this continuous mode refrigerator, this effect is increased. The refrigerator is more than 2 m long and the distance between the mixing chamber and the base of the refrigerator is of the same order. This leads to a sensitive setup for vibrations of any sources. The main source are vibrations from the pumping system. Thus the root pumps, which are operating at a frequency of 50 Hz resulting in a typically building motion frequency of $\approx 2{-}4$ Hz [73], are uncoupled by attaching them with rubber pads to their mechanical supply. In addition, the pumping leads between root pumps and refrigerator are uncoupled with flexible metal bellows. Following Lounasmaa [74], mechanical vibrations easily cause a heat load of $\approx$ 100 nW and in the case of strong vibrations and poor damping this heat load goes up to several micro-watts. In this system, the heat load due to vibrations should be smaller than 100 nW.

5.1.4 Joule heating

For thermometry, resistance thermometers are located at the mixing chamber, the heat sinks, the heat exchangers and all other important parts of the refrigerator. The electric currents of these and the internal polarization magnet cause a heat load, which can be calculated by

$$\dot{Q}_{\text{electric}} = I^2 R = \frac{U^2}{R}. \tag{5.10}$$

I is the current, R the resistance and U the voltage used for the measurement. The resistance thermometers are measured with 4-wire AC bridges whose excitation is adapted to the particular temperature region. To reduce the heat conduction along the measurement wire, a special quad twisted wire is used. Also, the AC bridges measures only one resistance at one time to reduce the joule heating. This leads to a heat load of less than 10 pW from thermometry.

5.1.5 Heat load on the mixing chamber

The above sections show that the heat transfer from the room temperature surroundings on the refrigerator is dominated by thermal conduction along the mechanical supply and by thermal radiation. To reduce the heat load on the mixing chamber, it is important to have a pressure as low as possible in the beam pipe to minimise the effect of gaseous heat conduction. The heat load from mechanical vibration and Joule heating can be neglected since they are in the order of 100 nW. Tab. 5.1 summarises the heat load of the different sources to the mixing chamber.

Table 5.1: Heat load on the mixing chamber

	P
radiative heat transport	41 pW
gaseous conduction without beampipe	0.4 μW
gaseous conduction through the beam pipe	≤ 31.5 μW
conduction by solids	7.4 μW
mechanical vibrations	< 100 nW
Joule heating	< 1 pW

5.2 The Precooling Stages

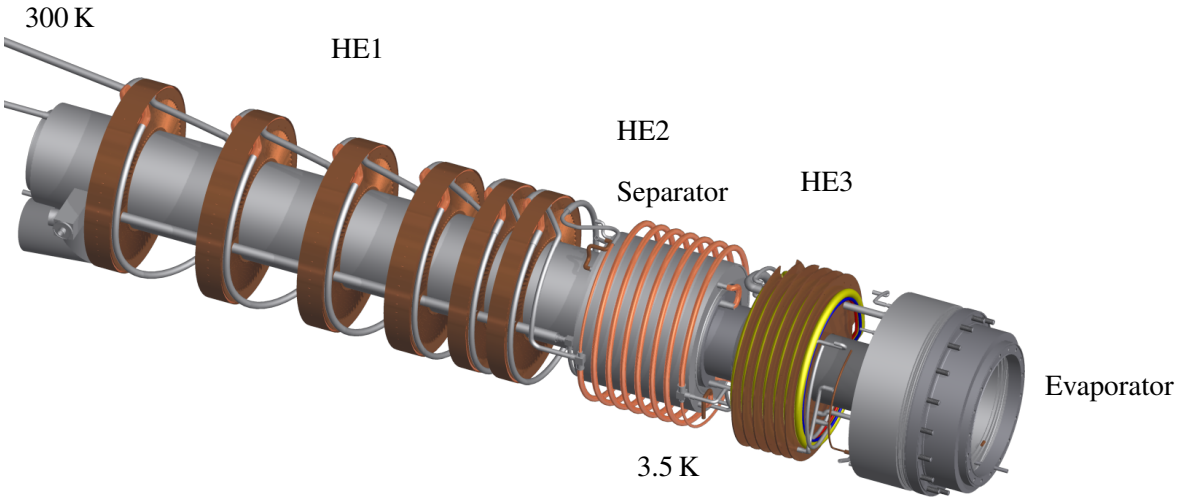

Figure 5.5: Sketch of the precooling unit

As mentioned before, the refrigerator consists of two main parts: the dilution unit and the precooling stages. The precooling stages, which are shown in Fig. 5.5 and 5.6, have to precool and liquefy the incoming ^{3}He-^{4}He mixture entering the refrigerator. For this the precooling consists of a series of counter flow heat exchangers cooled by two continuous flow ^{4}He evaporation stages called separator and evaporator. Radebaugh et all [75] have shown that such a design reduces the ^{4}He consumption and is used for a refrigerator working more economical. There are three counter flow heat exchangers, where the first two are supported by the separator, the third one by the evaporator. Each heat exchanger gets additional cooling by the ^{3}He back-streaming from the dilution unit. An additional heat exchanger is located inside the evaporator and operates as an heat sink to get the incoming mixture cooled down to 1 K before it enters the dilution unit.

First, the incoming ^{3}He-^{4}He mixture enters heat exchanger 1 (HE1) and is cooled from room temperature (300 K) to around 8 K. Afterwards heat exchanger 2 (HE2) cools the mixture to the temperature of the separator (around 3.5 K). Then, the ^{3}He-^{4}He mixture enters heat exchanger 3 (HE3) and is cooled to around 1 K. The ^{4}He flowing from the separator to the evaporator is cooled by HE3, too. This heat exchangers cool the incoming streams by ^{4}He from the separator and the evaporator and by the back-streaming ^{3}He-^{4}He. At the end of the precooling stages a heat exchanger (HE4) is located inside the evaporator as a thermal sink to ensure that the incoming ^{3}He-^{4}He mixture is cooled to the evaporator temperature of 1 K, independent of the circulating rate of the mixture. The following sections will give a more detailed view to the different parts of the precooling.

The results of the CFD simulations, mentioned in Chap. 4, are presented in this Chapter. This simulations give access to a more detailed view in the fluid dynamics of the precooling stages. In addition, all streams of the different heat exchangers are implemented in the simulations and the influence of the back streaming ^{3}He-^{4}He mixture is taken into account.

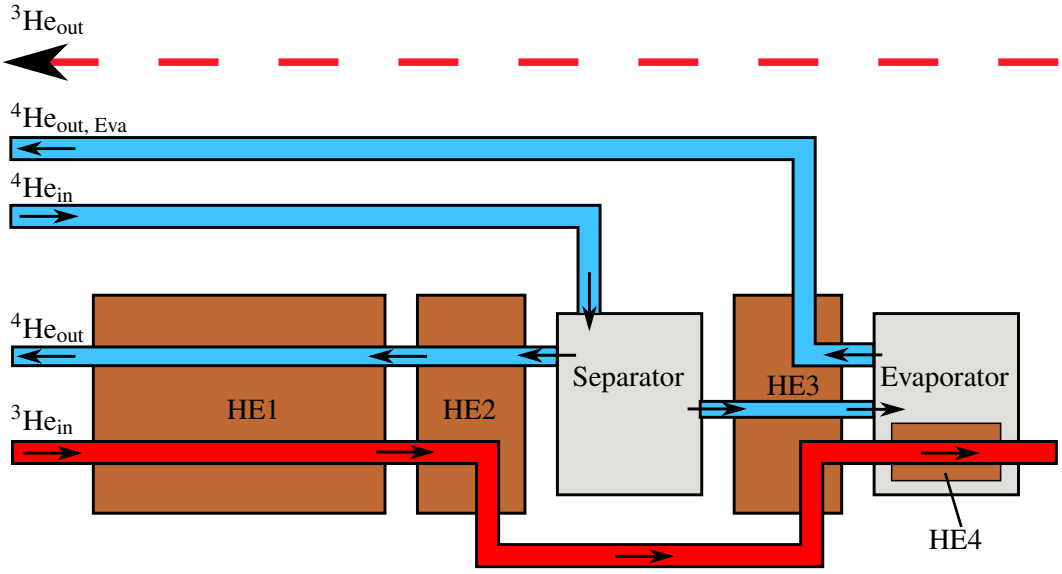

Figure 5.6: Scheme of the precooling unit and the different streams

5.2.1 Separator

The separator is formed by a cylindrical stainless steel chamber of 400 cm^3 volume. It is operated at a pressure range around 600 mbar to 700 mbar, which results in a temperature of the liquid ^{4}He of around 3.5 K. This enables a continuous filling through the transfer line with liquid helium from a Dewar at atmospheric pressure. The flow can be regulated by a needle valve, but depends on the different cooling stages and the setting of the helium support from the separator to these cooling stages. Inside the separator, a layer of sintered brass is mounted to purify the liquid helium. This is necessary to protect the other parts of the refrigerator from blocking from dirt and ice, coming from the Dewar. After the refrigerator is warmed up to room temperature, the separator can be evacuated to clean the filter brass. The separator is the first heat sink of the refrigerator and provides the liquid ^{4}He for liquefaction and to cool down the structure. Thus, the separator supports

- the evaporator,
- heat exchanger 1 and 2,
- the cooling of the internal polarisation magnet and the heat shields during the cool down procedure,
- a bypass to precool the dilution unit and in addition the indium seal of the insert (see Chap 5.5) can be cooled with liquid helium.

To reach the operation pressure of the separator, a rotary vane pump with 100 $m^3\,h^{-1}$ is used. Fig. 5.7 shows the dependence of the separator cooling power on its temperature. This relation was calculated under the usage of the latent heat and the flow rate.

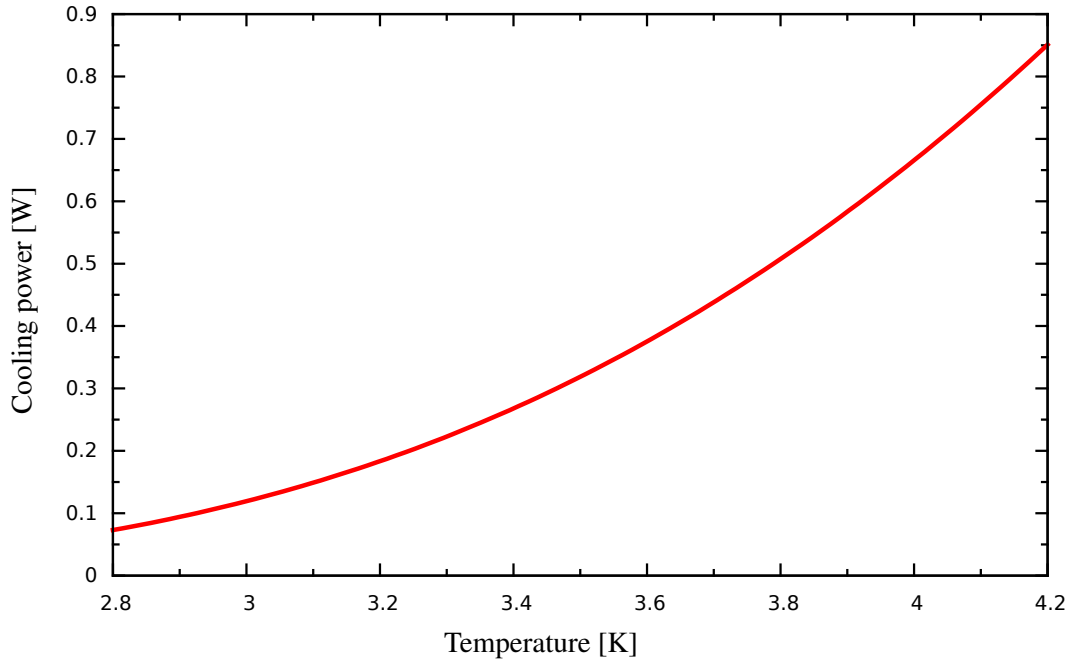

Figure 5.7: Cooling power of the separator.

The gas, leaving the separator through this pumping line, is used to cool the transfer line. This reduces the consumption of liquid helium in the precooling unit. The separator is also pumped by the heat exchanger cascade 1,2 and the evaporator to support them with liquid helium. The flow to this parts can be regulated by needle valves.

5.2.2 Heat exchanger 1 and 2

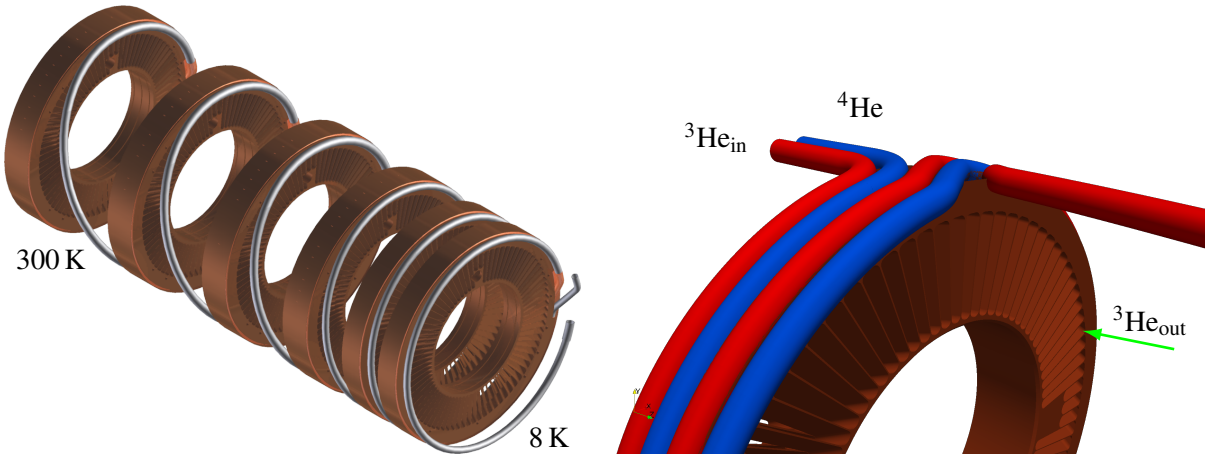

(a) All stages of heat exchanger 1

(b) Detailed view of one stage of heat exchanger 1

Figure 5.8: Construction sketches of heat exchanger 1

As mentioned before the ^{3}He-^{4}He mixture, necessary to cool the target, circulates in a closed system. Before it enters the dilution unit, the circulating mixture has to be cooled. For this, a series of counter

flow heat exchangers is used. Heat exchanger 1 and 2 cool the incoming mixture from room temperature ($\propto$ 300 K) to the temperature of the separator ($\propto$ 3.5 K). These heat exchangers are shown in Fig. 5.8 and 5.9. First the ^{3}He-^{4}He mixture enters HE1 and is cooled. Afterwards, the incoming mixture enters HE2 which cools it to the temperature of the separator. In both heat exchangers, the incoming stream is cooled with back streaming pure ^{4}He from the separator and the ^{3}He-^{4}He mixture from the dilution unit. The flow scheme is shown in Fig. 5.6. Thus, both heat exchangers can be seen as one cooling unit, due to the in series connected cooling streams. The ^{4}He back-stream is pumped by a rotary vane pump with 100 m^3 h^{-1} and the flow-rate of this back-stream can be regulated by an additional needle valve.

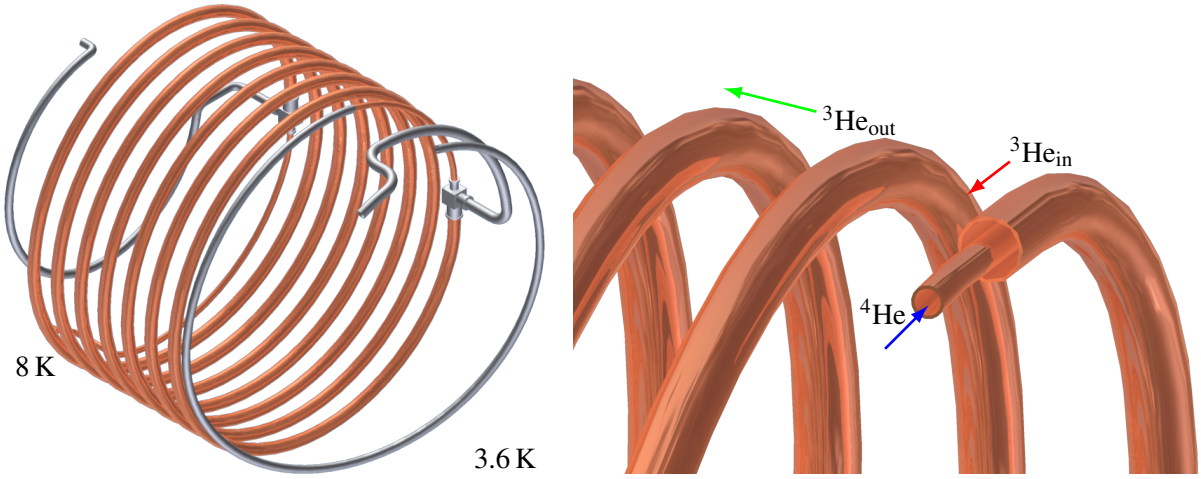

(a) Overview of heat exchanger 2

(b) detailed view of heat exchanger 2

Figure 5.9: Construction sketches of heat exchanger 2

To suggest an assumption of the performance of the precooling stages, CFD-Simulations based on the *chtMultiRegionSimpleFoam* [63] solver were performed. After the creation of the mesh, it is important to choose the correct boundary conditions.

The boundary *zeroGradient* says that the condition $\nabla\phi = 0$ has to be full-filled at the wall were this condition is used. Thus, the pressure condition *zeroGradient* is set to the walls and the outlet. The pressure at the inlet of the heat exchangers was set to a constant value. To ensure mass conservation the flow at the in- and outlet are set to a constant value but with opposite sign. This is necessary because the direction of the flow through a face is always given along the face normal and this is always directed into the mesh in OpenFOAM. The velocity of the fluid has to be zero at the walls. The boundary condition *compressible::turbulentTemperatureCoupledBaffleMixed* is used to translate the temperature conditions between the different sub-meshes of the simulation. For each fluid stream and each solid a sub-mesh is created with an interface at the connecting surfaces for interaction. How this boundary condition works has been described in Chap. 4.3.1. All other walls are set to *zeroGradient* which means that they are assumed to be adiabatic. Heat exchanger 1 consists of 6 copper turbine stages. To reduce the thermal conductivity along the structure these stages are interconnected with stainless steel tubes. Thus, the heat conductivity along these tubes could be ignored for this simulations. In Appendix A.4 the boundaries for heat exchanger 1 and 2 are summarised. Following the data for a ^{3}He-^{4}He circulation rate of 1 mmol s^{-1} are shown.

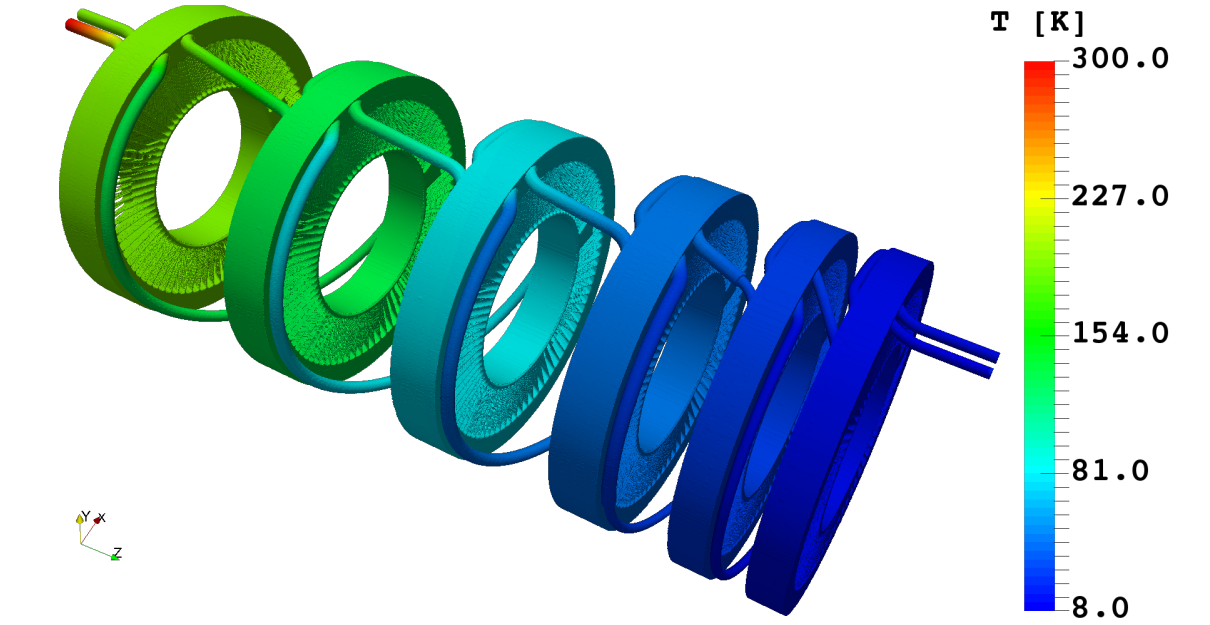

(a) Temperature data of heat exchanger 1

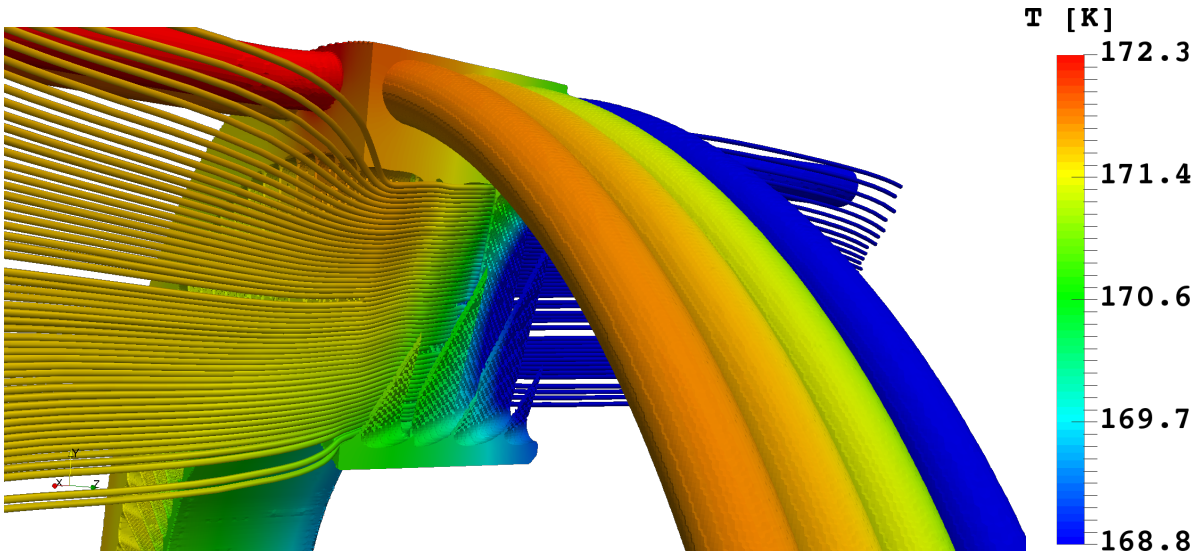

(b) detailed view of stage 6

Figure 5.10: Temperature data for heat exchanger 1 at 1 mmol s^{-1} ^{3}He circulation rate

Fig. 5.10 shows the simulated temperature profile for heat exchanger 1. It can be seen that the temperature profile for all streams and all stages of the heat exchanger was calculated. Also, each stage has a good defined mean temperature and is thermal uncoupled from the surrounding stages, as it can be seen in Fig. 5.10a. Due to the well defined temperature gradient along this heat exchanger, the heat conductivity along the refrigerator to the cooler front part is reduced. Fig. 5.10b shows the temperature profile for stage 6 in more detail and the three streams flowing through this stage. The out-going gaseous ^{3}He stream from the dilution unit is represented by the stream traces in this plot. The stream traces show that this back-stream trough HE1 is laminar as expected. In Fig. 5.11 the pressure field for all streams is presented.

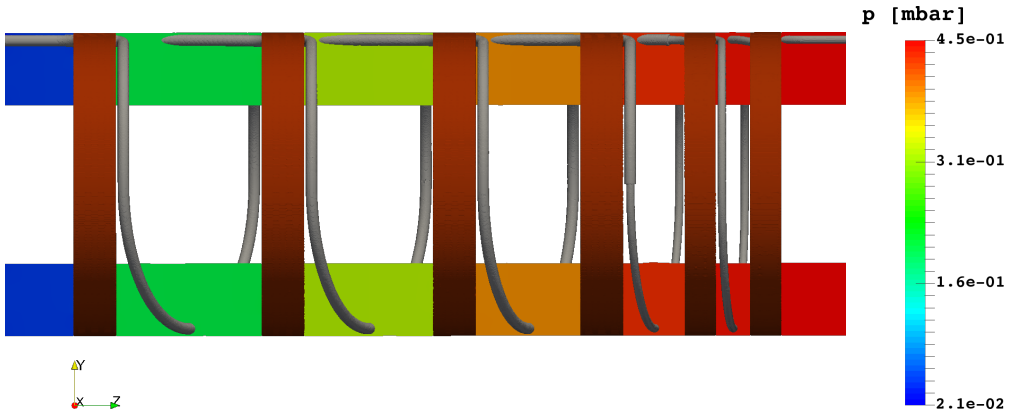

(a) pressure of the out-going ^{3}He

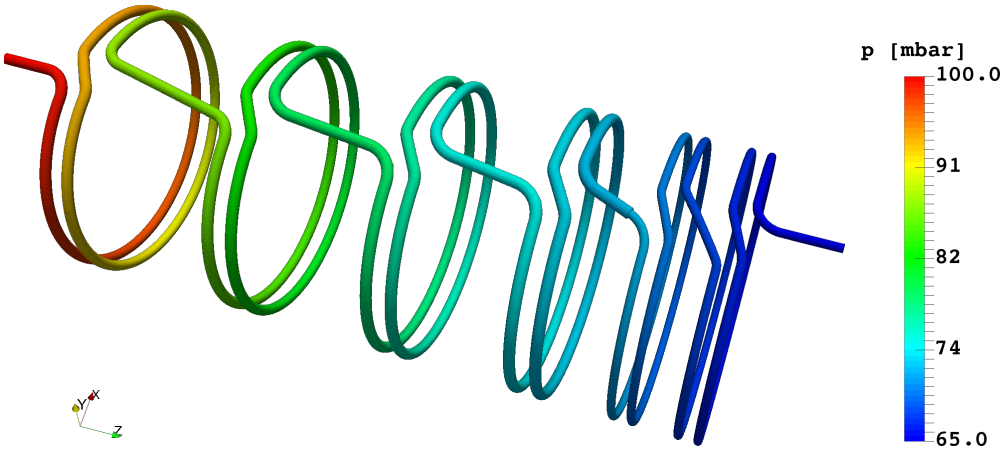

(b) pressure of the in-streaming ^{3}He

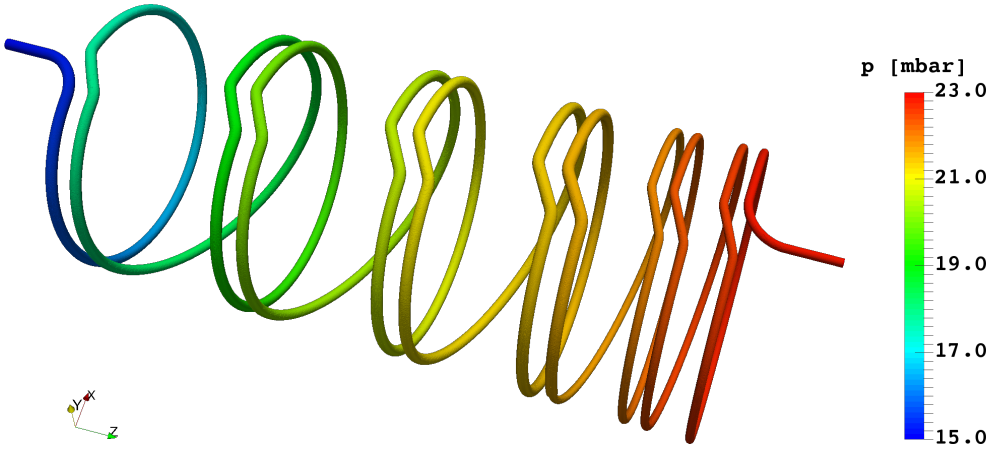

(c) pressure of the out-going ^{4}He

Figure 5.11: Pressure data for heat exchanger 1 at 1 mmol s^{-1} ^{3}He circulation rate

The pressure at the inlet for the ^{3}He-^{4}He mixture at HE1 could be measured to be 100±5 mbar which fits with the simulated data and the assumed inlet-pressure for the simulation. Also the measured pressure at the outlet of the ^{4}He stream of about 15±2 mbar fits to the simulated data. The outlet pressure of the out-

going ^{3}He-^{4}He was measured to be 2.4±0.5 mbar. The measurement at other positions was not possible.

The temperature profile for all fluid streams of heat exchanger 2 are shown in Fig. 5.12. Fig. 5.12d shows the temperature gradient of the out streaming ^{3}He-^{4}He mixture. Fig. 5.12a shows the temperature profile of the incoming ^{3}He-^{4}He mixture without the ^{3}He-^{4}He back-stream and Fig. 5.12b shows the temperature profile including both cooling streams. In comparison, the two data sets show that the additional cooling stream has a influence on the temperature at the outlet of the incoming ^{3}He-^{4}He mixture.

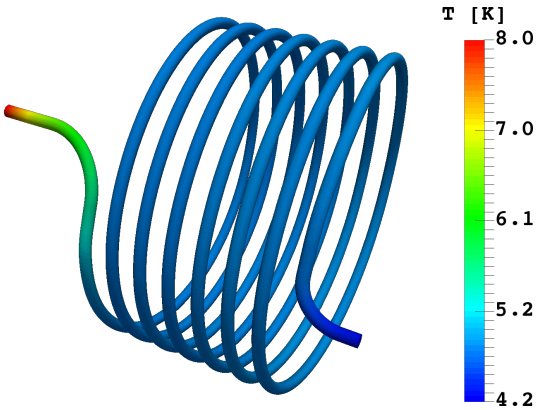

(a) Temperature gradient of the incoming ^{3}He, without cooling from the back streaming ^{3}He

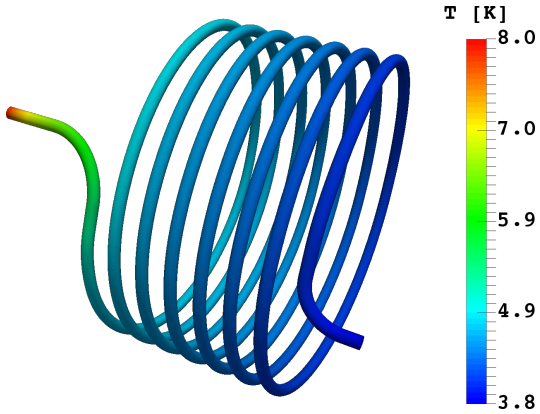

(b) Temperature gradient of the incoming ^{3}He

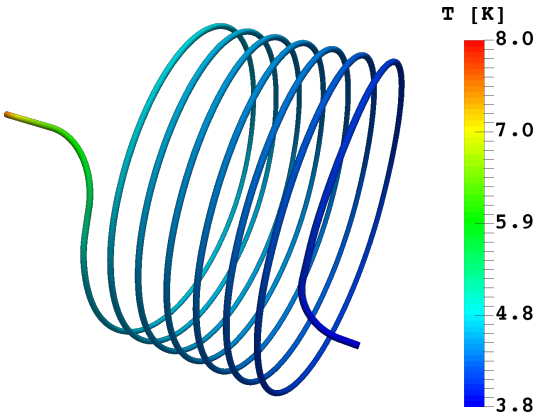

(c) Temperature gradient of the outgoing ^{4}He

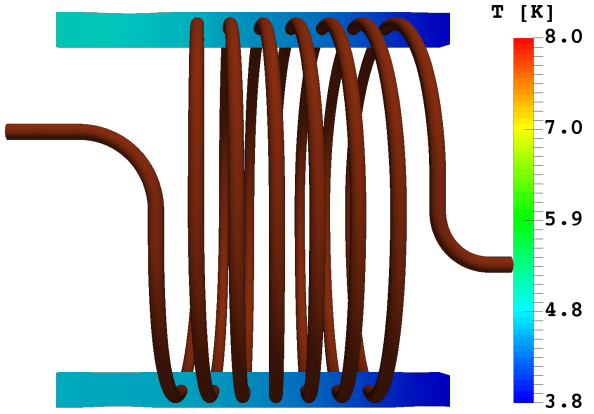

(d) Temperature gradient of the outgoing ^{3}He

Figure 5.12: Temperature data for heat exchanger 2 at 1 mmol s^{-1} ^{3}He circulation rate

If the flow is turbulent, there are several turbulence models which can be used for the simulation. A good description of the different most recent models is given in [61] and [62]. In the case of the different precooling heat exchangers, the fluid dynamic is well described by laminar flow. Therefore the Navier-Stokes equations can be solved directly. Referring to [42], helium behaves like an ideal fluid until the lambda point is reached. Thus, the thermophysical properties of a perfect fluid were used. Depending on the temperature region, the viscosity η was modelled by the Sutherland equation

$$\eta = \frac{A_S \sqrt{T}}{1 + \frac{T_S}{T}}, \tag{5.11}$$

where A_s is the SUTHERLAND constant and T_s the temperature at which the SUTHERLAND constant has been calculated. Also polynomial fits to the data from [47], [49], [45] and [76] permit the description of the behaviour of these values. The amount of ^{4}He in the circulating ^{3}He depends on the performance of the dilution unit. For a ideal working dilution refrigerator, the amount of ^{4}He in the circulation mixture is less than 4 %. Depending on the temperature of the still (see Chap. 5.3), this can go up to 15 %. This change in the mixture changes also the heat capacity and conductivity of the circulating ^{3}He-^{4}He mixture and thus, the performance of the precooling heat exchangers. The simulation was done with an ^{4}He amount up to 15 % in the circulating ^{3}He-^{4}He mixture, due to this fact. In addition, the simulations were done with pure ^{4}He, because the first test measurements were done with ^{4}He instead of the ^{3}He-^{4}He mixture.

The heat capacity and conductivity of the solid parts of the heat exchanger have to be modelled. This was done by the polynomial fits from [77]

$$\log c_{\mathrm{p,\,Copper}}(T) = \sum_{i=0}^{7} a_i \cdot (\log T)^i, \tag{5.12}$$

with

$$a_0 = -1.918\,44,\ a_1 = -0.159\,73,\ a_2 = 8.610\,13,\ a_3 = -18.996,\ a_4 = 21.9661 \tag{5.13}$$

$$a_5 = -12.7328,\ a_6 = 3.543\,22,\ a_7 = 0, \tag{5.14}$$

and

$$\kappa_{\mathrm{Copper}}(T) = \sum_{i=0}^{7} a_i \cdot T^i, \tag{5.15}$$

with

$$a_0 = -186.672,\ a_1 = 152.442,\ a_2 = -5.187\,05,\ a_3 = 0.074\,805\,9 \tag{5.16}$$

$$a_4 = -5.609\,29 \times 10^{-3},\ a_5 = 2.291\,93 \times 10^{-6},\ a_6 = -4.840\,49 \times 10^{-9},\ a_7 = 4.1374 \times 10^{-12}. \tag{5.17}$$

Under usage of the simulations, it is possible to predict the ^{4}He flow-rate, necessary to cool down a specific ^{3}He flow to the desired temperatures given in Fig. 5.8a and 5.9a, which is shown in Fig. 5.13.

These flow-rates, the pressure at the end of the outgoing streams, the inlet pressure for the dilute at HE1 and the temperature is measured to test the performance of the different cooling stages as discussed in Chap. 6. The measurement is in good agreement with the simulated data, if it is taken into account that the test fluid is pure ^{4}He. Thus, the simulation seems to describe the performance of these two heat exchangers very well. A more detailed description of the measurement is given in Chap. 6.2.

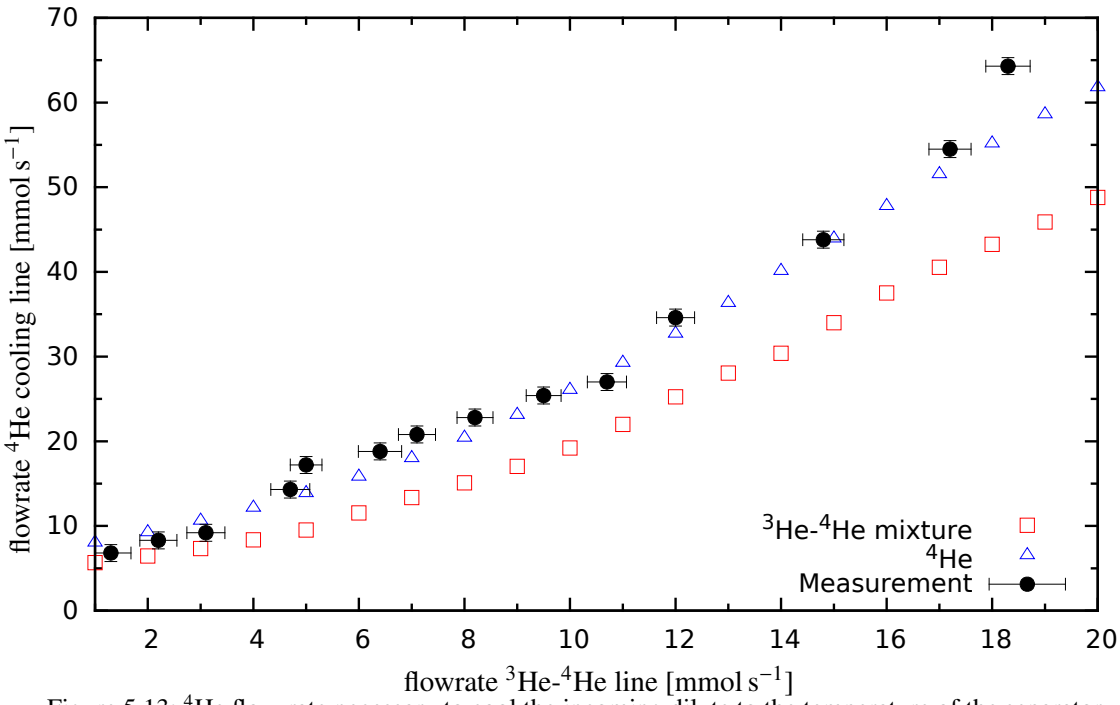

Figure 5.13: ^{4}He flow-rate necessary to cool the incoming dilute to the temperature of the separator

5.2.3 Heat exchanger 3

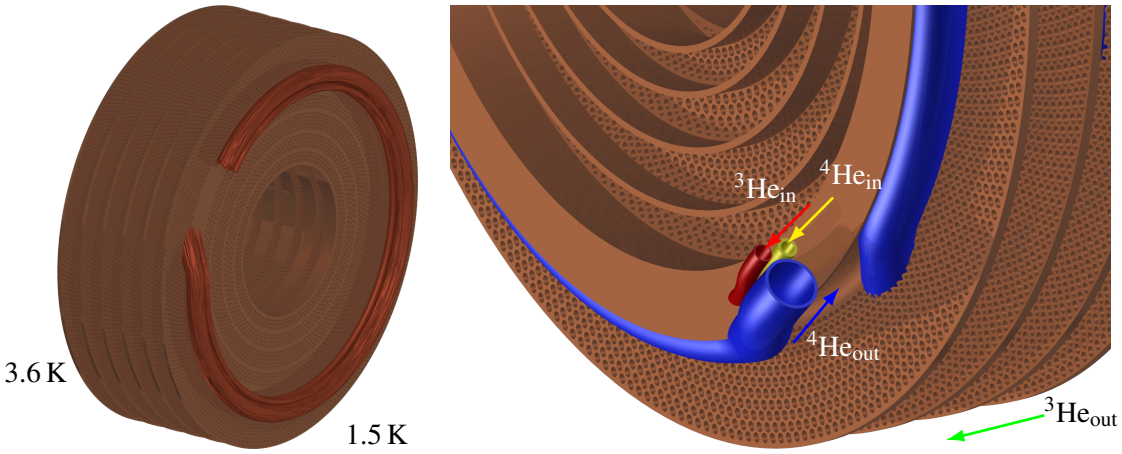

(a) Overview of heat exchanger 3

(b) detailed view of heat exchanger 3

Figure 5.14: Construction drawings of heat exchanger 3

The heat exchanger, shown in Fig. 5.14, is the part of the refrigerator having to liquefy the incoming dilute. It consists of 6 plate stages. The incoming dilute and the liquid ^{4}He from the separator, flowing to the evaporator, have to be cooled down to around 1 K. In contrast to the first two heat exchangers, this heat exchanger has two incoming streams which are cooled by two outgoing streams as shown in Fig. 5.14b.

The initial boundary conditions are mostly the same as for the different parts of heat exchanger 1 and 2. Only the low temperature data for the viscosity, the heat capacity and the heat conductivity have to be implemented. For ^{4}He, the Data collected by Donnely [47] and Keesom[78] [79] was used. The physical properties of ^{3}He are given by the book of Keller [40], the work of Black [80] and Greywall [45].

At this temperatures, the incoming ^{4}He stream from the separator to the evaporator becomes superfluid. Thus, the change in the heat conductivity and the heat capacity has to be taken into account to get an approximation as good as possible for the cooling of this heat exchanger. To simplify the simulation, the change in the viscosity was neglected. The incoming ^{4}He is only precooled for the evaporator and the change to the ^{4}HE II state should not have a huge influence on the performance of the heat exchanger. Nevertheless, the simulation gives only a upper limit for the performance of the refrigerator and a lower limit for the needed ^{4}He flow to cool the incoming streams.

Fig. 5.15 represents the temperature profile for a ^{3}He circulation rate of 1 mmol s^{-1}. As for heat exchanger 1, there is a well defined temperature gradient over the heat exchanger, due to the 6 cooling stages. Fig. 5.15b shows the temperature profile of stage 6 in detail. It can be seen, that most of the temperature drop is caused near the inlet of the incoming helium streams.

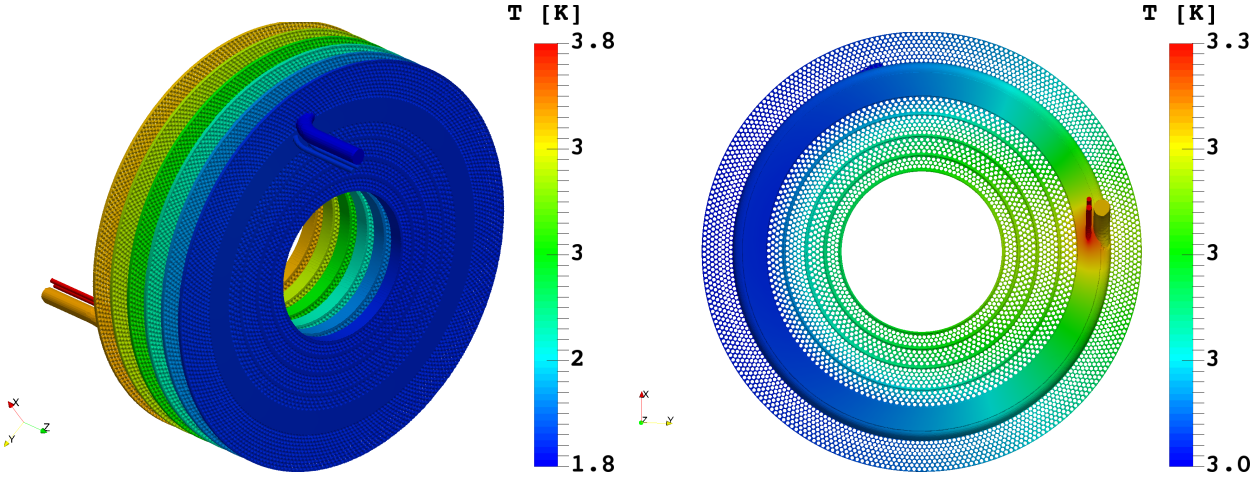

(a) Temperature data of heat exchanger 3

(b) Heat exchanger 3, temperature profile of stage 6

Figure 5.15: Temperature data of heat exchanger 3

The simulation shows that it is possible to use a small flow-rate of ^{4}He to liquefy and cool the circulating dilute. As in Chap. 5.2.2, the necessary ^{4}He rate to cool the incoming ^{3}He can be extracted from the simulation data as it is given in Fig. 5.16. To compare the simulation with the operation parameter of the refrigerator, the temperature at the in- and outlet of the incoming mixture has been measured and the pressure of the out-streaming ^{4}He can be measured outside the refrigerator. In addition, the flow-rate of each stream is measured as described in Chap. 6.

As Fig. 5.16 shows, the measurement and the simulation data are not as good in agreement as the data for HE1 and HE2. A possible source for this is the coarse model for the superfluid ^{4}He flowing from the separator to the evaporator. But as described in Chap. 6.2, due to a cold leak from the dilution unit to the

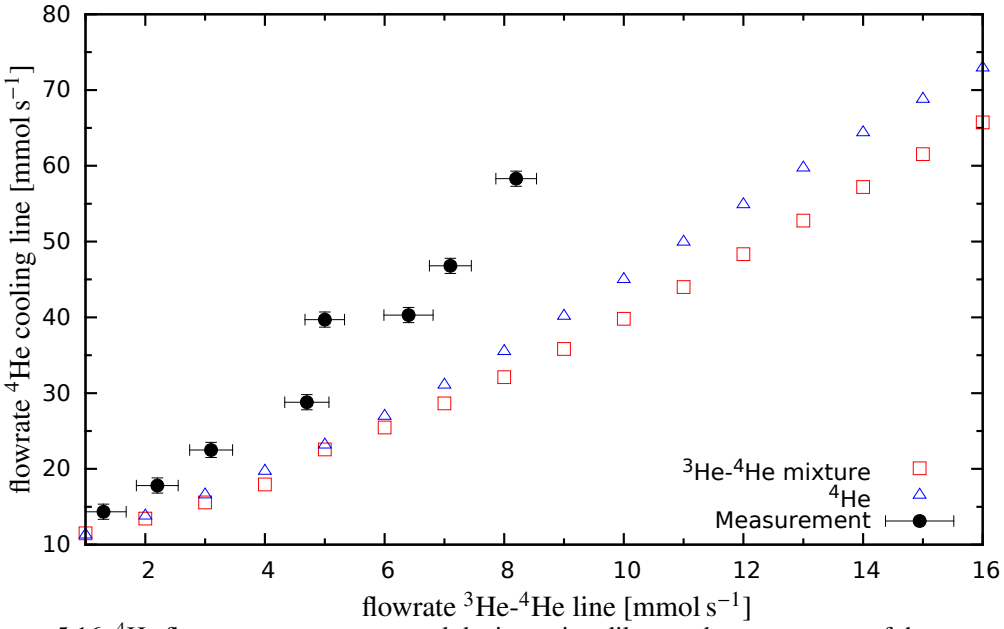

Figure 5.16: ^{4}He flow-rate necessary to cool the incoming dilute to the temperature of the evaporator

isolation vacuum it was not possible to reach the operation temperature of the evaporator of 1 K. The temperature of the evaporator was around 1.8 K during the tests which also increases the temperature of the ^{4}He cooling stream and influences the cooling power of HE3.

5.2.4 Evaporator and heat exchanger 4

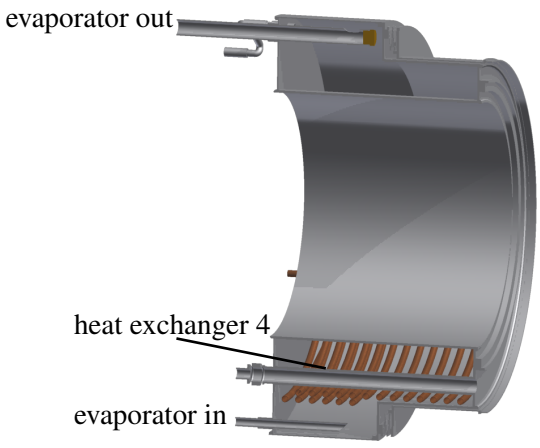

Figure 5.17: Construction drawing of the evaporator

The evaporator (shown in Fig. 5.17) is a stainless steel cylinder like the separator, with a volume of 1500 cm^3. It is fed with liquid ^{4}He from the separator, which is cooled by heat exchanger 3 before it enters the evaporator (see Chap. 5.2.3). In addition, a heat exchanger (HE4) is located inside the evaporator. This heat exchanger, shown in Fig. 5.17, has to ensure that the incoming ^{3}He-^{4}He mixture is cooled down to the temperature of the evaporator around 1 K. This thermal sink ensures a stable temperature of the incoming ^{3}He-^{4}He mixture for all possible circulation rates. The cooling power of

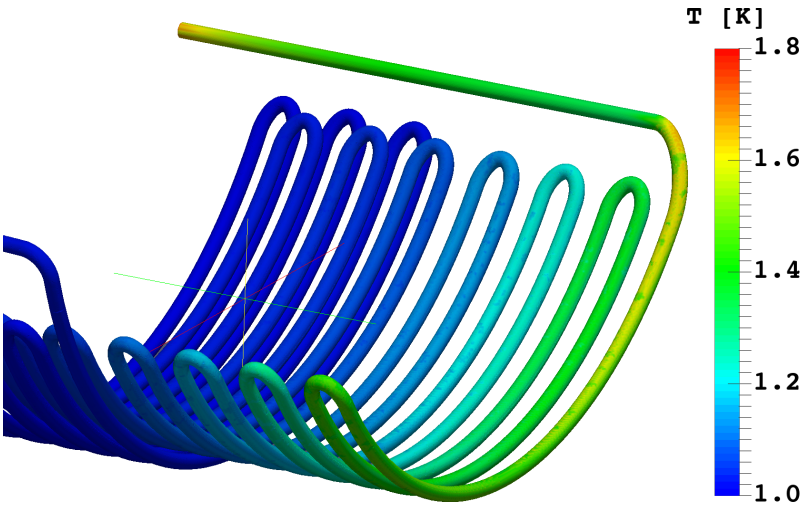

Figure 5.18: Temperature gradient for heat exchanger 4

the evaporator is also important, due to the fact that the evaporating gas is used to cool heat exchanger 3 and afterwards the beam-line through a set of turbine stages (see Chap. 5.5). To reach a evaporator temperature of 1 K, a rotary vane pump with a flow-rate of 250 $m^3\,h^{-1}$ is used. This leads to a pressure at the evaporator of 10 mbar to 20 mbar, depending of the ^{4}He flow rate. The cooling power depending on the temperature is shown in Fig. 5.19. To ensure that the evaporator works as a heat sink for all

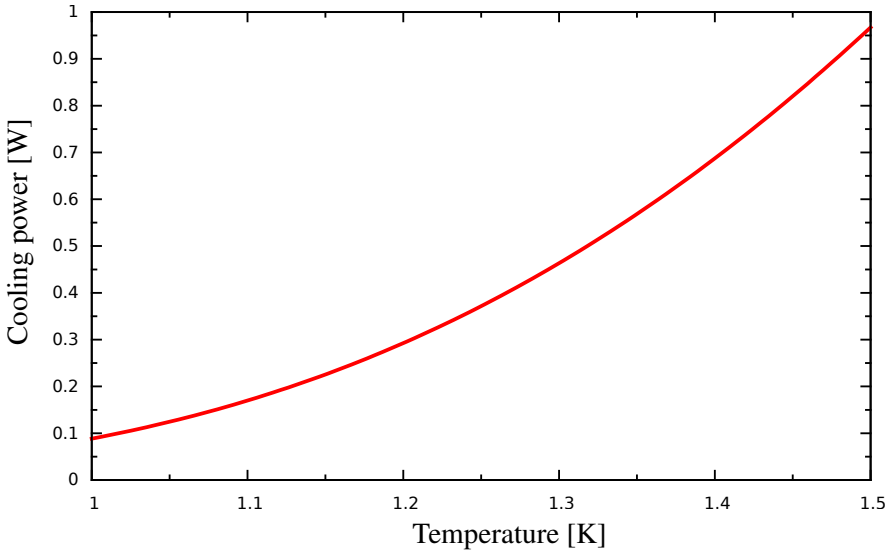

Figure 5.19: Cooling power of the evaporator.

^{3}He-^{4}He circulating rates, the cooling performance of heat exchanger 4 was simulated. Fig. 5.18 shows the temperature profile for the maximum circulating rate of 20 mmol s^{-1}. It is obvious that the cooling power of the evaporator is high enough to ensure a temperature of 1 K for the dilute before it enters the still. It is also possible to support the cooling of the internal coil and the heat shields with liquid ^{4}He from the evaporator instead of the separator. The lower temperature of the liquid provides a lower base temperature of the internal magnet if needed. The flow-rate of the evaporator and the flow to the cooling of the internal magnet can be regulated by needle valves.

5.3 The Dilution Unit

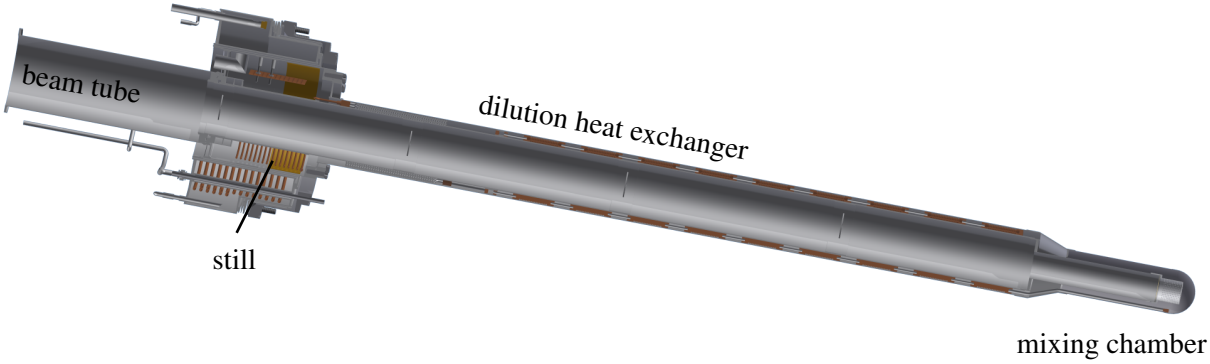

Figure 5.20: Construction sketch of the dilution unit

In Chap. 3.2, the principle of the dilution effect and the main components of a dilution refrigerator were discussed. It is obvious that the precooling unit of this new dilution refrigerator represents the condenser shown in Fig. 3.7. Due to the special geometry of the CB detector, the necessary 4π acceptance and the diameter of the external polarising magnet, the mixing chamber and the dilution heat exchanger, with the surrounding vacuum shell, is limited to a diameter of 94 mm. Fig. 5.20 shows the construction drawing of the dilution unit. After the ^{3}He-^{4}He mixture exits heat exchanger 3, it is guided through heat exchanger 4, located inside the evaporator, to the still. There, an additional heat exchanger ensures that the incoming dilute is thermalised to the temperature of the still around 700 mK. This heat exchanger consists of a 5 m long copper tube located in the helium bath of the still. Afterwards, the incoming mixture is guided through the main flow impedance to the last heat exchanger. This heat exchanger consists of 10 copper sintered stages to maximise the surface area and to uncouple the different stages for heat conductivity along the structure of the heat exchanger. Finally, the mixture enters the mixing chamber where the target is located. The mixture flows back through the heat exchanger to the still, and with the heater located there, it is possible to create the concentration gradient between mixing chamber and still which is necessary for the dilution effect.

A flow diagram of the dilution unit is shown in Fig. 5.21. The still is pumped by a series of root blowers of the pumping system. The whole test facility is described in Chap. 6. In the following, the different parts of the dilution unit will be described in more detail. The outgoing ^{3}He-^{4}He mixture is used for additional cooling on each main heat exchanger of the precooling unit before it exits the refrigerator at room temperature. The flow of the circulating ^{3}He-^{4}He mixture can be regulated with a needle valve before the incoming dilute enters the heat exchanger at the still. Also, a ^{4}He bypass from the separator to the dilution heat exchanger can be used to cool the refrigerator down from room temperature (300 K) to around 900 mK, where the refrigerator can be used as an ^{4}He evaporation system, too.

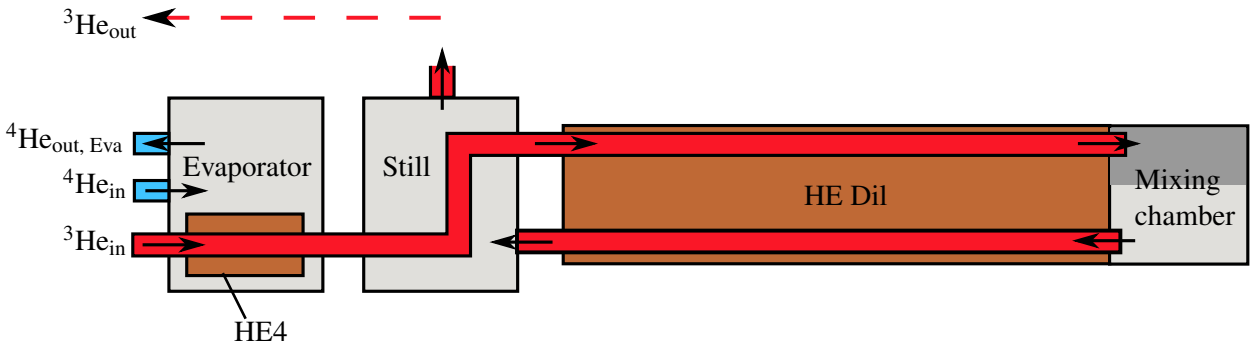

Figure 5.21: Flow diagram of the dilution unit

5.3.1 Mixing Chamber

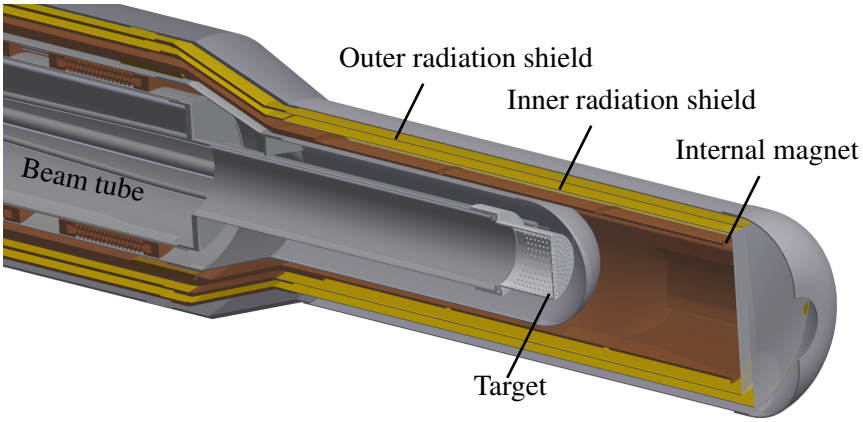

Figure 5.22: Cut through the mixing chamber

The mixing chamber is shown in Fig. 5.22. It is of a cylinder of aluminium situated in the front part of the refrigerator at the end of the beam-tube. It is surrounded by the heat shields and the internal magnet inside the vacuum jacket. Through the beam-tube, a NMR wire and a microwave guide enter the mixing chamber to polarise the target material and to measure the polarisation (see Chap. 2 and 6.1.4). Thus, the mixing chamber serves simultaneously as microwave cavity during the DNP.

The mixing chamber holds 180 ml of helium and is designed to provide target samples of up to 2 cm in length and diameter. As a consequence of the enthalpy balance given in Eq. 3.13, the temperature T_0 of the circulating ^{3}He leaving the last stage of the dilution heat exchanger and entering the mixing chamber may exceed the temperature of the diluted phase T_{mc} at most by a factor of $\frac{T_0}{T_{\mathrm{mc}}} \leq 2.8$. The maximum is reached when no additional heat is applied to the mixing chamber. Chap 5.1.5 shows the heat load through the thermal insulation. Dependent on the beam energy and flux an additional heat source increases the minimal target temperature.

5.3.2 Still

The still, which is surrounded by the last part of the precooling stages, the evaporator, is of major importance for the performance of the dilution refrigerator. Like the separator and the evaporator, it is a stainless steel vessel with a volume of 0.3 l. As shown in Fig. 5.23, a heater and a level meter is located

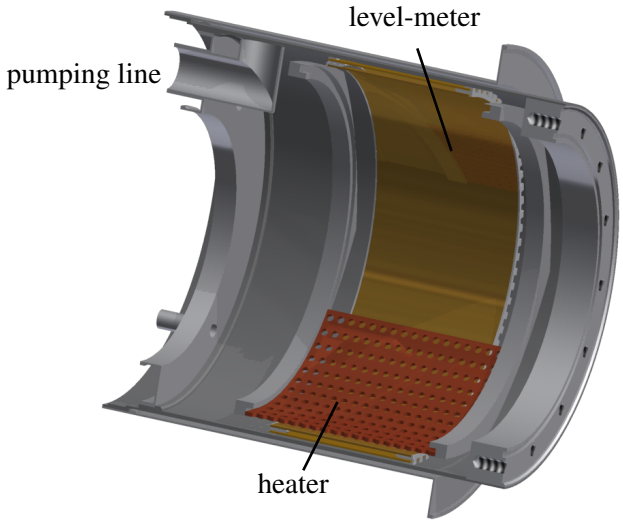

Figure 5.23: Cut through the still

at the still. The heater is necessary to heat the still to an operational temperature of $T_{\text{still}} \approx 700\text{mK}$. The temperature of the still has no direct effect on the temperature of the mixing chamber T_{mc}, but on the vapour pressure ratio of the ^{3}He-^{4}He mixture at the still. Thus, the temperature of the still affects the osmotic pressure π_{still} between still and mixing chamber. This pressure can be calculated by

$$\pi_{\text{st}} = \frac{x_{\text{st}} \cdot R \cdot T_{\text{still}}}{V_{^4\text{He}}}. \tag{5.18}$$

It is the van't Hoff law with the gas constant R, the volume $V_{^4\text{He}}$ of ^{4}He and can be used for $T_{\text{still}} > 150\,\text{mK}$. Below this value, the osmotic pressure is independent of the temperature and proportional to the ^{3}He concentration by $\propto x^{\frac{5}{3}}$. Thus, for the mixing chamber, where $x_{\text{st}} = 6.6\,\%$, π_{mc}, it is around 20 mbar. In order to suck ^{3}He from the mixing chamber to the still, $\pi_{\text{st}} \ll \pi_{\text{mc}}$ has to be fulfilled, which corresponds to $x_{\text{st}} = 0.9\,\%$ at 700 mK. For this, it is necessary that the temperature of the still is constant. This is maintained by a conventional heater. With a resistance of $100\,\Omega$, it is possible to use low currents and voltage to heat the still to the necessary temperature. This heat should compensate the cooling due to the heat of evaporation at the still

$$\dot{Q}_{\text{still}} = \dot{n}_{^3\text{He}} \cdot L_{^3\text{He, still}}, \tag{5.19}$$

where $L_{^3\text{He, still}}$ represents the latent heat of the ^{3}He depending on the still temperature and $\dot{n}_{^3\text{He}}$ is the circulation rate of ^{3}He. Pobell [42] gives $40\,\text{mW}\,\text{mmol}^{-1}\,\text{s}$ as a rule of thumb.

One of the most crucial points in the design of the still is the ^{4}He super-fluid film flow. It leads to an increase of the ^{4}He evaporation rate and to a contamination of the circulating dilute by ^{4}He. This

does not affect directly the mixer temperature, due to the enthalpy balance of the mixing chamber, but a higher amount of ^{4}He in the circulating dilute lowers the effective ^{3}He circulation rate. The reason of this is the constant total volume flow, given by the pumping system. This should not increase the temperature of the mixing chamber dramatically, but due to the specific heat of ^{3}He-^{4}He mixtures, which is considerably higher than for pure ^{3}He, the efficiency of the dilution heat exchanger decreases with increasing ^{4}He amount.

In order to minimise the film flow, the still is evaporated through the pumping line shown in Fig. 5.23, since the effect is directly proportional to the inner circumference of the pumping aperture.

In addition, the still contains a level meter (see Fig. 5.23) to measure the helium level inside the dilution unit. The level meter consists of two brazen cylinder which are working as an electric capacity. Depending on the liquid helium level, the measured capacity changes from 226 pF (empty still) to 238 pF. Due to the non linear behaviour of the capacity, a LCR measurement bridge of the type E4980A from *Keysight* is used.

5.3.3 Main Flow Impedance

Before the incoming dilute enters the last heat exchanger, it passed through a flow impedance Z, which provides a pressure drop, depending on the volume flow $\dot{V}$ and the dynamic viscosity η

$$\Delta p = Z \cdot \dot{V} \cdot \eta. \tag{5.20}$$

It is important to find the optimum value for the flow impedance, since an isenthalpic expansion of the liquid causes a temperature rise by

$$\left(\frac{\partial T}{\partial P}\right)_H = -\frac{1}{c_{^3\mathrm{He,p}}}\left[v_{^3\mathrm{He}} - T\left(\frac{\partial v_{^3\mathrm{He}}}{\partial T}\right)_P\right], \tag{5.21}$$

with v the molar volume and $c_{^3\mathrm{He,p}}$ the heat capacity of ^{3}He. At low temperatures, the second term becomes negligible and the heat load, which would charge the heat exchanger, is given by the first term. At 0.7 K this gives $\left(\frac{\partial T}{\partial P}\right)_H = 1\,\mathrm{mK\,mbar^{-1}}$, which is an significantly heat load to the dilution heat exchanger as Radebaugh and Siegwarth mentioned in [81].

The dilution heat exchanger is a design which is already used for the frozen spin target of the A2 collaboration in Mainz [82]. Thus, the same value for the flow impedance of $1.5 \times 10^8\,\mathrm{cm^{-3}}$ is used as in the Mainz/Dubna dilution refrigerator. The flow impedance in the dilution refrigerator, described in this thesis, consists of two parallel stainless steel tubes with an annulus surface. With a length $l_{\mathrm{tube}} = 1$ m and the diameters $d_{\mathrm{outer\,tube}} = 1.6$ mm and $d_{\mathrm{core}} = 1$ mm The flow impedance can be calculated by

$$Z = 128 \cdot \frac{l_{\mathrm{tube}}}{\pi \cdot d^4_{\mathrm{hydraulic}}} = 3 \times 10^8\,\mathrm{cm^{-3}} \tag{5.22}$$

with the hydraulic diameter

$$d_{\mathrm{hydraulic}} = d_{\mathrm{outer\,tube}} - d_{\mathrm{core}}. \tag{5.23}$$

Due to the parallel arrangement of the two annulus tubes this gives a flow impedance of $1.5 \times 10^8\,\mathrm{cm^{-3}}$.

5.3.4 Heat Exchanger

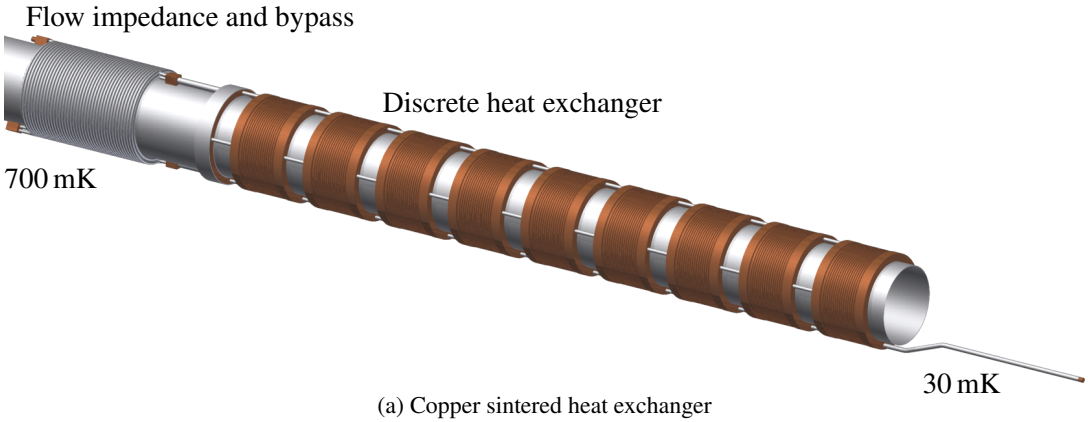

(a) Copper sintered heat exchanger

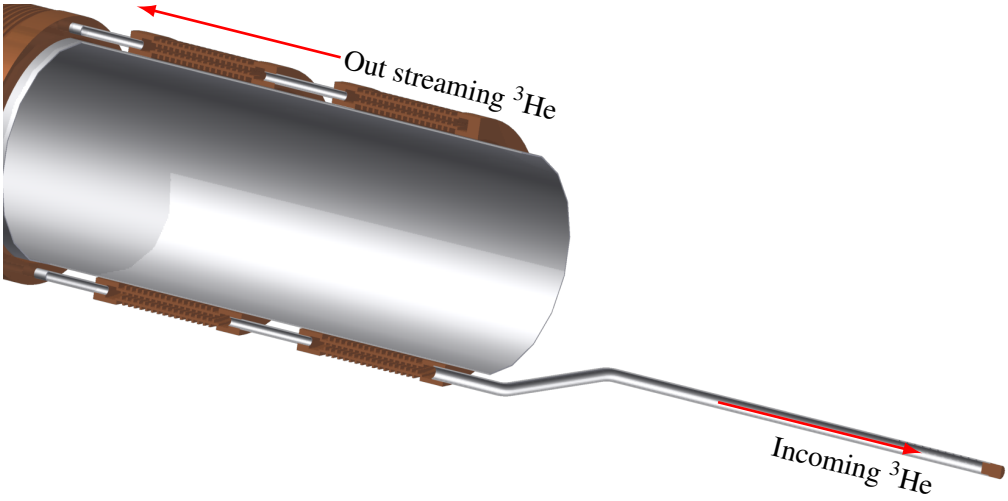

(b) Detailed view of the dilution heat exchanger

Figure 5.24: Construction sketches of the dilution heat exchanger

As a consequence of the above mentioned condition $\frac{T_0}{T_{mc}} \leq 2.8$, the quality of the last heat exchanger gives a limit for the performance of the dilution refrigerator. Fig. 5.24a shows the construction drawing of the heat exchanger used in this refrigerator. This cooling stage consists of two parts: The flow impedance (see Chap. 5.3.3) and a discrete heat exchanger. Continuous heat exchangers are favourable when the total heat conductance is small compared to the total heat transfer. Thus, the stainless steel tubes containing the flow impedance is used as a first step continuous heat exchanger before the fluid enters the discrete heat exchanger. The flow impedance of $1.5 \times 10^{-8}\,\mathrm{cm}^{-3}$ prevents bubble building after the still, due to reevaporation of the gas-mixture. This reevaporation and recondensation would not change the enthalpy and would not cause a direct thermal heat load, but it would affect the temperature difference and the heat transfer, which should be avoided.

In the temperature region below 200 mK axial conduction becomes more important, such that the heat exchanger is broken into several, isolated segments. This discrete part consists of 10 stages in order to compensate the increasing Kapitza heat resistance for decreasing temperatures which was mentioned in Chap. 3.3. Fig. 5.24b shows a cut through the last two stages. The incoming dilute streams through

stainless steel connecting tubes inside the copper sintered cooling stages and is cooled by the outstreaming ^{3}He around the stages. Since the KAPITZA resistance of the concentrated and the diluted side are in series, the thermal boundary resistance on both sides should best be equal. Due to a thin film of ^{4}He (with density ρ_{dl}) coating the surfaces of both sides (σ_{con} and σ_{dil}), leading to

$$R_{\mathrm{KAPITZA}} = \frac{\rho_{\mathrm{dl}}}{(\sigma_{\mathrm{con}} + \sigma_{\mathrm{dil}})}, \tag{5.24}$$

the best performance is reached if the surface area of both streams is equal. The heat exchanger consists of 10 stages which provide a total surface area of $\sim 27\,\mathrm{m}^2$, which results in $2.7\,\mathrm{m}^2$ per stage. Each stage consists of two sintered copper parts to provide this huge surface area in the small space around the last 1 m of the beam-tube. It is designed for a low flow impedance to prevent JOULE heating in the last cooling stages.

The sintered heat exchanger was designed and constructed in cooperation with the Joint Institute for Nuclear Research (JINR) Dubna. The minimal temperature at the mixing chamber for this dilution refrigerator has to be calculated to $T_{\mathrm{mc}} \approx 30\,\mathrm{mK}$ [56]. In addition, this design is used in the frozen-spin target for the A2 collaboration in Mainz [82] and reached temperatures around 25 mK under experimental conditions. Due to the fine structure of the copper sintered heat exchanger stages, it was not possible to create a mesh for the simulation with a FVE program as it was performed in Chap. 5.2. The following analysis of the heat exchanger was done, which is similar to the analysis of Frossati [21].

Eq. 3.13 is only full-filled, if the outlet temperature of the heat exchanger is independent of the circulation rate. This is the case for low flow rates where the effectiveness of the heat exchanger is high. The maximum cooling power can be calculated by

$$\frac{\mathrm{d}\dot{Q}}{\mathrm{d}\dot{n}_3} = 0. \tag{5.25}$$

This can only be applied for a constant still temperature T_{still}, a constant temperature of the mixing chamber T_{mc} and a constant ^{3}He-^{4}He ratio of the circulating mixture. Then the ^{3}He circulation rate is given by

$$\dot{n}_3 = \frac{H_{\mathrm{d}}(T_{\mathrm{mc}}) - H_{\mathrm{c}}(T_0)}{c_{\mathrm{c}}(T_0)} \cdot \frac{\mathrm{d}\dot{n}_3}{\mathrm{d}T_0}, \tag{5.26}$$

with c_{c} the specific heat of helium of the concentrated stream and $H_{\mathrm{D,c}}$ the enthalpy of the two phases. In order to calculate the ratio $\frac{\mathrm{d}T_0}{\mathrm{d}\dot{n}_3}$, the gradient $\frac{\mathrm{d}T}{\mathrm{d}z}$ of both streams in a counter-current heat exchanger, as shown in Fig. 5.24, along the flow direction z has to be analysed. This temperature gradient is determined by

- the heat exchange between the liquids and the solid body of the heat exchanger,
- by axial conduction along the streams and the body,
- the frictional heat,
- the enthalpy change.

In addition, the heat exchange $\dot{Q}_{\mathrm{HE}}$ between the liquid streams and the body of the temperature T_{HE}

depends on the Kapitza resistance ρ (see Chap. 3.3) and the heat transfer surface area σ by

$$\frac{\mathrm{d}\dot{Q}_{\mathrm{HE}}}{\mathrm{d}z} = -\frac{\mathrm{d}\sigma(z)}{\mathrm{d}z}\int_{T_{\mathrm{HE}}}^{T(z)}\frac{\mathrm{d}T}{\rho(z)}. \tag{5.27}$$

The boundary resistance of pure ^{3}He, in the temperature region between 10 mK and 130 mK, has been measured and can be expressed by

$$\rho_{\mathrm{con}} = 200 \cdot T^{-3}\ \mathrm{cm^2\,K\,W^{-1}}[54]. \tag{5.28}$$

Whereas, the data between 130 mK and 700 mK can be represented by

$$\rho_{\mathrm{con}} = \left(240 \cdot T^{-4} + 155 \cdot T^{-3}\right)\ \mathrm{cm^2\,K\,W^{-1}}. \tag{5.29}$$

The boundary resistance of the concentrated phase can be expressed by this equations in first approximation. For the dilute stream the Kapitza resistivity for temperatures below 200 mK was determined by [55] to be about

$$\rho_{\mathrm{dil}} = 70 \cdot T^{-3}\ \mathrm{cm^2\,K\,W^{-1}}. \tag{5.30}$$

For a counter-flow heat exchanger, used in this setup, the axial heat conduction depends on the thermal conductivity κ for the liquid streams and the body of the heat exchanger, and on the cross section area A perpendicular to the flow, which leads to

$$\frac{\mathrm{d}\dot{Q}_{\mathrm{axial}}}{\mathrm{d}z} = A \cdot \left[\kappa(z)\frac{\mathrm{d}^2T(z)}{\mathrm{d}z^2} + \frac{\mathrm{d}\kappa(z)}{\mathrm{d}T}\left(\frac{\mathrm{d}T(z)}{\mathrm{d}z}\right)^2\right]. \tag{5.31}$$

Abel et al [83] determined the thermal conductivity for the liquid streams of a copper sintered heat exchanger to

$$\kappa_{\mathrm{con}} = \left(3.84T^{-1} + 31.4 + 58.1T\right)\ \mu\mathrm{W/cmK}, \tag{5.32}$$

for the concentrated side and

$$\kappa_{\mathrm{dil}} = 3000T_{\mathrm{dil}}^3 + 2.6T_{\mathrm{dil}}^{-1}\ \mu\mathrm{W/cmK} \qquad \text{for } T_{\mathrm{dil}} < 100\,\mathrm{mK}, \tag{5.33}$$

$$\text{and}\quad \kappa_{\mathrm{dil}} = 5400 \cdot (T_{\mathrm{dil}} - 45\,\mathrm{mK})\ \mu\mathrm{W/cmK} \qquad \text{for } T_{\mathrm{dil}} \geq 100\,\mathrm{mK}, \tag{5.34}$$

at the diluted stream. As in [21] mentioned, the viscous heating can be written as

$$\frac{\mathrm{d}\dot{Q}_{\mathrm{vis}}}{\mathrm{d}z} = \eta(z) \cdot (V \cdot \dot{n}_3)^2 \cdot \frac{\mathrm{d}Z(z)}{\mathrm{d}z}, \tag{5.35}$$

where Z is the flow impedance and η the viscosity of ^{3}He. V is the molar volume. At temperatures in the milli-kelvin region, the viscosity of the liquid ^{3}He is given by [84] by

$$\begin{aligned} \eta_{\mathrm{con}} &= 2.25 \cdot T^{-2}\ \mu\mathrm{Poise\ K}^2, \\ \text{and}\quad \eta_{\mathrm{dil}} &= 0.6 \cdot T^{-2}\ \mu\mathrm{Poise\ K}^2. \end{aligned} \tag{5.36}$$

Due to Eq. 5.36, the viscosity reaches high values at low temperatures. As a result of the conservation of energy in each segment of the heat exchanger, one obtains two coupled differential equations for the enthalpy change of the concentrated and the diluted stream:

$$\begin{aligned} c_{\mathrm{con}}(z)\,\dot{n}_3 \cdot \frac{\mathrm{d}T_{\mathrm{con}}}{\mathrm{d}z} =& A_{\mathrm{con}} \left[\kappa_{\mathrm{con}}(z) \cdot \frac{\mathrm{d}^2 T_{\mathrm{con}}(z)}{\mathrm{d}z^2} + \frac{\mathrm{d}\kappa_{\mathrm{con}}(z)}{\mathrm{d}T_{\mathrm{con}}} \cdot \left(\frac{\mathrm{d}T_{\mathrm{con}}(z)}{\mathrm{d}z} \right)^2 \right] \\ &+ \eta_{\mathrm{con}}(z) \cdot (V_{\mathrm{con}} \cdot \dot{n}_3)^2 \cdot \frac{\mathrm{d}Z_{\mathrm{con}}(z)}{\mathrm{d}z} + \frac{\mathrm{d}\sigma_{\mathrm{con}}(z)}{\mathrm{d}z} \int_{T_{\mathrm{b}}}^{T_{\mathrm{con}}(z)} \frac{\mathrm{d}T}{\rho_{\mathrm{con}}(z)} \end{aligned} \tag{5.37}$$

$$\begin{aligned} c_{\mathrm{dil}}(z)\,\dot{n}_3 \cdot \frac{\mathrm{d}T_{\mathrm{dil}}}{\mathrm{d}z} =& A_{\mathrm{dil}} \left[\kappa_{\mathrm{dil}}(z) \cdot \frac{\mathrm{d}^2 T_{\mathrm{dil}}(z)}{\mathrm{d}z^2} + \frac{\mathrm{d}\kappa_{\mathrm{dil}}(z)}{\mathrm{d}T_{\mathrm{dil}}} \cdot \left(\frac{\mathrm{d}T_{\mathrm{dil}}(z)}{\mathrm{d}z} \right)^2 \right] \\ &+ \eta_{\mathrm{dil}}(z) \cdot (V_{\mathrm{dil}} \cdot \dot{n}_3)^2 \cdot \frac{\mathrm{d}Z_{\mathrm{dil}}(z)}{\mathrm{d}z} + \frac{\mathrm{d}\sigma_{\mathrm{dil}}(z)}{\mathrm{d}z} \int_{T_{\mathrm{b}}}^{T_{\mathrm{dil}}(z)} \frac{\mathrm{d}T}{\rho_{\mathrm{dil}}(z)} \end{aligned} \tag{5.38}$$

Thus, a mathematically description of real heat exchangers is not trivial. One has to solve the coupled differential equations for the concentrated and diluted stream. For the calculation, the heat capacity of the concentrated phase c_{con} is taken as calculated by Radebaugh [85], while the dilute phase heat capacity c_{dil} is replaced by the heat capacity at constant osmotic pressure under the assumption of zero mixer temperature $T_{\mathrm{mc}} = 0$. The resulting error caused by this simplification should be less than 10 % [86].

In order to estimate the influence of axial conduction, along a length L, on the performance of the exchanger, the thermal resistance ratio W of the liquid axial resistance to the Kapitza resistance is calculated

$$W = \frac{A \cdot \kappa \cdot \rho}{L \cdot \sigma}. \tag{5.39}$$

Since the thermal resistance ratio increases with decreasing temperature, $W \leq 0.05$ serves as an upper limit in the whole exchanger and axial conduction by the liquid should be insignificant. The axial conduction along the heat exchanger is reduced by the stainless steel interconnecting tubes and can be ignored in the following calculation.

Eq. 5.37 and 5.38 are used to calculate the temperature gradient for the copper sintered segments of the heat exchanger numerically for each stream with the boundary condition that axial conduction must be continuous at the transition to the interconnecting tubes. This calculation is similar to the analysis of Soegwarth and Radebaugh [86]. The heat flow between two segments is reduced by stainless steel tubes with a small wall thickness. Due to the small surface of the tubes and the Kapitza resistance it is assumed for the calculation that the temperature between two stages is almost constant.

To simplify the calculation it is assumed, that the temperature of the heat exchanger body is constant. Also, the calculation was performed for a temperature at the mixing chamber of 30 mK, which is related to the inlet temperature of the last segment of the discrete heat exchanger. The outlet temperature of

81.7 mK was calculated by Eq. 3.12 using the calculated heat load of 39.3 µW from Chap. 5.1.5. Now the equation system is solved by varying T_{body} until the heat transfer on the concentrated and the diluted side comes equal. It is helpful to define the relative effectiveness [19] of a heat exchanger

$$R = \frac{T_{con}^{in} - T_{con}^{out}}{T_{con}^{in} - (T_{con}^{out})_{\sigma=\infty}}. \tag{5.40}$$

This effectiveness indicates the ratio of temperature change of the incoming stream to the maximum possible change, which is the case of infinite surface area and leads to $T_{body} = T_{con} = T_{dil}$. The effectiveness depends on the circulation rate of the fluid. This leads to a relative effectiveness of $R = 64\,\%$ for the last segment of the heat exchanger for a circulation rate of $1\,\mathrm{mmol\,s^{-1}}$. Since R increases strongly with the operating temperature, the effectiveness of the other exchanger segments is almost near to 100 %. Fig. 5.25 shows the temperature gradient of the last stage resulting from these calculations. The calculated temperature profile is only an assumption to the real temperature development in the discrete heat exchanger, since after this calculation only eight segments would be necessary. The additional two segments should improve the performance and ensure the design temperature of 30 mK.

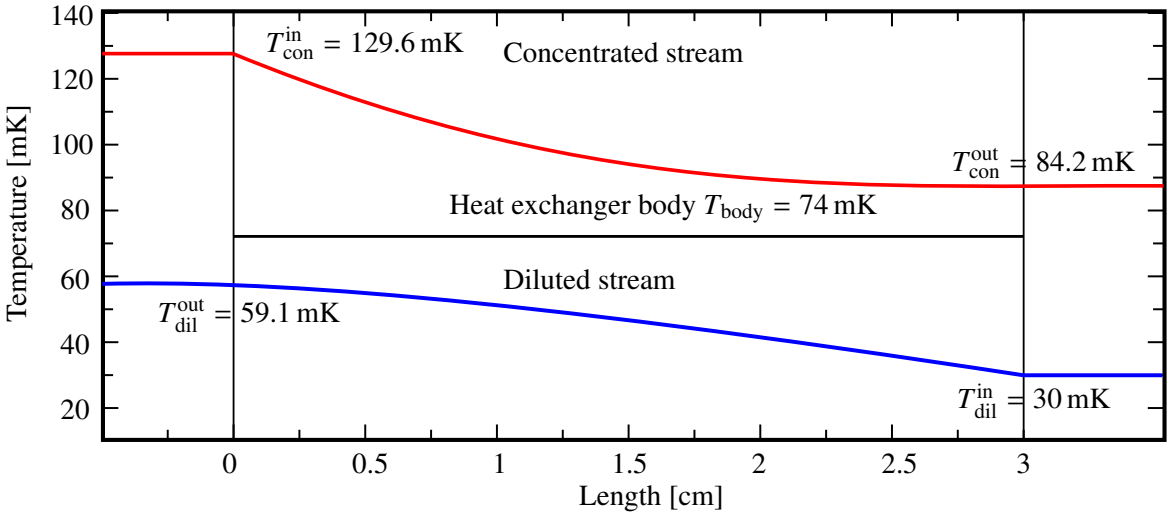

Figure 5.25: Temperature profile of the last stage of the discrete heat exchanger for both streams.

5.4 The Polarising Magnets

For DNP, the magnetic field can be provided by an external superconducting solenoid, which has been built by the Saclay group [87]. Its maximum field is 6.5 T, but during the DNP process the magnet is operated at 70 A providing a magnetic field of 2.5 T. The solenoid has a central warm bore of 95 mm and encloses the target completely in the polarisation mode. It is designed to ensure a field homogeneity of $\pm 5 \times 10^{-5}$ over a region with a diameter of 30 mm and 200 mm length [88].

The internal holding coils, built by Rohlof [36], can be used for a longitudinal or a transverse polarised target. It is possible to operate in a continuous mode without the external polarisation magnet, due to the new internal polarisation magnet developed by Féher [37] and Bornstein [38][33].

5.4.1 Internal Polarization Coil

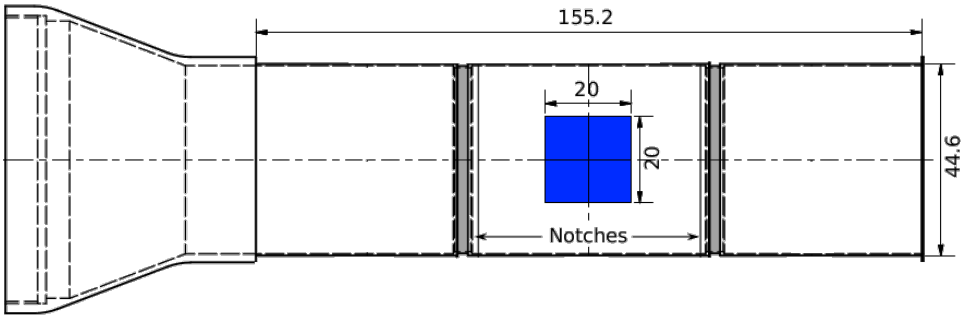

Figure 5.26: Sketch of the internal polarisation magnet, length diameter and dimension of the target region is given in [mm] [33]

In the frozen-spin mode and in the continuous mode, internal superconducting coils are used to maintain the nucleon polarisation or to create a magnetic field strong enough to polarise the target material during the data taking. For the design of these internal coils, it is necessary to reduce the thickness of these as much as possible in order to minimise the influence on the outgoing particles. Since the magnetic field $\underline{B}$ is proportional to the current I and the winding number n, this leads to high currents, a condition that can be only fulfilled by a superconducting wire. It is possible to not exceed a overall thickness of 2 mm by using a multi-filament niobium-titanium wire (⌀ 0.254 mm, insulation included), wound in an orthocyclic winding pattern [89], maximising the packing density of the wires. Fig. 5.26 shows a technical drawing of the internal polarising magnet's supporting structure. The blue rectangular shows the target region.

For polarising, the inhomogeneity of the magnetic field within the target region has to be

$$\frac{\Delta B}{B_0} = \frac{\left|\underline{B}\left(\underline{x}_0\right)\right| - B_0}{B_0} < 10^{-4}. \tag{5.41}$$

In order to reach this homogeneity Bornstein optimised the construction of the internal longitudinal polarising magnets and build a first prototype [33]. As described in the beginning of this Chapter, the internal magnet is cooled by pure ^{4}He from the separator or the evaporator. This ensures a operating temperature as low as possible. The cooling of the magnet was tested during the first performance tests

which is presented in Chap. 6.2.

5.5 Loading of the Target Material

Horizontal dilution refrigerators, like those used for the CB experiment, are build around a beam-tube. This beam tube is connected to the beam-line of the particle accelerator and has to be evacuated to reduce the heat conduction through the beam tube. Therefore, the target material is put into the refrigerator with a special insert through the beam-tube. Due to the temperature stability of the target materials, it is necessary to insert the target material under cryogenic conditions. The target material is loaded under liquid nitrogen in a cylindrical container of polytetrafluorethylen. Afterwards, the container is attached to the end of the insert and, by quickly sliding the insert through the beam-tube, the refrigerator is loaded. The mixing chamber is insulated against the beam tube vacuum by a cold indium O-ring. Fig. 5.27 shows the front part of the insert. The indium seal and the target are shown.

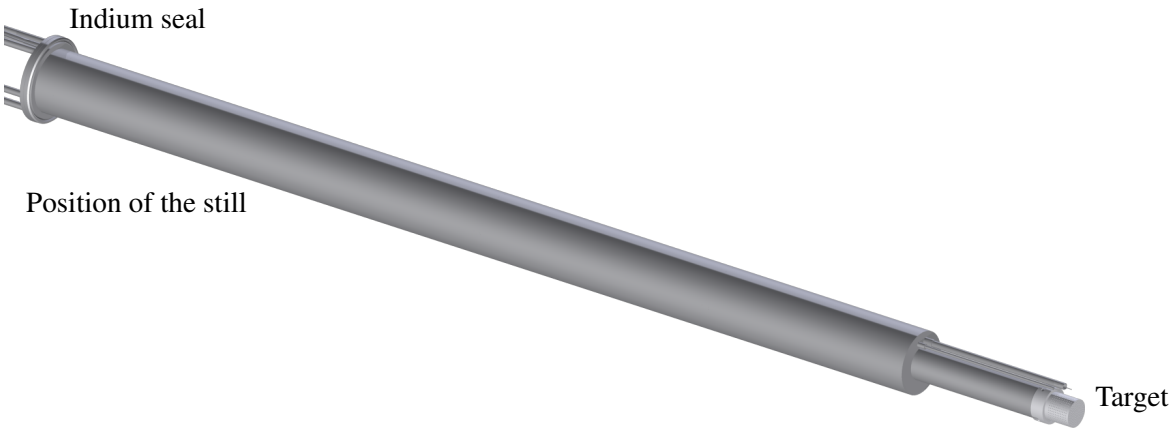

Figure 5.27: Front part of the insert

The seal is located at the position of the still. This should prevent additional heat to the target material after the insert is put into the beam-tube, due to the temperature at the sealing ($\sim$ 270 K), which is needed for a good sealing and a good vacuum in the beam-tube (see 5.1.1). To reach this temperature, a heater is located at the insert near to the sealing. The indium seal of the former frozen spin target, used for the CB experiment, was located at the mixing chamber, thus the target was heated up to $\sim$ 180 K [13]. After the sealing is heated, a heat exchanger inside the refrigerator can be used to cool down the seal as fast as possible to minimise heating of the surrounding structure. This heat exchanger is supported with liquid helium from the separator at a temperature of 3.5 K. Afterwards, the bypass can be used to cool down the dilution unit with ^{4}He.

Chapter 6

Performance of the Refrigerator

To test the dilution refrigerator, a new independent test facility was set up. This includes a root pump system for the circulating dilute, a rotary vane system for the precooling stages, the thermometry measurement system and a DAQ for the data acquisition. The recirculating system pumps off the vapour from the still and refills the gas mixture to the precooling stages. This is done by a pump cascade of four pumps:

- Okta 4000, 4000 $1\,h^{-1}$
- Okta 1000, 1000 $1\,h^{-1}$
- Okta 500, 500 $1\,h^{-1}$
- DUO 125 M, 125 $1\,h^{-1}$

build by *Pfeiffer Vacuum* [68]. The pumps of the Okta line are root vacuum pumps equipped with canned motors. The vacuum is generated by two synchronously and counter-rotating rotors operating without contact in one housing. Thus, a roots pump is sealed only by the small gap between the rotors and the housing and uses no lubrication. The suction chamber is free of oil, reducing the possibility of oil freezing out and blocking the helium tubes of the refrigerator. The dynamic sealing provides for an almost constant conductance of a roots pump rather than a constant mass flow rate. Thus, the still pressure becomes less dependent on the circulation rate, which is desirable with regard to the operational stability at high flow rates.

One disadvantage is the low compression factor of these pumps due to the gas back-streaming through the gap in the suction chamber. In order to provide a higher inlet pressures at the refrigerator, a two stage rotary vane pump is used (type DUO 125). For this pump, the suction chamber is not free of oil. To block of this oil and to purify the helium, a filter system is used. First, a filter is used to eliminate small particles such as charcoal pieces and second, a liquid nitrogen cooling trap with active carbon is used to absorb air and oil.

The cooling of the coil and the radiative heat shields have a independent pumping cascade of a Okta 2000 and a Hena 300 which are a root pump with 2000 $1\,h^{-1}$ and a rotary vane pump with 300 $1\,h^{-1}$. In addition, the different parts of the cooling stages have their own pumping system described in Chap 5.2. The following Chapter describes the essential parts of the test facility and shows the results of the first tests of the refrigerator under cryogenic conditions.

6.1 Refrigerator Diagnosis

6.1.1 Thermometry

Thermometry of a dilution refrigerator is of main importance. It is used for the optimisation of the refrigerator by controlling the critical operation parameter and to calibrate the NMR signal of the target polarisation. For that reason, a very accurate temperature measurement is needed. Besides the stability and reproducibility of the temperature measurement, a low sensitivity to a change of magnetic fields and a small size, due to the limited space in different parts of the refrigerator, are necessary.

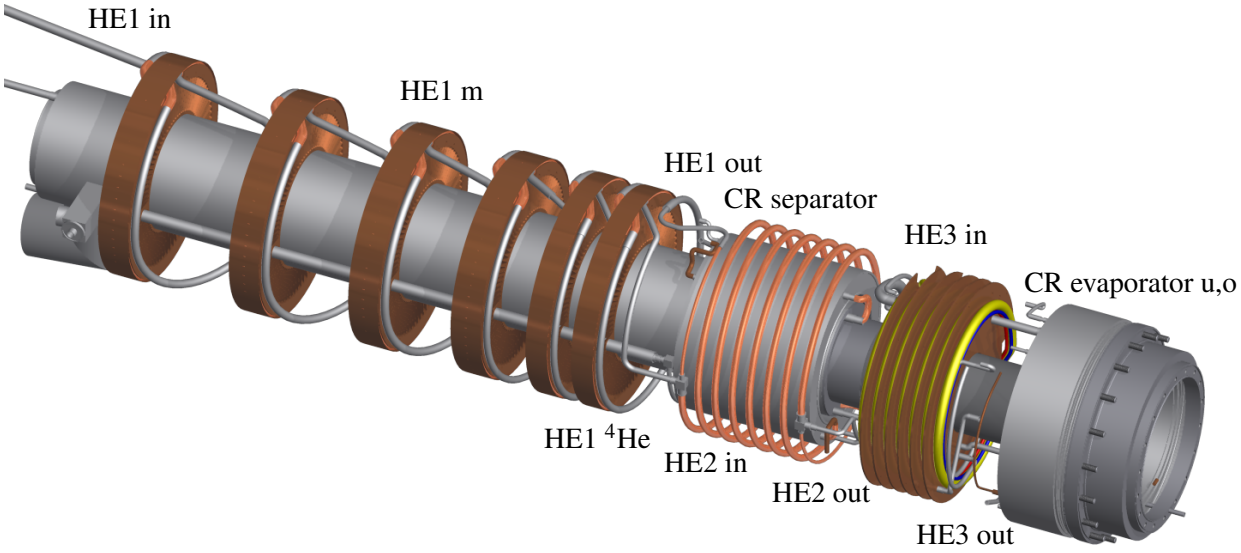

(a) Precooling

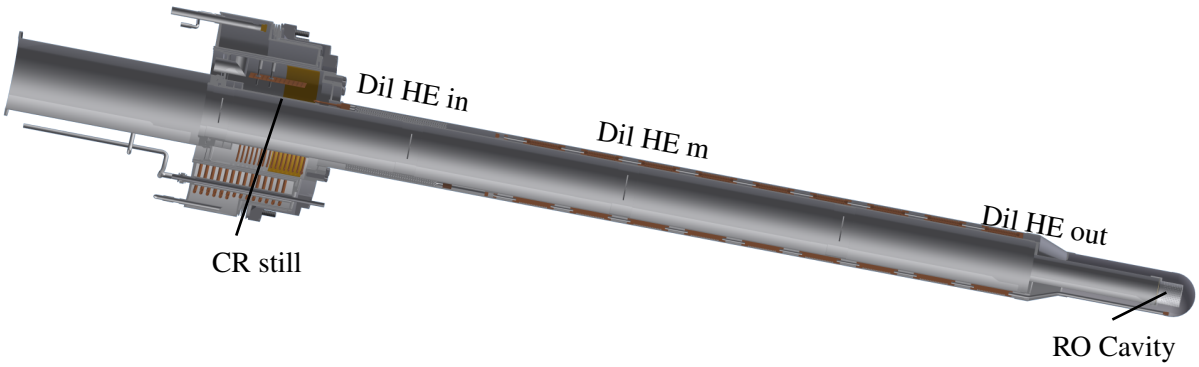

(b) Dilution Unit

Figure 6.1: Positions of the temperature sensors

For the measurement of the temperature of the outer and the inner radiation shield, the indium seal of the insert and the cooling for the transfer line, platinum resistors of the type *PT100*, having an accuracy of $\frac{\Delta R}{R} \approx 1\,\%$ down to a temperature of 15 K, are used. For a precise measurement below 15 K and a higher precision for the measurement of the cooling power, Cernox resistors manufactured by *Lake Shore Cryotronics* were used. Fig. 6.1 shows the position of the resistors for the inner parts of the refrigerator. For the incoming ^{3}He-^{4}He mixture, the temperature is measured at the in- and the outlet of the cooling stages. Thus, the temperature gradient of each heat exchanger can be measured and the flow-rate can be easily corrected for a optimal performance. Additionally, the temperature of the separator, the evaporator and the still are measured for the same reason. The temperature of the mixing chamber is of major interest. Thus, a Ruthenium Oxide Resistance, with a calibrated temperature range of 20 mK to 40 K, was used.

The resistance of all thermometers are measured by four AC bridges AVS 47, manufactured by *Picowatt*. The influence of the leads on the determination of the resistance is cancelled by the principle of a four-wire-measurement using quad twisted wires manufactured by *Lake Shore Cryotronics*. The excitation level of the bridge is a reasonable compromise between power dissipation and noise. The lowest excitation of 3 μV reduces the Joule heating at the lowest possible temperatures inside the refrigerator and is made feasible by a special amplifier placed close to the refrigerator. Thus, a precise determination of the resistance at low temperatures is possible.

6.1.2 Measurement of the ^{3}He-^{4}He ratio

In order to find the optimal working parameter of a dilution refrigerator, the knowledge about the mass flow of the different streams is of major importance, as well as the ^{4}He concentration in the circulating ^{3}He-^{4}He mixture. Therefore, for each pumping system, a mass flow meter was installed and tested. To measure the concentration of ^{4}He in the circulating mixture, a mass spectrometer, manufactured to detect only elements with an atomic mas number of ≤ 7, was installed. This system was set up and integrated in the test facility by Streit [90]. A simple scheme of the flow measurement system can be seen in Fig. 6.2.

The flow-meters HFM-300, manufactured by *Hastings*, are used to monitor the ^{4}He flow of the different precooling stages and of the circulating dilute of the dilution unit. A detailed description is given in the manuals [91] and [92]. The Sensor consists of a tube where the temperature can be measured at the in- and outlet. In the centre of the tube is a heater. If a gas flows through the tube, the temperature gradient changes and from this the flow can be calculated. For this, the flow has to be laminar what is given by a shunt used for this type of flow meter.

The mass spectrometer Microvision2 manufactured by *MKS*, which is used for this setup consists of the following parts:

- An ion source, to ionise the incoming particles
- A electrostatic slit, to accelerate the ionised particles through the spectrometer
- A quadrupole mass filter, to extract particles with a specific mass from the particle flowing through the filter
- A detector, to detect the particles after the filter unit

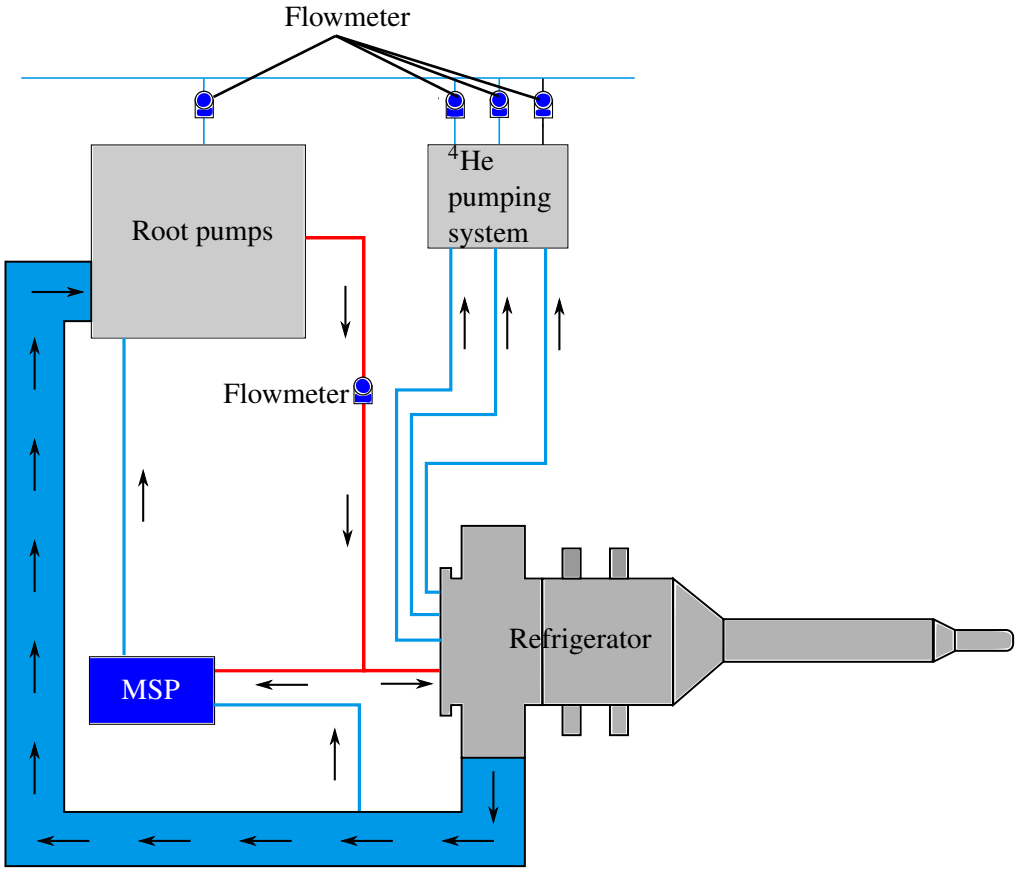

Figure 6.2: Simple scheme of the test facility [90]

- Some electronics for the DAQ
- A recipient for the measurement
- A turbo molecular pump.

A detailed description of these parts is given in [90] and [93]. The measurement of the ^{3}He-^{4}He ratio is important, due to the reduction of the cooling power of a dilution refrigerator by an increasing amount of ^{4}He in the circulating stream (see Chap. 5.3.2). The measurement of the ^{3}He-^{4}He ratio can be done like Streit did in [90].

For this determination, it is important to consider that the conductance L of the capillary, which is used to connect the recipient of the spectrometer with the test volume, as well as the pumping speed S of the turbo molecular pump, which evacuates the recipient of the spectrometer, depends of the molecular weight M, which causes a demixing of the gas molecules in the recipient. A simple scheme of the used setup is shown in Fig. 6.3. The setup of the recipient with its capillary and the value is adapted from a former setup described by Werth [94]. Using the same setup, it is possible to measure the ratio of the ^{3}He-^{4}He mixture by measuring the partial pressures of the two isotopes independent of the inlet pressure of the recipient:

$$R\left(\frac{^3\mathrm{He}}{^4\mathrm{He}}\right) = \frac{p_{^3\mathrm{He}}}{p_{^4\mathrm{He}}} \tag{6.1}$$

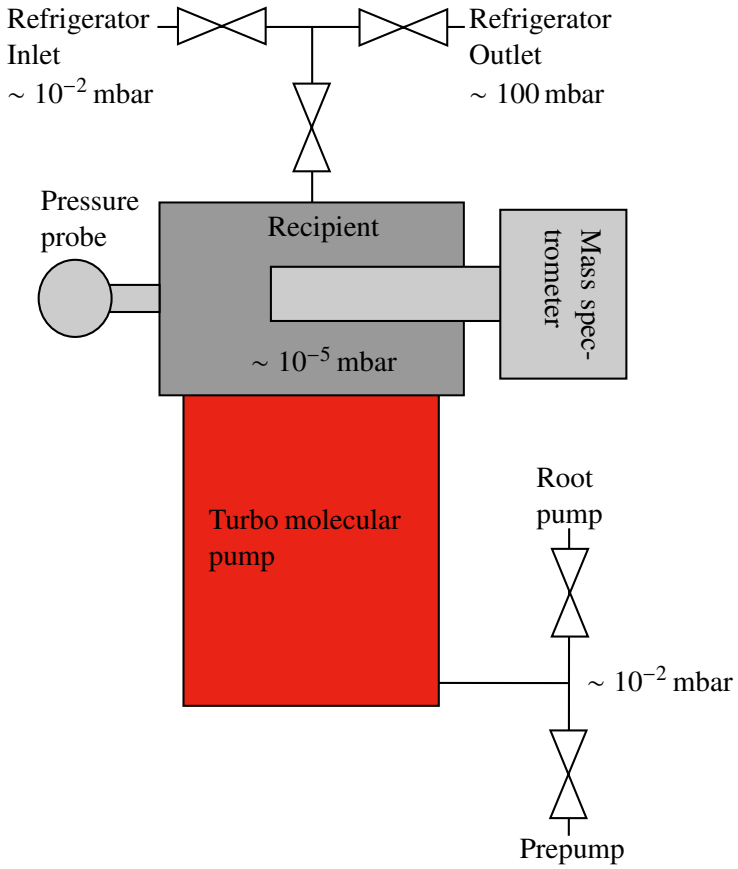

Figure 6.3: Simple scheme of the mass spectrometer inspired by [90]

6.1.3 Microwave System

For the DNP-process, the target material has to be irradiated by microwaves near the electron LAMOR frequency to induce the wanted transitions between the ZEEMAN levels. For a high efficiency of this process and a high nucleon polarisation, a frequency stability of 10^{-4} is mandatory. In addition, the ability to tune the frequency is desirable as the frequencies related to the polarisation process in positive and negative direction differ by several 100 MHz.

To polarise the target material within the dilution refrigerator, two microwave sources can be used. If a magnetic field of 2.5 T is available, a 70 GHz GUNN-diode can be used. In addition, a 50 GHz GUNN-diode is available to polarise the target at a magnetic field strength of 1.8 T. For both diodes the frequency can be varied by a control voltage and the power output at the different frequencies was measured by Golla [95] to be around 160 mW for the 70 GHz and 290 mW for the 50 GHz GUNN diode. By tuning the frequency of the microwave source the power output changes. As a consequence of this behaviour, the maximum positive and negative polarisation differ from each other. This can be compensated by changing the LAMOR-frequency caused by a change of the magnetic field. Thus, the polarisation in positive and negative direction can be achieved by the same microwave frequency and at the same microwave power.

Fig. 6.4 shows the set-up of the microwave system. The microwaves are conducted to the refrigerator by a rectangular wave-guide, which is oversized to minimise the power loss. Inside the refrigerator

they are guided by a stainless steel tube into the mixing chamber. This stainless steel tube is part of the insert and connected to the still to reduce heat conduction to the mixing chamber. At the end of the insert, it is connected to the rectangular wave-guide by a vacuum feed-through containing a window made of fluorinated ethylene propylene and in addition, it is sealed against the mixing chamber by a Teflon hood. In the case the Teflon hood does not seal the microwave guide inside the insert, it is evacuated and the ^{3}He-^{4}He mixture can be injected back to the circulation system.

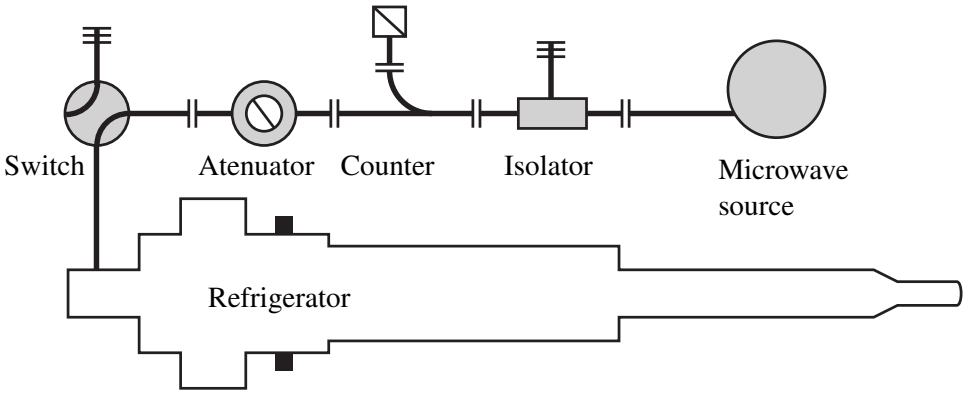

Figure 6.4: Simple scheme of the microwave system [28]

6.1.4 NMR System

The value of the nucleon polarisation is one of the most important contributions to the polarisation observable of the scattering experiment and has to be determined with an accuracy as high as possible. The target material is located inside a small coil for the measurement of the polarisation. This small coil works as a sensing probe of a series Q-meter [96]. The Q-meter is working at the Lamor-frequency of the nucleon to induce transitions between the nucleon Zeeman levels of the material. This interaction with the material exchanges energy with the Q-meter, leading to a linear dependence of the coil impedance $Z(\omega)$ on the complex magnetic susceptibility χ of the material

$$Z(\omega) = R + i\omega L\left[1 + \eta\chi(\omega)\right] \quad \text{and} \quad \chi(\omega) = \chi'(\omega) - i\chi''(\omega)\,. \tag{6.2}$$

R is the resistance, η is the effective filling factor of the target material, L the inductance for $\chi = 0$ and ω the frequency driven by a RF oscillator. Whereas the real part χ' represents the resulting inductance, the imaginary part χ'' is determined by the energy caused by the Zeeman transitions and is proportional to the population of the nucleon Zeeman levels. Thus, the imaginary part of the susceptibility is a direct measure of the polarisation of the target material.

To sustain the polarisation, as high as possible, only a small RF signal is used. Otherwise, the polarisation would be fully destroyed by the measurement. By using a continuous wave measurement procedure with a small signal, only a small part of the polarisation will be used for the measurement. This leads to the problem that the NMR-system has to be calibrated to determine the polarisation. It is realised by the measurement of the target polarisation in thermal equilibrium at ~ 1 K. As described in

Chap. 2.1, Eq. 2.7 and 2.8 can be used to calculate the assumed polarisation in thermal equilibrium. This can be used to determine a calibration factor for the polarisation measurement

$$P_{\text{meas}} = P_{\text{TE}} \frac{A_{\text{meas}}}{A_{\text{TE}}}, \tag{6.3}$$

where A_{i} are the surfaces of the measured signals. Then the polarisation of the target, reached by the DNP, can be measured. The signal of the NMR coil is guided by a coaxial line through the insert outside the refrigerator to the room temperature electronics. There are two systems available:

- The LIVERPOOL NMR Module [97]
- A NMR Module manufactured in Bonn, created by Kaufmann [28] and improved by Voge [98] and Miebach [99]

Both Q-meters can be connected to the same Computer system and are controlled and analysed by a computer program generated with *LabView*.

6.1.5 DAQ

For the polarised target to work well, a computer aided control and data acquisition is needed. For this, a *LabView* generated data acquisition, which also communicates with the different controlling parts of the test facility, was implemented [100]. A key feature of this new system is the possibility of having a dynamic and scalable system to allow the introduction of further instruments and measurement devices in an easy way. Shared variables are the basis of this system which allow a network wide management and supervision of all kinds of parameters which are necessary for the operation of a refrigerator. This allows to read out the measurement devices with different PCs and send their data to a single Server PC which hosts all shared variables in use.

Due to this system, it is easy to connect the different measurement devices via USB, GPIB or Multi I/O-boards to a PC and read out the parameters with *LabView* programs which were programmed by different members of the polarised target group in Bonn.

To operate the pumping system, a PLC controlling is used which allows switching of electronic valves and activation of vacuum pumps. The different parts communicates via the industrial network *Inter-Bus* with the PLC. This system is connected via an OPC server to the data acquisition system. Thus, it is possible to use shared variables for the vacuum components too. This allows a visualisation and operation of the whole system with one DAQ system.

6.2 First Cool down

First cool down tests of the refrigerator were performed. For this tests, liquid ^{4}He was used to cool down the refrigerator to its operational temperature and to test for cold leaks. Due to possible fixings of the precooling stages, the dilution heat exchanger was not mounted and the precooling unit was tested by circulating ^{4}He instead of the ^{3}He-^{4}He mixture, which is used in a dilution refrigerator. Thus, ^{4}He gas was filled into the dilution circuit. Nevertheless, it was possible to test the precooling stages with this setting. Following the cool down procedure, the performance tests of the cooling for the internal magnet and the precooling unit are presented.

6.2.1 Cool down procedure

Horizontal dilution refrigerators, like the refrigerator designed within this thesis, cool the circulating ^{3}He-^{4}He mixture under the usage of liquid ^{4}He supported from a Dewar. Thus, before the refrigerator is operational, the different parts have to be cooled from room temperature to the specific working temperatures. For this, it is possible to use a bypass to fill liquid ^{4}He from the separator to the dilution unit. The temperature of the heat sinks and the cavity, during the cool down phase, can be seen in Fig. 6.5. First, the separator reaches a temperature of around 100 K. Due to the fact that the separator is filled

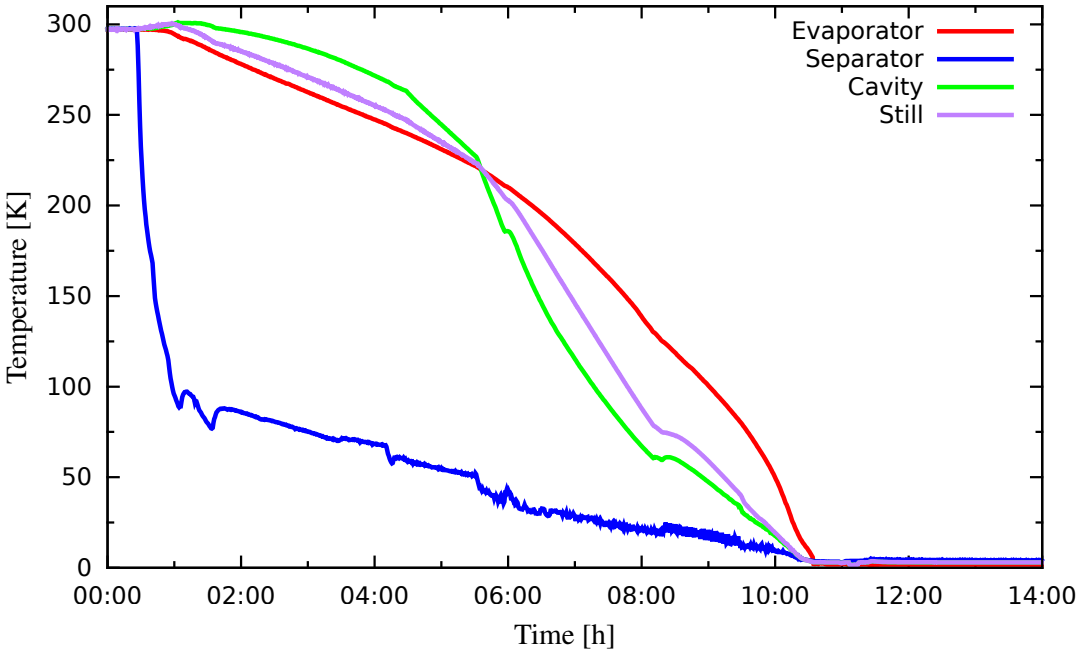

Figure 6.5: Temperature of the heat sinks and the dilution unit during cool down phase

with helium from the Dewar in a direct way, it is obvious that this stage is the first part of the refrigerator which is cooled (see Fig. 5.6). From the separator, the ^{4}He is guided to the different cooling parts and heat sinks of the refrigerator. The flow to this parts can be regulated by needle valves. After the separator reaches a temperature below 100 K, the incoming ^{4}He is cold enough to cool the other parts of the refrigerator. By usage of the different needle valves, it is possible to cool down the refrigerator as uniformly as possible. Fig. 6.6 shows that liquid helium enters the separator and the evaporator within a few minutes. This method to cool down the refrigerator allows to reduce thermal stresses to the structure and to fill in liquid helium into the dilution unit within $\sim$ 11h.

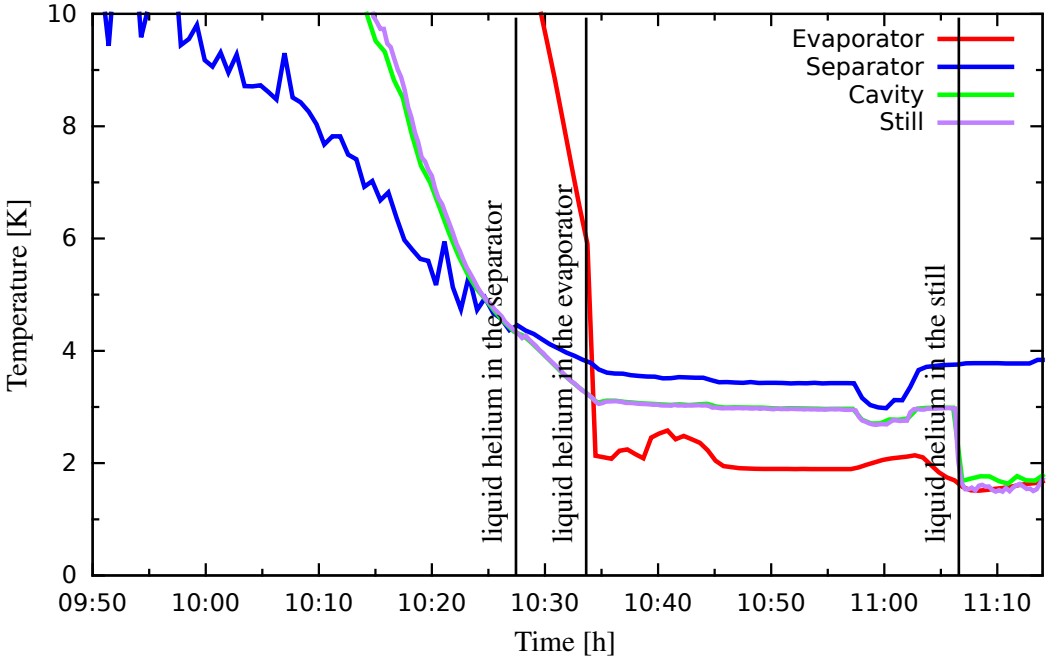

Figure 6.6: Temperature of the heat sinks and the dilution unit in detail

In addition, the heat radiation shields and the internal magnet have to be cooled down. Fig. 6.7 shows the temperature behaviour of the radiation shields during the cool down period.

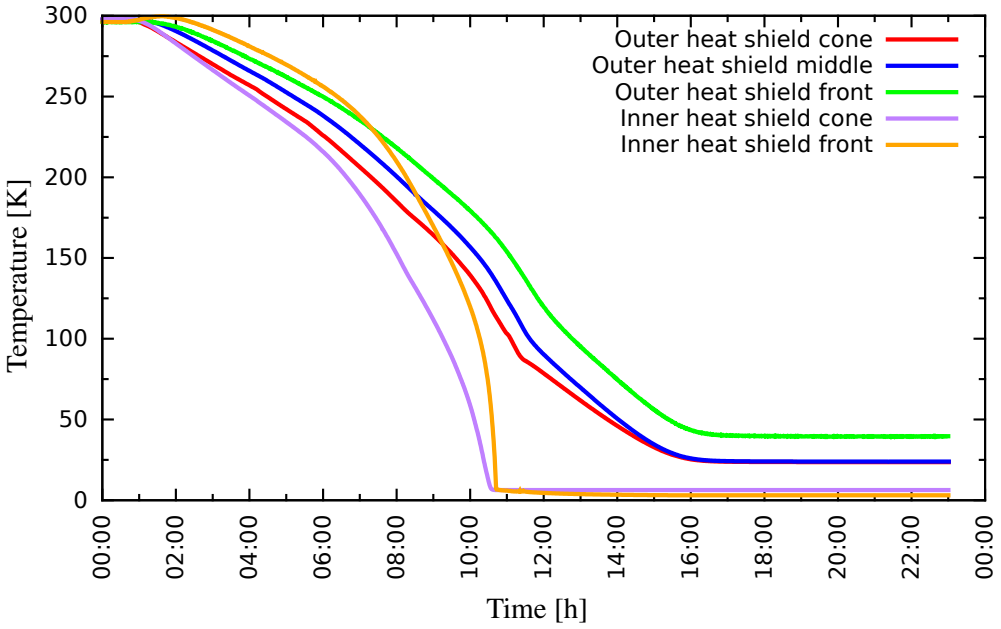

Figure 6.7: Temperature of the heat radiation shields during cool down phase

The cooling system for the internal magnet and the radiation shields is filled with liquid ^{4}He from the separator during the cool down phase and afterwards from the evaporator. This uncouples the internal

magnet from the dilution unit and makes it possible to reduce the thermal load on the different cooling stages of the refrigerator. Fig. 6.7 shows that after ≈ 10 h, where liquid helium enters the separator and the evaporator for the first time, the inner radiation shield is cooled to around 3 K. 5 h later the outer radiation shield is cooled to its operational temperature and the whole refrigerator is cooled down.

It takes 17 h to cool the precooling stages, the internal magnet and the radiation shields to its operational temperatures. For this, an amount of 15.2 kg corresponding to 121.61 of liquid helium is necessary. Then the refrigerator is ready to be filled with the ^{3}He-^{4}He mixture.

6.2.2 Cooling of the internal magnet

First tests with the internal magnet were done. It was possible to cool down the internal magnet to temperatures between 1.2 K and 1.9 K, depending of the temperature of the evaporator. Using the prototype of Bornstein [33], it was possible to operate the magnet with a current of ≈ 78 A before quenching.

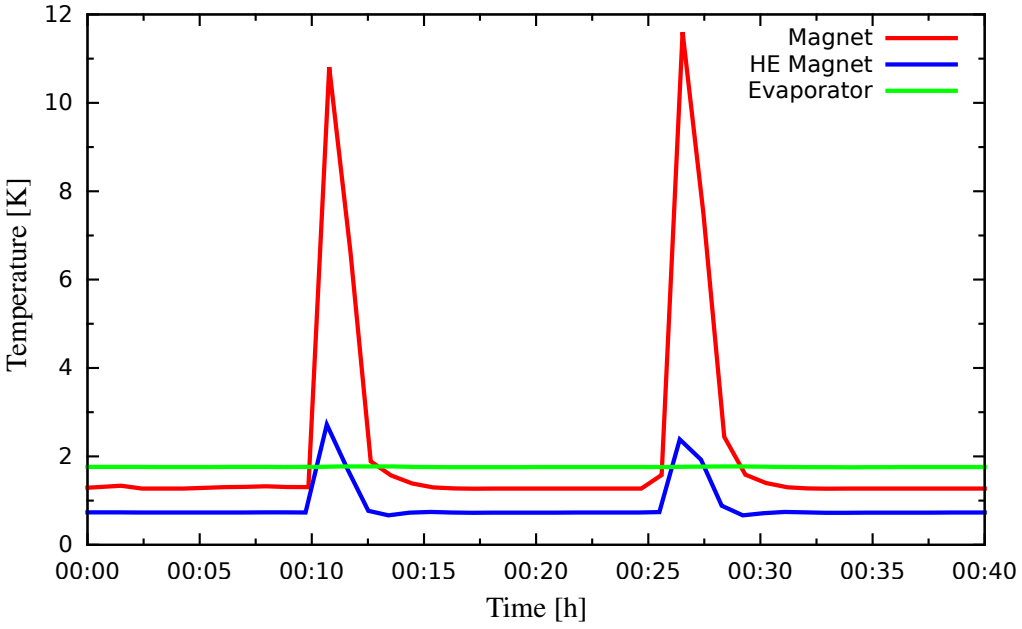

Figure 6.8: Temperature profile during a quench of the internal coil

Fig. 6.8 shows the temperature of the internal magnet, the heat exchanger cooling the coil and the evaporator which supports the liquid helium for the cooling. In this case the internal magnet quenched two times in a very short timescale. The temperature of the magnet rises up to around 11 K, where the temperature of the heat exchanger himself only raises to a temperature between 2 K and 3 K.

The temperature of the evaporator is not affected. Thus, the design with an additional cooling for the internal magnet to uncouple the cooling of the magnet from the refrigerator works well. Without changing the flow through the heat exchanger, the heat of the quench can be transported away in about 5 min to 10 min and the magnet is cooled to its operational temperature. With the prototype of the magnet, which was used for this tests, it is possible to operate the refrigerator as a continuous mode target at a magnetic field of 1.8 T, if a longitudinal target polarisation is needed. In addition, a new prototype is

under construction and concepts to improve the cooling of the current leads will be tested by Bornstein [33].

6.2.3 Test measurement of the precooling stages

To test the performance of the precooling unit, the necessary ^{4}He flow rates for the different cooling stages were measured depending on the flow rate of the fluid circulating in the ^{3}He-^{4}He circuit. This measurement was done with pure ^{4}He instead of the ^{3}He-^{4}He mixture for dilution mode, due to a cold leak to the isolation vacuum making it difficult to operate the refrigerator in a stable operation mode. In addition, ^{3}He would be lost through the leak which has to be avoided.

Nevertheless, it was possible to test the precooling stages with ^{4}He gas, filled in the ^{3}He-^{4}He circuit to cool and liquefy it with the precooling unit of the refrigerator. For all measurements the inlet pressure for the test fluid was set to 100 ± 5 mbar.

The flow rate of the test fluid was set to a specific value by the ^{3}He needle valve and measured with the system mentioned in Chap. 6.1.2. The ^{4}He flow of the precooling stages were set by needle valves too. By optimising the flows of ^{4}He, the heat exchangers were operated by the simulated temperatures at the measurement places. This means that the pressures and temperatures of the precooling unit were held to be as constant as possible to make a comparison to the simulated data possible. The temperatures of the precooling unit during the test and the simulated temperatures are presented in Tab. 6.1.

Table 6.1: Measured and simulated temperatures of the precooling stages

Temperature probe	Simulated	Measured
$HE1_{in}$	170 K	170 ± 5 K
$HE1_{middle}$	43 K	43 ± 3 K
$HE1_{out}$	8 K	8 ± 1 K
$HE2_{in}$	8 K	8 ± 1 K
$HE2_{out}$	3.5 K	3.5 ± 0.2 K
Separator	3.5 K	3.5 ± 0.2 K
$HE3_{in}$	3.5 K	3.5 ± 0.2 K
$HE3_{out}$	1.5 K	2.0 ± 0.5 K
Evaporator	1 K	1.8 ± 0.2 K

The simulated temperatures of HE1 and HE2 and the assumed temperature of the separator are in good agreement with the measurement. The evaporator and the outlet of HE3 are at higher temperatures than the simulation predicts. This is a result of the leak to the isolation vacuum. Due to the leak, it was not possible to fill the dilution unit complete with liquid helium. This results in a higher heat load to the evaporator which makes it impossible to reduce the flow to the evaporator. Due to the higher temperature of the evaporator, the temperature of the cooling ^{4}He at the ^{4}He inlet of HE3 is also higher.

The necessary flow rate for the precooling and liquefaction of the circulating ^{3}He-^{4}He mixture which is shown in Fig. 6.9 for heat exchanger 1 and 2 and in Fig. 6.10 for heat exchanger 3 was already shown in Chap. 5.2.2 and 5.2.3. Fig. 6.9 shows that the simulated flow rates fits well to the measurement if it is taken into account that the circulating test fluid was pure ^{4}He instead of a ^{3}He-^{4}He mixture. Thus,

the flow characteristic of these heat exchangers is understood and can be well described by the CFD-simulations which were performed. In adition, it seems that the leak does not influence the cooling stages after the separator.

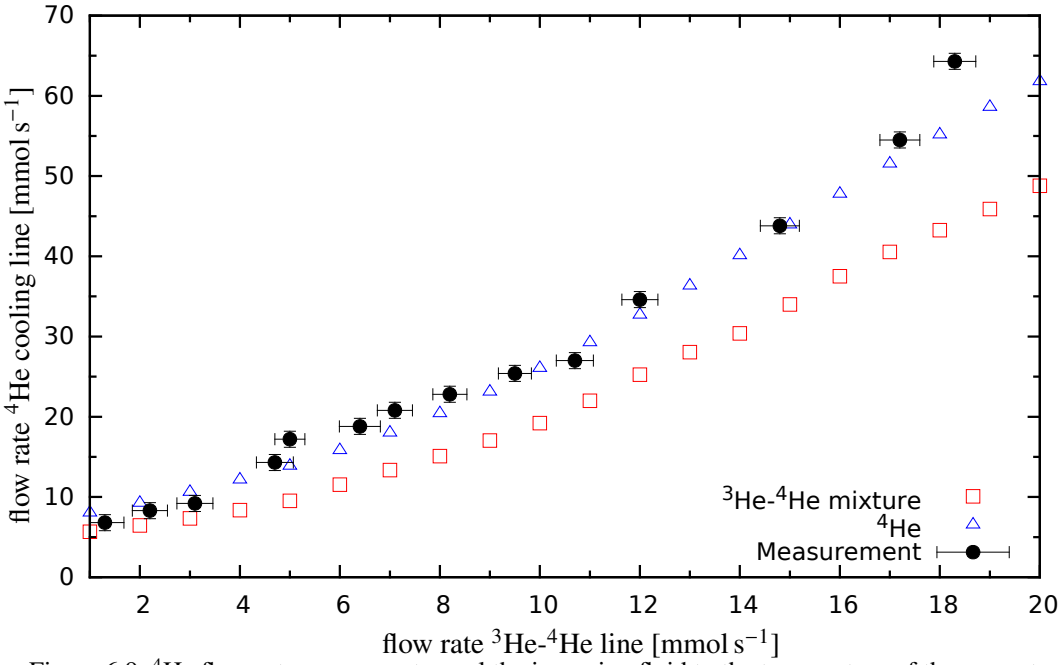

Figure 6.9: ^{4}He flow-rate necessary to cool the incoming fluid to the temperature of the separator

Fig. 6.10 shows a different behaviour. For increasing flow rates the difference between the simulated and the measured data becomes greater. As in Chap. 5.2.3 already discussed a bigger difference than for HE1 and HE2 was assumed, due to the simple model for the super fluid ^{4}He. Also, that the phase boundary between gaseous and liquid fluid was not modelled in detail could have an influence on the simulated data. In addition, the mismatch between simulation and measurement can be explained by the existing leak between the isolation vacuum and the dilution unit.

As shown in Tab. 6.1, the evaporator is operated at higher temperatures than for the calculation assumed. This results in a higher temperature for HE3 and therefore to a different performance as expected. Due to the leak, it was not possible to fill the dilution unit complete or get the refrigerator in a stable operation mode for long term measurements. This leads to a higher temperature of the cavity and the still, which also leads to a higher temperature of the back streaming gas from the dilution unit. Thus, both cooling streams have a higher temperature at the inlet.

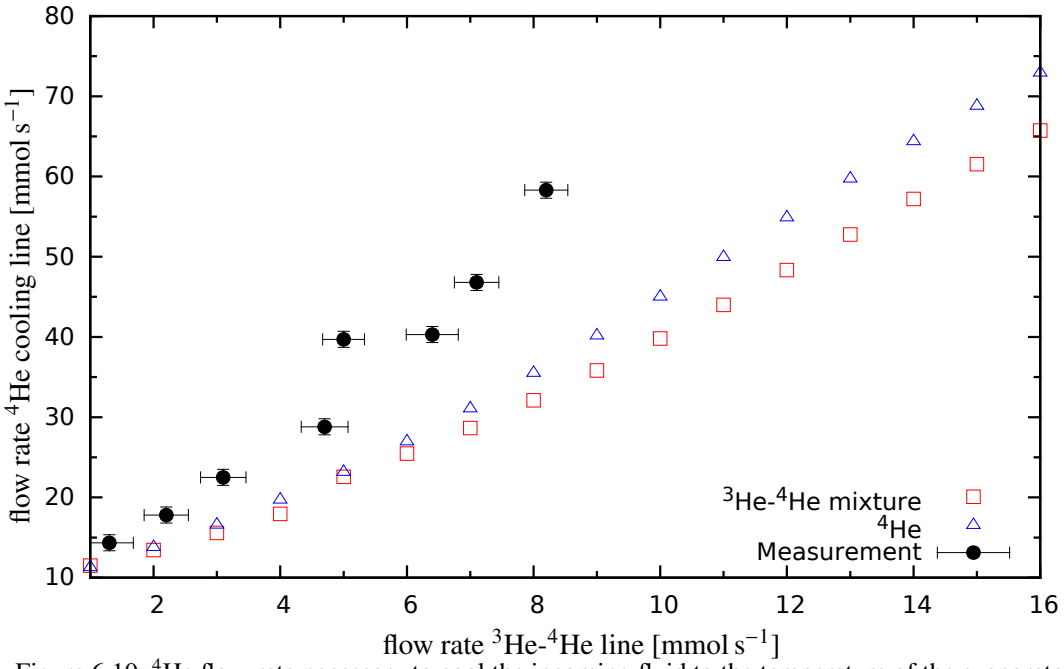

Figure 6.10: ^{4}He flow-rate necessary to cool the incoming fluid to the temperature of the evaporator

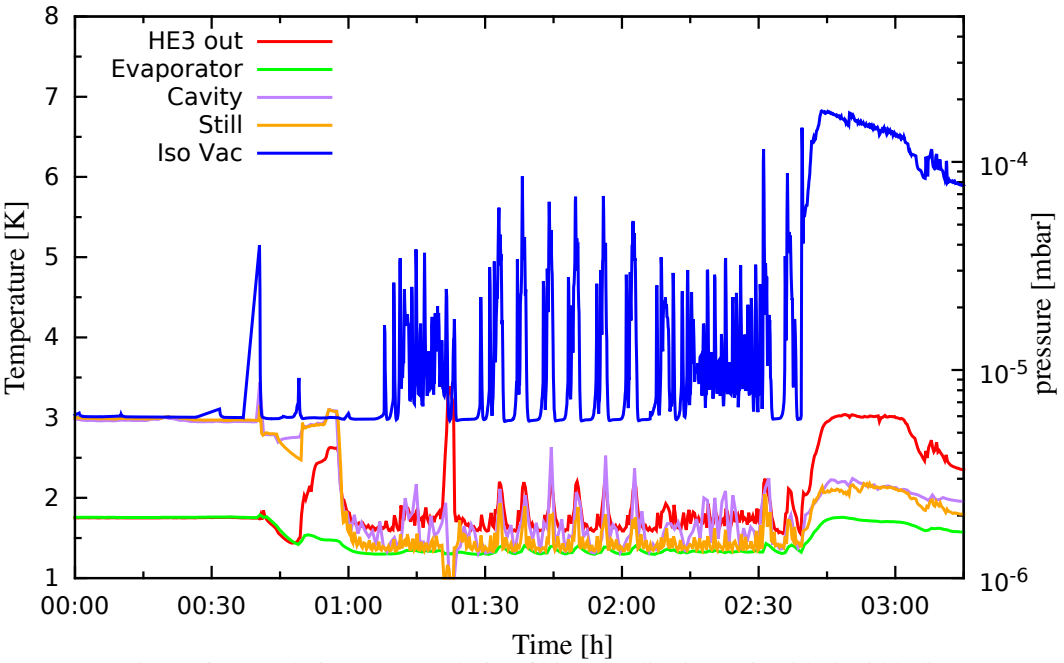

Figure 6.11: Isolation vacuum during filling the dilution unit with liquid helium

Fig. 6.11 shows the influence of the cold leak to the operation of the refrigerator. In this case, the dilution unit was filled with ^{4}He from the bypass. The temperature drop in cavity and still shows that liquid helium enters the dilution unit. The isolation vacuum rises but a semi stable operation mode is possible. It seems that super fluid helium reaches the leak and evaporates into the isolation vacuum. This leads to a temperature rise, which breaks the superfluid state of the helium and the superfluid helium film at the

position of the leak is gone. Then the isolation vacuum decreases until new liquid helium reaches the leak.

After 2.5 h, the liquid helium level is high enough for a constant flow of helium to the isolation vacuum. Due to the increasing pressure, the heat load to the dilution unit and the evaporator increases and it is not possible to operate the evaporator at a temperature below 1.5 K. Also, the temperature in the dilution unit increases and a stable operation of the refrigerator is not possible. In this situation the full amount of helium in the dilution unit evaporates and the temperature of the dilution unit increases by several Kelvin.

Different leak tests were done to locate the leak from the dilution unit to the isolation vacuum. Unfortunately, the leak is a cold leak. Only at temperatures below 80 K the leak is detectable. Thus, the front part of the inner shell has been unmounted and tested under liquid nitrogen at a temperature of 77 K. This test showed that this part of the dilution unit has no leak and can be eliminated as a possible location. Also, if the indium seal of the dilution unit would not work properly, the leak would be still detectable after a cool down. Additional tests with liquid nitrogen showed that the cold leak is located at the still. Additional leak tests are ongoing to find the exact position.

For a full operating refrigerator this leak has to be found and fixed. If the leak is found and fixed, the refrigerator has to be tested in dilution mode with a target material to find the optimal operation parameter for frozen spin and continuous polarising operation modes. Afterwards, the dilution refrigerator can be used as a continuous polarising target and the usage of the first prototype for the internal polarisation magnet.

Chapter 7

Summary

The CBELSA/TAPS experiment has produced a large amount of data on photo-production reactions in double polarization reactions. For this a frozen-spin target has been used, which consists of a horizontal dilution refrigerator with an internal holding coil for a 4π acceptance.

For further experiments with CBELSA/TAPS, a new horizontal dilution refrigerator has been designed as a continuous polarised solid target to increase the FOM. This can be realized by an internal polarization magnet for a continuous polarisation of the target material during the data taking of the experiment. This refrigerator was designed to:

- Support an internal superconducting magnet for continuous polarisation during the measurement
- Improve the performance to reach lower temperatures for the frozen-spin mode (30 mK)
- Optimise the loading procedure to lower the maximum temperature during the change of the target material

First, the different heat sources to the mixing chamber were calculated. To minimise the influence of these heat leaks a vacuum shell with two radiation shields at 40 K and 3 K was designed to minimize the heat input by radiation. Also the holding structure and the connections between the different heat exchangers were built from stainless steel for a low thermal conduction along the structure. For thermal isolation, a critical part of the refrigerator is the beam-tube, due to the necessity of a good isolation vacuum in this part of the refrigerator. The beam-tube is sealed by an indium O-ring and the tightening of this seal is important for the vacuum in the beam-tube. Taking all heat sources into account gives a heat of 40 µW to the mixing chamber.

In order to improve the knowledge about the fluid characteristics of the precooling stages, CFD simulations were performed. Thus, with a FVE-method, it is possible to calculate a vector field for the fluid pressure, velocity, density and the temperature of the different heat exchangers and the different streams flowing through these heat exchangers. These simulations were performed for a ^{3}He-^{4}He mixture flowrate of $1 - 20\,\mathrm{mmol\,s^{-1}}$. It was possible to predict the necessary ^{4}He flow rate for the heat exchangers, HE1 and HE2, to precool the circulating dilute of the refrigerator. Nevertheless, for HE3 only a coarse model was used, due to the fact that one of the 4 streams in this heat exchanger has to be super fluid and only the thermal conditions of this state were implemented in this calculation. This means that the predicted flow rate of ^{4}He is only a rough assumption for the performance of this heat exchanger. It is the first time CFD-simulations have been used to predict the performance of a dilution refrigerator for a polarised target. Now these simulations can be used to optimise the performance of the condenser unit of other dilution refrigerators. It is possible to draw a specific geometry and use the input parameter of these simulations to test new heat exchanger concepts before building a prototype.

The dilution unit has to cool the target material, under the usage of the dilution effect, to temperatures around 30 mK for the frozen spin mode and to 200 mK in the case of a continuous operating target. Additionally, the geometry of the target front is limited through the geometry of the detector and the external polarisation magnet. Thus, the outer diameter of the front of the refrigerator has to be smaller than 94 mm including the vacuum shell, the radiation shields, the internal magnet and the dilution heat exchanger. Also, these parts surrounds the beam tube which is necessary to guide the particle beam to the target material. For a good performance of the dilution unit a copper sintered heat exchanger has been designed. It is composed of 10 stages to prevent heat conduction along the axis of the heat exchanger. The calculation shows, that, including the heat leaks, it should be possible to reach temperatures around 30 mK in dilution mode. Due to the available computer resources the copper sintered heat exchanger was not simulated. In principle, by programming a specific solver it should be possible to use *openFOAM* for the simulation of the copper sintered dilution heat exchanger if the necessary computer power is available.

A test facility was built to measure the performance of the refrigerator. The facility consists of a vacuum system, including several probes to measure the pressure and the volume flow in the different cooling streams, a NMR- and microwave-system, special electronics for the determination of the temperature and a mass-spectrometer to determine the ^{3}He-^{4}He ratio.

First test measurements with ^{4}He, instead of a ^{3}He-^{4}He mixture, circulating in the closed cooling circuit were performed and the simulated data for the first two heat exchangers are in good agreement with these measurements. Unfortunately, due to a cold leak between the dilution unit and the isolation vacuum it was not possible to operate the refrigerator in the dilution mode. It was not possible to reach the necessary temperature of 1 K in the evaporator due to this leak. This also increased the temperatures of HE3, which reduces the performance of the refrigerator. In addition, to test if a continuous mode of the refrigerator is possible, the prototype of an internal magnet was used to test the cooling of the magnet. It was possible to reach temperatures below 1.5 K and to generate a magnetic field of 2.2 T. Thus with a 50 GHz microwave-source, it should be possible to use the refrigerator as a continuous mode polarised target, if the leak of the dilution unit is fixed.

The tests to locate the leak are ongoing. Unfortunately, the cold leak is only detectable at temperatures below 80 K. If the leak has been located and fixed, the refrigerator will be first tested in ^{4}He mode for further leaks and afterwards the dilution heat exchanger can be mounted. Then, the refrigerator has to be tested in dilution mode and after optimising the operation parameter it can be used for the measurements at CBELSA/TAPS.

Appendix A

Useful Informations

A.1 Physical properties of Helium

Table A.1: Properties of the stable liquid helium isotopes [42]

Properties	^{3}He	^{4}He
Density $\rho \left[\mathrm{g\,cm^{-3}}\right]$ ($T = 0\,\mathrm{K}$)	0.0823	0.146
Boiling point T_b [K]	3.191	4.215
Critical temperature T_c [K]	3.324	5.20
Critical pressure p_c [bar]	1.165	2.289
Critical density $\rho_c \left[\mathrm{g\,cm^{-3}}\right]$	0.0413	0.0693
Melting pressure p_m [bar] ($T = 0\,\mathrm{K}$)	34.39	25.36
Minimum melting pressure p_m [bar]	29.31	25.32
Maximum superfluid transition temperature T_c [K]	0.0025	2.177
Gas-to-liquid volume ratio (liquid at 1 K, gas at 300 K and at 1 bar) T_c [K]	662	866
Classical molar volume $V_m \left[\mathrm{cm^3\,mol^{-1}}\right]$ (at saturated vapour pressure and $T = 0\,\mathrm{K}$)	12	12
Molar volume $V_m \left[\mathrm{cm^3\,mol^{-1}}\right]$ (at saturated vapour pressure and $T = 0\,\mathrm{K}$)	36.84	27.58

A.2 Case structure in OpenFOAM 2.4.0

The case is set up in an appropriately named folder. It contains three sub-folders: *system*, *constant*, and 0. In the 0 directory the initial and boundary conditions for all fields of the case are defined.

The *constant* folder contains case specific files defining the geometrical and thermo-physical properties of the case. The geometrical properties are stored in the sub-folder *polymesh* inside the *constant* folder. The files with the thermo-physical and turbulence properties are stored directly in the *constant* folder.

In the *system* folder the files relevant to the solver, e.g. the *fvScheme*, are located. It provides the information which numerical schemes has to be used. The *fvSolution* and *fvOptions* contain the convergence criteria, the algorithm and physical boundaries. In the *controlDict* the start time, the end time and other run time utilities are defined.

In the cases used for the refrigerator, so-called multi meshes were used. For each mesh a sub folder in 0, *constant* and *system* exists which contains the necessary files for the simulation. An overview for all necessary folders and files is given in Fig. A.1. A full description of the necessary case structure and the executable applications is given in [63].

```
./
├── 0
│   ├── p
│   ├── p_rgh
│   ├── T
│   └── U
├── Allclean
├── Allrun
├── Allrun.pre
├── baf_multi_OpenFOAM.sh
├── baf_snappy.sh
├── constant
│   ├── helium3_in │   ├── helium3_out │   ├── helium4 │   ├── polyMesh │   ├──
RASProperties
│   ├── RASProperties~
│   ├── regionProperties
│   ├── thermophysicalProperties
│   ├── transportProperties
│   ├── transportProperties~
│   ├── turbine1 │   ├── turbine2 │   ├── turbine3 │   ├── turbine4 │   ├── turbine5 │
├── turbine6 │   └── turbulenceProperties
├── forceCoeffs
├── functions
├── Residuals
├── result.html
├── system
│   ├── controlDict
│   ├── createCellZone.topoSetDict
│   ├── createInletOutletSets.topoSetDict
│   ├── createPatchDict
│   ├── createPatchDict.domain
│   ├── createPatchDict.inout
│   ├── createPatchDict.oldInternalFaces
│   ├── decomposeParDict
│   ├── fvSchemes
│   ├── fvSolution
│   ├── helium3_in │   ├── helium3_out │   ├── helium4 │   ├── meshQualityDict
│   ├── removeOldInternalFaces.setSet
│   ├── removeRedundantZones.setSet
│   ├── removeRedundantZones.topoSetDict
│   ├── snappyHexMeshDict
│   ├── surfaceFeatureExtractDict
│   ├── surfaceFeatureExtractDictDefaults
│   ├── turbine1 │   ├── turbine2 │   ├── turbine3 │   ├── turbine4 │   ├── turbine5 │
└── turbine6 └── test.html
```

Figure A.1: Example case structure for a ChtMultiRegionSimpleFoam case

A.3 Heat load to the inner refrigerator parts

Table A.2: Radiative heat transfer to the mixing chamber

	P	$\frac{P}{\sigma}$
outer radiation shield	13.7 W	2.03 mW/cm^2
inner radiation shield	33.4 mW	8.25 mW/cm^2
cooling structure for radiation shields and magnet	2.3 mW	314 nW/cm^2
internal polarization magnet	93.4 nW	275 pW/cm^2
mixing chamber	41 pW	0.21 pW/cm^2

Table A.3: Gaseous conduction

	P	$\frac{P}{\sigma}$ [nW/cm^2]
outer radiation shield	2.7 mW	460
inner radiation shield	0.8 mW	156
cooling structure for radiation shields and magnet	0.18 mW	40
internal polarization magnet	2.3 μW	6.7
mixing chamber	0.4 μW	2.0

A.4 Boundarys for heat exchanger 1 and 2

Table A.4: Boundary conditions for velocity U and pressure p

Boundary	Patch	HE1	HE2
U	input ^{4}He	1 mmol s^{-1} to 60 mmol s^{-1}	1 mmol s^{-1} to 60 mmol s^{-1}
	output ^{4}He	1 mmol s^{-1} to 60 mmol s^{-1}	1 mmol s^{-1} to 60 mmol s^{-1}
	input ^{3}He$_{in}$	1 mmol s^{-1} to 20 mmol s^{-1}	1 mmol s^{-1} to 20 mmol s^{-1}
	output ^{3}He$_{in}$	1 mmol s^{-1} to 20 mmol s^{-1}	1 mmol s^{-1} to 20 mmol s^{-1}
	input ^{3}He$_{out}$	1 mmol s^{-1} to 20 mmol s^{-1}	1 mmol s^{-1} to 20 mmol s^{-1}
	output ^{3}He$_{out}$	1 mmol s^{-1} to 20 mmol s^{-1}	1 mmol s^{-1} to 20 mmol s^{-1}
	walls	(0, 0, 0)m s^{-1}	(0, 0, 0)m s^{-1}
p	output ^{4}He	5 mbar to 20 mbar	10 mbar to 40 mbar
	input ^{4}He	*zeroGradient*	*zeroGradient*
	input ^{3}He$_{in}$	100 mbar to 180 mbar	60 mbar to 150 mbar
	output ^{3}He$_{in}$	*zeroGradient*	*zeroGradient*
	input ^{3}He$_{out}$	1×10^{-1} mbar to 1 mbar	5×10^{-2} mbar to 5×10^{-1} mbar
	output ^{3}He$_{out}$	*zeroGradient*	*zeroGradient*
	walls	*zeroGradient*	*zeroGradient*

Table A.5: Boundary conditions for temperature T

Boundary	Patch	HE1	HE2
T	input ^{4}He	5 K to 10 K	3.8 K
	output ^{4}He	*zeroGradient*	*zeroGradient*
	input ^{3}He$_{in}$	300 K	5 K to 10 K
	output ^{3}He$_{in}$	*zeroGradient*	*zeroGradient*
	input ^{3}He$_{out}$	5 K	3 K
	output ^{3}He$_{out}$	*zeroGradient*	*zeroGradient*
	wall_to_solid	*compressible::turbulent*	*compressible::turbulent*
		TemperatureCoupled	*TemperatureCoupled*
		BaffleMixed	*BaffleMixed*
	solid_to_wall	*compressible::turbulent*	*compressible::turbulent*
		TemperatureCoupled	*TemperatureCoupled*
		BaffleMixed	*BaffleMixed*

Bibliography

[1] C. Berger, *Teilchenphysik, Eine Einführung*. Springer-Lehrbuch, 1st ed., 1992.

[2] V. E. Barnes *et al.*, "Observation of a Hyperon with Strangeness −3," *Physical Review Letters*, vol. 12, p. 204, 1964.

[3] S. Weinberg, "Nonabelian Gauge Theories of The Strong Interaction," *Physical Review Letters*, vol. 31, p. 494, 1973.

[4] H. Fritzsch, M. Gell-Mann, and H. Leutwyler, "Advantages of the Color Octet Gluon Picture," *Physical Letters B*, vol. 47, p. 365, 1973.

[5] A. V. Anisovich *et al.*, "The Impact of New Polarization Data from Bonn, Mainz and Jefferson Laboratory on $\gamma p \to \pi N$ Multipoles," *arXiv:1604.05704v1 [nucl-th] 19 Apr 2016*.

[6] W. T. Chiang and F. Tabakin, "Completeness Rules for Spin Observables in Pseudoscalar Meson Photoproduction," *Subnuclear Structure of Matter: Achievements and Challenges*, vol. 55, p. 2054, 1997.

[7] J.-L.-U. G. Rheinische Friedrich-Wilhelms-Universität Bonn, Ruhr-Universität Bochum, "Subnuclear Structure of Matter - Elektromagnetische Anregung subnuklearer Systeme, Finanzierungsantrag 01.07.2004 - 30.06.2008," *Sonderforschungsbereich / Transregio 6034*, vol. 35, 2003.

[8] R. Beck and U. Thoma, "Spectroscopy of baryon resonances," *EPJ Web of Conferences*, vol. 134, p. 02001, 2017.

[9] W. Hillert, "The Bonn Electron Stretcher Accelerator ELSA: Past and Future," *European Physics Journal A*, vol. 28S1, p. 139, 2006.

[10] R. Beck *et al.*, "Timing and tracking for the Crystal Barrel detector," *EPJ Web of Conferences*, vol. 134, p. 05003, 2017.

[11] S. B. Gerasimov, "A sum rule for magnetic moments and the damping of the nucleon magnet moment in nuclei," *Soviet Journal of Nuclear Physics 2*, vol. 4, p. 430, 1966.

[12] S. D. Drell and A. C. Hearn, "Exact Sum Rule for Nucleon Magnetic Moments," *Physical Review Letters*, vol. 16, p. 908, 1967.

[13] C. Bradtke, *A New Frozen-Spin Target for the Measurement of the Helicity Asymmetry of the Total Photoabsorption Cross-Section*. Phd thesis, Universität Bonn, January 2000. IR-2000-1.

[14] C. Bradtke, "A new frozen-spin target for 4π particle detection," *Nuclear Instruments and Methods in Physics Research A*, vol. 436, pp. 430–442, 1999.

[15] R. Gehring *et al.*, "First use of an internal superconducting 'holding magnet' in an η-photoproduction experiment," *Nuclear Instruments and Methods in Physics Research A*, vol. 418, p. 233, 1998.

[16] H. Dutz *Proceedings of the 16th International Spin Physics Symposium*, p. 221, 2004.

[17] H. Dutz, "Highlights of polarized solid state target instrumentation," *Nuclear Instruments and Methods in Physics Research A*, vol. 526, p. 117, 2004.

[18] H. Dutz, "personal communication."

[19] W. Polifke and J. Kopitz, *Wärmeübertragung*. Pearson Studium, 2nd ed., 2009.

[20] W. Wagner, *Wärmeaustauscher*. Vogel, 4th ed., 2009.

[21] G. Frossati, "Experimental Techniques: Methods for Cooling Below 300 mK," *Journal of Low Temperature Physics*, vol. 87, p. 595, 1992.

[22] G. Frossati, "Obtaining Ultralow Temperatures by Dilution of ^{3}He into ^{4}He," *Journale de Physique (Paris)*, vol. 39 (C6), p. 1578, 1978.

[23] H. Haken and H. C. Wolf, *Atom- und Quantenphysik*. Springer, 8th ed., 2004.

[24] NIST, "2010 CODATA recommended values." Website, 2010. http://physics.nist.gov/cuu/Constants/index.html.

[25] A. Abragam and W. G. Proctor, "Experiments on Spin Temperature," *Physical Review*, vol. 106, p. 160, 1957.

[26] A. Abragam and M. Goldmann, "Principles of Dynamic Nuclear Polarisation," *Reports on Progress in Physics*, vol. 41, p. 395, 1978.

[27] A. Berlin, "Spindiffusionsmessungen in polarisierten Festkörpermaterialien," Master's thesis, Ruhr-Universität Bochum, 2010.

[28] T. Kaufmann, "Aufbau eines modularen NMR-Systems zur Polarisationsmessung an polarisierten Festkörpertargets," Diploma thesis, Universität Bonn, 2010. IB-2010-04.

[29] A. G. Redfield, "Nuclear magnetic resonance saturation and rotary saturation in solids," *Physical Review*, vol. 98, p. 1787, 1955.

[30] S. Goertz, "The dynamic nuclear polarisation prozess," *Nuclear Instruments and Methods in Physics Research*, vol. A526, p. 28, 2004.

[31] C. Collaboration *et al.*, "COMPASS-II Proposal," *CERN SPSC*, vol. 14, p. 340, 2010.

[32] S. Runkel, "Herstellung und Untersuchung von Ammoniakkristallen als polarisiertes Target für das COMPASS-Experiment," Diploma thesis, Universität Bonn, 2011. IB-2012-10.

[33] M. Bornstein, *PhD thesis in preparation*. PhD thesis, Universität Bonn, 2017.

[34] R. Gehring, *Ein neuartiges Frozen Spin Target zur Messung der Targetasymmetrie in der η-Photoproduktion*. Phd thesis, Universität Bonn, 1996. IR-96-16.

[35] A. Thiel *et al.*, "Double-polarization observable G in neutral-pion photoproduction," *arXiv:1604.02922v1 [nucl-ex] 11 Apr 2016*, 2016.

[36] C. Rohlof, *Entwicklung polarisierter Targets zur Messung der Gerasimov-Drell-Hearn-Summenregel an ELSA*. Phd thesis, Universität Bonn, April 2003.

[37] B. Feher, "Entwicklung eines supraleitenden, kryostatinternen Polarisationsmagneten für polarisierte Targets," Diploma thesis, Universität Bonn, 2010.

[38] M. Bornstein, "Bau eines supraleitenden, kryostatinternen Polarisationsmagneten für polarisierte Targets," Diploma thesis, Universität Bonn, 2010.

[39] J. A. Peacock, *Cosmological Physics*. Cambrige University Press, 7th ed., 2005.

[40] W. E. Keller, *^{3}He and ^{4}He*. Plenum Press, 2nd ed., 1969.

[41] G. Ventura and L. Risegari, *The Art of Cryogenics*. Elsevier, 1st ed., 2008.

[42] F. Pobell, *Matter and Methods at Low Temperatures*. Springer, 3rd ed., 2007.

[43] S. Reeve, *PhD Thesis in preparation*. Phd thesis, Universität Bonn, 2017.

[44] D. S. Greywall, "Specific heat and phonon dispersion of liquid ^{4}He," *Physical Review*, vol. B 18, p. 2127, 1978.

[45] D. S. Greywall, "Specific heat of normal liquid ^{3}He," *Physical Review*, vol. B 27, p. 2747, 1983.

[46] D. S. Greywall, "^{3}He specific heat and thermometry at millikelvin temperatures," *Physical Review*, vol. B 33, p. 7520, 1986.

[47] R. J. Donnelly and C. F. Barenghi, "The Observed Properties of Liquid Helium at the Saturated Vapor Pressure," *Journal of Physical and Chemical Reference Data*, vol. 27, p. 1217, 1998.

[48] F. Schwabl, *Statistische Mechanik*. Springer, 3rd ed., 2006.

[49] D. S. Greywall, "The Observed Properties of Liquid Helium at the Saturated Vapor Pressure," *Physical Review*, vol. B 23, p. 2152, 1981.

[50] J. Wilks, *The Properties of Liquid and Solid Helium*. Clarendon Oxford, 1967.

[51] C. Ebner and D. O. Edwards, "The low temperature thermodynamic properties of superfluid solutions of ^{3}He in ^{4}He," *Physics Report*, vol. 2, p. 77, 1971.

[52] G. E. Watson, J. D. Reppy, and R. C. Richardson, "Low-Temperature Density and Solubility of ^{3}He in Liquid ^{4}He under Pressure," *Physical Review*, vol. 188, p. 384, 1969.

[53] H. London and G. R. Clarke, "Osmotic Pressure of ^{3}He in Liquid ^{4}He, with Proposal for a Refrigerator to Work below 1 K," *Physical Review*, vol. 5, p. 1992, 1962.

[54] A. C. Anderson, J. I. Connolly, and J. C. Wheatley, "Thermal boundary resistance between solids and helium below 1 K," *Physical Review A*, vol. 135, p. 910, 1964.

[55] J. C. Wheatley, O. E. Vilches, and W. R. Abel *Low Temperature Physics*, vol. 4, p. 1, 1971.

[56] N. Borisov, “personal communication.”

[57] L. Prandtl and H. Oertel, *Führer durch die Strömungslehre*. Springer Vieweg, 13th ed., 2012.

[58] O. Foundation, “OpenFOAM 2.4.0.” Website. http://www.openfoam.com/.

[59] OpenFOAM Foundation, “OpenFOAM 2.4.0 User Guide.” https://cfd.direct/openfoam/user-guide/mesh-description/#x23-1580005.1.

[60] R. Schwarze, *CFD-Modellierung*. Springer Vieweg, 2013.

[61] J. H. Ferziger, *Computational Methods for Fluid Dynamics*. Springer Vieweg, 3rd ed., 2002.

[62] H. Versteeg and W. Malalasekera, *An introduction to Computaltional Fluid Dynamics*. Longman Scientific and Technical, 1st ed., 1995.

[63] OpenFOAM Foundation, “OpenFOAM 2.4.0 C++ Guide.” Website. http://www.openfoam.com/documentation/cpp-guide/html/.

[64] OpenFOAM Foundation, “OpenFOAM 2.4.0 C++ Guide.” Website, 2017. https://github.com/OpenFOAM/OpenFOAM-2.4.x/tree/master/src/turbulenceModels /compressible/turbulenceModel/derivedFvPatchFields/turbulentTemperatureCoupledBaffleMixed.

[65] E. H. Kennard, *Kinetic Theory of Gases*. McGaw-Hill Book Company, 1st ed., 1938.

[66] F. Pavese and G. Molinar Min Beciet, *Modern Gas-Based Temperature and Pressure Measurements*. Boston, MA: Springer US, 2013.

[67] G. K. White, “Experimental Techniques in Low-Temperature Physics,” *Clarendon Press*, 1968.

[68] Pfeiffer Vacuum GmbH, Berliner Strasse 43, 35614 Asslar, Germany, *The Vacuum Technology Book, Know-how Book*.

[69] G. Wiedemann and R. Franz, “Über die Wärmeleitfähigkeit der Metalle,” *Annalen der Physik*, vol. 165 No. 8, pp. 497–531, 1853.

[70] N. C. T. Group, “Material Properties: 304 Stainless.” Website, 2016. http://cryogenics.nist.gov/MPropsMAY/304Stainless/304Stainless_rev.htm.

[71] B. A. Hands, “Cryogenic Engineering,” *Academic Press*, 1986.

[72] L. Klostermann, “Heat Sinking of Cryogenic Coaxial Cables in a Dilution Refrigerator,” *Proceedings of High Energy Spin Physics 1990*, 1990.

[73] R. C. Richardson and E. N. Smith, *Experimental Techniques in Condensed Matter Physics at Low Temperatures*. Addison Wesley, 1988.

[74] O. V. Lounasmaa, *Experimental Principles and Methods Below 1 K*. Academic Press, 1974.

[75] R. Radebaugh and J. D. Siegwarth, “Dilution refrigerator technology,” *Cryogenics*, vol. 11, p. 368, 1971.

[76] C.-I. Um, “Thermal Conductivity and Viscosity in Dilute ^{3}He-^{4}He Mixtures Below 0.6 K,” *Journal of Low Temperature Physics*, vol. 109, pp. 495–510, 1997.

[77] N. C. T. Group, "2010 CODATA recommended values." Website, 2016. http://cryogenics.nist.gov/MPropsMAY/OFHCCopper/OFHC_Copper_rev1.htm.

[78] W. H. Keesom and P. Keesom, "The Viscosity of Liquid Helium," *Physica V*, vol. 8, p. 737, 1938.

[79] W. H. Keesom and P. Keesom, "On the Viscosity of Liquid Helium in theNeigbourhood of the Lambpda-Point," *Physica VIII*, vol. 1, p. 65, 1941.

[80] M. A. Black, H. E. Hall, and K. Thomson, "The Viscosity of Liquid Helium 3," *Journal of Physics C: Solid State Physics*, vol. 4, p. 129, 1971.

[81] R. Radebaugh and J. Siegwarth, "Dilution refrigerator technology," *Cryogenics*, vol. 11, no. 5, pp. 368 – 384, 1971.

[82] A. Thomas, N. S. Borisov, W. Meyer, and Y. A. Usov, "The new frozen spin target at MAMI," *Physics of Particles and Nuclei*, vol. 44, no. 6, pp. 964–967, 2013.

[83] W. R. Abel, R. T. Johnson, and J. C. Wheatley, "Thermal Conductivity of Pure ^{3}He and of Dilute Solutions of ^{3}He in ^{4}He at Low Temperatures," *Physical Review Letter*, vol. 18, p. 737, 1967.

[84] R. König and F. Pobell, "Temperature, Pressure and Concentration Dependence of the Viscosity of Liquid ^{3}He-^{4}He Mixtures at Low Temperatures," *Physical Review Letters*, vol. 71, p. 2761, 1993.

[85] R. Radebaugh, "US National Bureau of Standards Technical Note," vol. 362, 1967.

[86] J. D. Siegwarth and R. Radebaugh, "Analysis of Heat Exchangers for Dilution Refrigerators," *Review of Scientific Instruments*, vol. 42, p. 1111, 1971.

[87] P. Chaumette *et al. Proceedings of the 19th International Symposium on High Energy Spin Physics*, vol. 2, p. 237, 1990.

[88] P. Chaumette *et al.*, "Advances in Cryogenic Engineering," *Plenum Press*, vol. 35, 1990.

[89] E. Kallenbach *et al.*, *Elektromagnete-Grundlagen, Berechnung, Entwurf.* Vieweg and Teubner, 4th ed., 2012.

[90] B. Streit, "Einrichtung eines ^{3}He/^{4}He Messsystems zur Überwachung und Leistungsoptimierung eines Dilutionkryostaten," Diploma thesis, Universität Bonn, 2014.

[91] T. H. Instruments, *Instruction Manual HFM-300 Flow Meter, HFC-302 Flow Controller*.

[92] T. H. Instruments, *Instruction Manual 201/203/205/207 Series Flow Meters/Controllers*.

[93] M. I. U. Ltd, *Microvision2 Hardware Manual, SP101015.106*.

[94] H. Werth, "Eine Aperatur zur Bestimmung der Heliumpartialdrücke eines Dilutionkryostaten," Diploma thesis, Universität Bonn, 1996. IR-96-13.

[95] I. Golla, "Aufbau und Vermessung von Mikrowellensystemen zur dynamischen Polarisation von festkörpertargets," Bachelor thesis, Universität Bonn, 2014.

[96] G. Reicherz *et al.*, "The Bonn polarized target NMR-system," *Nuclear Instruments and Methods A*, vol. 356, p. 74, 1995.

[97] G. Court *et al.*, "A high precision Q-meter for the measurement of proton polarization in polarised targets," *Nuclear Instruments and Methods A*, vol. 324, p. 433, 1993.

[98] T. Voge, "Untersuchung des Einflusses der HF-Komponenten eines NMR-Schwingkreises auf dessen Stabilität und Rauschverhalten," Diploma thesis, Universität Bonn, 2012.

[99] R. Miebach, "Aufbau eines modernen NMR-Systems zur präzisen Polarisationsbestimmung an deuterierten Festkörpertargets," Diploma thesis, Universität Bonn, 2014.

[100] M. Sommer, "A Scalable Data Acquisition System for Polarized Solid State Targets," Master's thesis, Universität Bonn, 2014.

List of Figures

List of Tables